



**HAL**  
open science

# Hyperfractals for wireless networks modelling

Dalia-Georgiana Popescu

► **To cite this version:**

Dalia-Georgiana Popescu. Hyperfractals for wireless networks modelling. Networking and Internet Architecture [cs.NI]. Sorbonne Université, 2018. English. NNT : 2018SORUS264 . tel-02868490

**HAL Id: tel-02868490**

**<https://theses.hal.science/tel-02868490>**

Submitted on 15 Jun 2020

**HAL** is a multi-disciplinary open access archive for the deposit and dissemination of scientific research documents, whether they are published or not. The documents may come from teaching and research institutions in France or abroad, or from public or private research centers.

L'archive ouverte pluridisciplinaire **HAL**, est destinée au dépôt et à la diffusion de documents scientifiques de niveau recherche, publiés ou non, émanant des établissements d'enseignement et de recherche français ou étrangers, des laboratoires publics ou privés.



**THÈSE DE DOCTORAT DE  
L'UNIVERSITÉ PIERRE ET MARIE CURIE**

Spécialité

**Informatique**

École Doctorale Informatique, Télécommunications et Électronique (Paris)

Présentée par

**Dalia-Georgiana POPESCU**

Pour obtenir le grade de

**DOCTEUR de l'UNIVERSITÉ PIERRE ET MARIE CURIE**

Sujet de la thèse :

**Les Hyperfractales  
pour la Modélisation des Réseaux sans Fil**

soutenue le 21 Novembre 2018

devant le jury composé de :

M. Bartłomiej BŁASZCZYSZYN	INRIA	Directeur de thèse
M. Philippe JACQUET	Nokia Bell-Labs	Directeur de thèse
M. Gustavo DE VECIANA	UT Austin	Rapporteur
M. Konstantin AVRACHENKOV	INRIA	Rapporteur
M. Anastasios GIOVANIDIS	UPMC	Examineur
M. Bernard MANS	MacQuarie University	Examineur
Mme. Maria POTOP-BUTUCARU	UPMC	Examineur
M. Luis Guilherme UZEDA GARCIA	Nokia Bell-Labs	Examineur

“Fractal geometry will make you see everything differently. There is a danger in reading further. You risk the loss of your childhood vision of clouds, forests, flowers, galaxies, leaves, feathers, rocks, mountains, torrents of water, carpet, bricks, and much else besides. Never again will your interpretation of these things be quite the same.”

- Michael F. Barnsley

“My life seemed to be a series of events and accidents. Yet when I look back, I see a pattern.”

— Benoît B. Mandelbrot

# Contents

<b>List of Figures</b>	<b>v</b>
<b>List of Tables</b>	<b>vii</b>
<b>Acknowledgements</b>	<b>viii</b>
<b>Abstract</b>	<b>ix</b>
<b>Les Hyperfractales pour la Modélisation des Réseaux sans Fil</b>	<b>x</b>
0.1 Les Modèles d' Hyperfractales . . . . .	xii
0.1.1 Un Modèle de Propagation qui Génère la Nécessité d'Elargir le Modèle Topologique. L'Effet Canyon . . . . .	xv
0.1.2 Le Modèle Hyperfractale pour les Relais . . . . .	xv
0.2 Des Applications pour les Réseaux sans Fil . . . . .	xvi
0.2.1 Procédure de Validation avec des Données . . . . .	xvi
0.2.2 Etude de la Vitesse de Propagation de l'Information dans un Réseau Urbain Tolérant aux Retards . . . . .	xviii
0.2.3 Le Routage de Bout en Bout dans un Réseau Hyperfractale avec Relais . . . . .	xxi
0.2.4 Goulot d'Etranglement . . . . .	xxiii
<b>1 Introduction and Motivation</b>	<b>1</b>
1.1 Technological Context . . . . .	1
1.2 Motivation . . . . .	5
1.3 Contributions and Structure of the Thesis . . . . .	6
1.4 Publications . . . . .	8
<b>2 Classic Stochastic Geometry</b>	<b>10</b>
2.1 Notions of Classic Stochastic Geometry . . . . .	12
2.1.1 Model fundamentals . . . . .	12
2.1.2 Poisson Point Process . . . . .	14
2.1.3 Poisson Line Process . . . . .	16
2.1.4 Voronoi Tessellations . . . . .	16
2.2 State of the Art of Stochastic Modeling of the Wireless Networks Topologies	17
2.3 Mobility Estimation in Cellular Networks by Means of Stochastic Geometry	19
2.3.1 Mobility State Estimation . . . . .	20

2.3.2	System Model . . . . .	22
2.3.3	Stochastic Geometry and User History based Mobility Estimation: STRAIGHT . . . . .	23
2.3.4	Stretch Parameter Computation . . . . .	24
2.3.5	Performance Evaluation . . . . .	26
2.3.6	Lessons Learned . . . . .	29
<b>3</b>	<b>Self-Similar Geometry. The Hyperfractal Model</b>	<b>30</b>
3.1	Self-similar Geometry. Fractals . . . . .	30
3.1.1	Fractal Dimension . . . . .	31
3.1.2	The Sierpinski Triangle . . . . .	33
3.2	Self-Similarity of Human Society Geometry. Self-Similarity of Wireless Networks . . . . .	34
3.3	Poisson-Shots on Fractal Maps as Precursors of the Hyperfractal Model . . . . .	35
3.3.1	Definition of Poisson-shots on Fractal Maps . . . . .	36
3.3.2	Towards the Hyperfractal . . . . .	38
3.4	The Hyperfractal Model . . . . .	39
3.4.1	Propagation Model as Feature of the Topological Model. Urban Canyon Model . . . . .	39
3.4.2	The Support . . . . .	40
3.4.3	The Hyperfractal Model for Mobile Users . . . . .	41
3.4.4	Hyperfractal Model for Relays . . . . .	43
3.5	Stochastic Geometry of the Hyperfractal Model . . . . .	46
3.5.1	Typical Points of $\Phi$ , $\Phi^r$ and $\Xi$ . . . . .	46
3.5.2	Fundamental Properties of the Typical Points . . . . .	47
3.5.3	An Alternative Method for Computing the Number of Relays in the Map . . . . .	49
3.6	Concluding Remarks . . . . .	50
<b>4</b>	<b>Model Fitting with Traces. Computation of Fractal Dimension</b>	<b>52</b>
4.1	Theoretical Foundation . . . . .	53
4.1.1	Density-to-Length Criteria and the Computation of the Fractal Dimension . . . . .	53
4.1.2	The Spatial Intersection Density Criterion . . . . .	54
4.1.3	The Time Interval Intersection Criterion . . . . .	55
4.2	Data Fitting Examples . . . . .	55
4.3	Concluding Remarks . . . . .	58
<b>5</b>	<b>Application to Ad-Hoc Networks. End-to-End Energy versus Delay</b>	<b>59</b>
5.1	Introduction and Motivation . . . . .	59
5.2	System Model . . . . .	61
5.2.1	Preliminary Study on Connectivity with no Energy Constraints . . . . .	62
5.3	Main Results . . . . .	65
5.3.1	Path Cumulated Energy . . . . .	67
5.3.2	Path Maximum Energy . . . . .	72
5.3.3	Remarks on the Network Throughput Capacity . . . . .	73

5.3.4	Simulations . . . . .	74
5.4	Short Study on Load and Bottleneck . . . . .	78
5.4.1	System Model . . . . .	78
5.4.2	Main Results . . . . .	79
5.5	Simulations . . . . .	81
5.6	Concluding Remarks . . . . .	83
<b>6</b>	<b>Application to Ad-Hoc networks. Delay-Tolerant Networks</b>	<b>84</b>
6.1	Introduction and Motivation . . . . .	84
6.2	System Model . . . . .	86
6.2.1	Canyon Effect . . . . .	87
6.2.2	Broadcast Algorithm . . . . .	87
6.3	Main Results . . . . .	88
6.3.1	Upper Bound . . . . .	88
6.3.2	Lower Bound . . . . .	94
6.3.3	Asymptotic to Poisson Uniform . . . . .	95
6.3.4	Extension with Limited Radio Range . . . . .	96
6.3.5	Information Teleportation . . . . .	98
6.4	Simulations in a System Level Simulator . . . . .	99
6.4.1	QualNet Network Simulator Configuration . . . . .	99
6.4.2	Urban Vehicular Environment Modeling and Scenario Description . . . . .	100
6.4.3	Validation of Upper and Lower Bounds: Constant Speed . . . . .	102
6.4.4	Validation of Bounds Under Speed Variation . . . . .	102
6.5	Simulations in a Self-Developped Discrete Time Event-Based Simulator . . . . .	105
6.5.1	Information Spread Under Hyperfractal Model and Teleportation Phenomenon . . . . .	106
6.5.2	Validation of Upper and Lower Bounds on the Average Broadcast Time in the Entire Network . . . . .	107
6.5.3	Validation of Bounds on Average Broadcast Time Under Speed Variation . . . . .	108
6.6	Concluding Remarks . . . . .	109
<b>7</b>	<b>Conclusion and Future Work</b>	<b>111</b>
7.1	Conclusion . . . . .	111
7.2	Future Work . . . . .	112
7.2.1	Generalization of the Model for Nodes . . . . .	113
7.2.2	Generalization to Poisson Points on Poisson Lines . . . . .	113
7.2.3	Generalization to Poisson Voronoi Tessellations . . . . .	114
7.2.4	In-Depth Percolation for a Finite Window . . . . .	115
<b>A</b>	<b>Proofs</b>	<b>116</b>
	<b>Bibliography</b>	<b>118</b>

# List of Figures

1	La carte de Indianapolis . . . . .	xi
2	(A) Le support; (B) Hyperfractale, $d_F = 3$ , $n = 1,200$ noeuds; . . . . .	xiv
3	La procédure d'emplacement des relais . . . . .	xvi
4	Carte avec noeuds et relais . . . . .	xvii
5	Procédure pour Minneapolis . . . . .	xix
6	La téléportation d'information . . . . .	xx
7	a) Chemin dévié avec trois relais fixes (à gauche), b) cinq relais fixes (à droite). . . . .	xxiii
8	Énergie de bout en bout minimale cumulée par rapport aux sauts pour une paire émetteur-récepteur. . . . .	xxiii
9	Répartition de la charge dans un hyperfractal avec $d_f = 3.3$ , $d_r = 2.3$ , index des noeuds jusqu'à l'index 500, index des relais à partir de l'index 500 . . . . .	xxiv
1.1	Property of Nokia Networks: Smart Cities that Enrich Life . . . . .	3
2.1	Poisson point process . . . . .	14
2.2	Voronoi tessellation . . . . .	17
2.3	UE mobility through heterogeneous networks. . . . .	20
2.4	The 3GPP LTE MSE algorithm. . . . .	21
2.5	Macro cell network topology. . . . .	22
2.6	Principle of the equivalent cell radius. . . . .	24
2.7	Examples of UE trajectories in the network. . . . .	27
2.8	Histogram of UEs' speed in cells. . . . .	28
3.1	Gosper island, Koch snowflake, box fractal, Sierpiński sieve . . . . .	31
3.2	Sierpinski triangle construction process . . . . .	33
3.3	Paris view from space at night. Courtesy of NASA/ESA . . . . .	34
3.5	Variation of parameter $a$ . . . . .	37
3.6	Signal strength heat map in a city. Canyon effect . . . . .	39
3.7	Hyperfractal support construction process . . . . .	40
3.8	. . . . .	41
3.9	Hyperfractal with $n = 1,200$ mobile nodes, $d_F = 3$ . . . . .	42
3.10	Relays process construction . . . . .	44
3.11	Complete hyperfractal map with mobiles and relays . . . . .	45
3.12	Measured versus computed number of relay in the map for several values of $k_{max}$ . . . . .	48



4.1	Procedure for Minneapolis . . . . .	55
4.2	Procedure for Nyon . . . . .	56
4.3	Procedure for Seattle . . . . .	57
4.4	Procedure for Adelaide . . . . .	57
5.2	a) Diverted path with three fixed relays (left), b) five fixed relays (right).	70
5.3	Minimum cumulated end-to-end energy versus hops for a transmitter-receiver pair. . . . .	75
5.4	Minimum cumulated end-to-end energy versus hops, averaging over 100 transmitter-receiver pairs, $d_F = 4.3, d_r = 3.3, n = 800$ . . . . .	76
5.5	Minimum cumulated end-to-end energy versus hops, averaging over 100 transmitter-receiver pairs, $d_F = 4.3, d_r = 3.3, n = 1000$ . . . . .	76
5.6	Minimum cumulated end-to-end energy versus hops, averaging over 100 transmitter-receiver pairs, $d_F = 3.2, d_r = 2.3, n = 800$ , linear scale left, logarithmic scale right . . . . .	76
5.7	Minimum cumulated end-to-end energy versus hops, averaging over 100 transmitter-receiver pairs, $\alpha = 2, d_F = 3.3, d_r = 2.3, n = 1000$ , linear scale left, logarithmic scale right . . . . .	77
5.8	Minimum cumulated end-to-end energy versus hops, averaging over 100 transmitter-receiver pairs, $\alpha = 3, d_F = 4.33, d_r = 3, n = 800$ . . . . .	77
5.9	Path maximum energy versus hops . . . . .	78
5.10	Load distribution in hyperfractal $d_m = 3.3, d_r = 2.3$ , nodes index up to index 500, relays index starting from index 500 . . . . .	82
5.11	Peak-to-average load (a) and delay (b) for two configurations, NN routing . . . . .	82
5.12	Peak-to-average load (a) and delay(b) for two configurations, min delay routing . . . . .	83
6.1	Direct route versus directed route . . . . .	89
6.2	(A) Broadcast time evolution in hyperfractal vs linear regime: inflexion point. (B) Contagion propagation speed on the line of level 0. . . . .	99
6.3	3-D city map modeling in QualNet . . . . .	101
6.4	Direct (green) versus diverted (red) path between source and destination, $d_F = 3, n = 200$ . . . . .	102
6.5	Validation of bounds for direct route, constant speed, (A), (B), (C). Validation of bounds for diverted route, constant speed, (D), (E), (F) . . . . .	103
6.6	Validation of bounds for $v$ increasing with level: a) $d_F = 3$ , direct route, b) $d_F = 3$ , diverted route, c) $d_F = 3.75$ , direct route, d) $d_F = 3.75$ , diverted route . . . . .	104
6.7	Validation of bounds for $v$ decreasing with level: a) $d_F = 3$ , direct route, b) $d_F = 3$ , diverted route, c) $d_F = 3.75$ , direct route, d) $d_F = 3.75$ , diverted route . . . . .	105
6.8	Snapshots of information dissemination in a Hyperfractal, healthy nodes in red ‘*’, infected nodes in black ‘o’ . . . . .	106
6.9	Broadcast time: simulation vs. theoretical results for (a) $d_F = 3$ , (b) $d_F = 3.33$ , (c) $d_F = 3.75$ , (d) $d_F = 5.33$ . . . . .	108
6.10	Speed proportional to the level . . . . .	109
6.11	Speed inversely proportional to the level . . . . .	109

# List of Tables

2.1	Simulation parameters . . . . .	26
2.2	Mobility class estimation accuracy. . . . .	27
2.3	MSE state distribution . . . . .	28
6.1	PHY, MAC, application and environment parameters configuration in Qual-Net . . . . .	100

# Acknowledgements

It is a pleasure to thank the many people who made this thesis possible and made this PhD an unforgettable experience.

I would like to express my gratitude to my supervisors, Dr. Philippe Jacquet and Dr. Bartłomiej Błaszczyszyn, who were abundantly helpful and offered invaluable assistance, support and guidance. Special thanks to Philippe who has been not only a advisor but also a mentor, and with whom I spent many precious moments.

Deepest gratitude are also due to Prof. Bernard Mans, who taught me always to aim for the best publications.

Deepest gratitude are also due to Dr. Chung Shue Chen, who motivated me to do a PhD and who offered great advising during my master internship.

I wish to offer my regards to all of my friends at LINCS, Kasia, Jon, Andrea, Leonardo, Danilo, Niraj, Max, Maura, Michele, Andrian, Flavia, Francesco, Diego, Nathan for helping me get through the difficult times with a smile on my face and for the memorable times spent together. Thanks to Andreas for reminding me in the final and difficult last 100 meters of the meaning of the PhD life and its beauty with all the ups and downs.

Many thanks to Marco, Fabien, Anne, Lou, Quan, Alonso, Ellie and the rest of my math team in Nokia Bell-Labs. Also special thanks to my new team's members who made the last months of my PhD a Great Success: Rauli, Andrea, Anna, Ahlem, Luis, Fuad.

I wish to thank my family, in particular to my grandmother, who always supported me and motivated me to strive for the best. And special thanks to my aunt, Cami, for always being there. Many thanks to Marius for supporting me in the pursuit of a researcher career.

# Abstract

The modeling of wireless networks with stochastic geometry has become popular in the recent decades. By means of point processes, the positions of wireless infrastructure and users are represented with the aim of computing metrics of interest like capacity, routing delay, broadcast time, etc. This has been done successfully for technologies such as 3G/LTE/Wi-Fi yet, with the arrival of 5G NR, the necessity for rethinking the models for the communication scenario has become paramount.

In this thesis we present a novel model for the locations of devices in urban communications networks. The model combines stochastic geometry with fractal geometry and it is called “hyperfractal”. The model exists in two options: the option for modeling the densities of cars on streets and the option for modeling the densities and repartition of auxiliary communication infrastructure. We present in detail the proposed model and its basic properties. In order to complete the description of the model and advocate for its ease of use, we provide a method for computing the fractal dimension of cities.

The usefulness of the model is showcased throughout this thesis by several wireless networks applications. One application evaluates the achievable trade-offs between delay and energy consumption for a V2X network in urban environment modeled with hyperfractals. A second application consists into studying the broadcast in a V2V delay-tolerant network. Achievable limits are presented together with a phenomenon specific to hyperfractals: the teleportation phenomenon, which allows an acceleration of the broadcast.

# Les Hyperfractales pour la Modélisation des Réseaux sans Fil

Nous sommes à la veille d'une nouvelle révolution industrielle provoquée par l'Internet des Objets (IoT). Dans le but de rendre les villes plus intelligentes et de faciliter la vie de leurs habitants, de nouveaux scénarios de communication sont apparus qui nécessitent des performances améliorées et nous obligent à repenser la manière dont nous concevons et analysons les réseaux. Les nouveaux modèles doivent incorporer les caractéristiques de la société humaine en profitant de la quantité toujours croissante d'apprentissage poussée par l'émergence de l'intelligence artificielle.

Les villes intelligentes comprendront un nombre considérable d'appareils connectés et des scénarios de communication hétérogènes : des drones communiquant avec des bâtiments intelligents, des bus vers des arrêts d'autobus, des ambulances vers des bicyclettes, des véhicules vers des feux de circulation et entre eux. Les réseaux de véhicules constituent une partie importante du nouvel écosystème de communication émergeant dans une ville intelligente. Les communications vehiculaires existent dans plusieurs formes : dans leur forme la plus simple, les communications de véhicule à véhicule (V2V), ou sous une forme étendue, véhicule à infrastructure (V2I) ou même vehicule a tout (V2X).

Un réseau de véhicules, tel que le réseau *ad hoc* véhiculaire (VANET), peut facilement être transformé en un système d'information organisé sur l'infrastructure, de façon à ce que tout véhicule puisse participer à la collecte et à la communication d'informations utiles. À mesure que le nombre de réseaux véhiculaires continue de croître et crée maintenant des réseaux géants (avec des structures hiérarchiques et des types de nœuds divers), les interactions véhiculaires deviennent de plus en plus complexes. Cette complexité est encore exacerbée par les relations spatio-temporelles entre véhicules. La mobilité des véhicules sur les routes ne peuvent plus être adéquatement modélisées par des méthodes utilisées pour les générations précédentes du réseau.

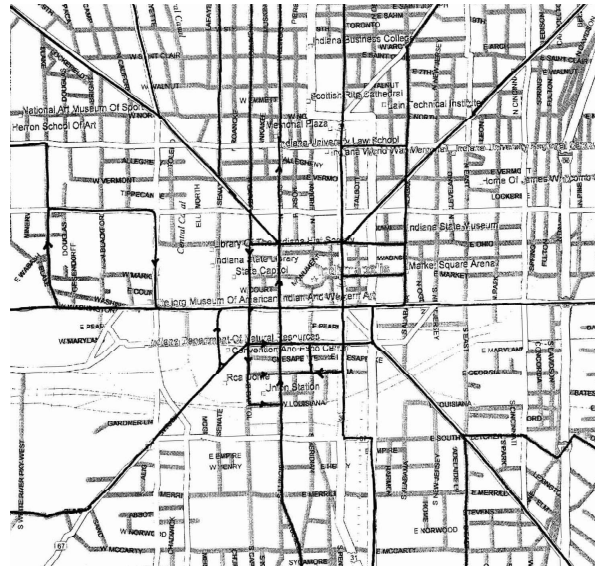


FIGURE 1: La carte de Indianapolis

Alors que les véhicules connectés suivent le déploiement de l'activité humaine, un modèle flexible devrait saisir les caractéristiques de la dynamique de la société humaine. Un département a des zones rurales à faible densité de population, tandis que les zones urbaines ont une forte densité de population, comme les villes et les villages. Les villes reflètent une auto-similarité statistique ou une hiérarchie des clusters [1]. Les villes sont organisées en quartiers, chaque quartier est organisé en pâtés de maisons, séparés par des rues. Les pâtés des maisons comprennent des bâtiments/maisons qui sont divisés eux-mêmes en pièces. Le concept d'auto-similarité, très présent dans la nature, a déjà été exploité depuis longtemps dans l'urbanisme et l'architecture [1, 2]. Comme les rues sont situées entre les bâtiments, la structure des rues et des routes dans une ville hérite de la nature auto-similaire de l'architecture urbaine et donc le trafic routier aussi (Figure 1).

Ce concept d'auto-similarité est particulièrement important. En mathématique, un objet auto-similaire, ou fractale, est un objet en géométrie qui montre une forte similarité soit exactement ou approximativement avec des parties plus petites de lui-même, le tout à la même forme qu'une ou plusieurs des ses pièces. Les fractales sont des objets qui présentent généralement des motifs similaires à des échelles de plus en plus petites et sont couramment utilisés pour décrire et simuler des objets apparaissant dans la nature. Dans ce sens, Mandelbrot a fait un travail remarquable.

Les éléments de réseaux sans fil ont été décrits en utilisant la géométrie stochastique, notamment, des processus ponctuels, qui permettent l'analyse des interférences et des retards réalisables, le débit, la planification efficace du réseau, etc. La géométrie stochastique a été particulièrement utilisée pour la modélisation de réseaux cellulaires, soit pour représenter les positions des stations de base soit pour les positions des utilisateurs mais aussi pour

la modélisation de réseaux *ad hoc*. Nous utilisons généralement des processus ponctuels qui supposent un caractère aléatoire complet, donc un processus ponctuel uniforme, à qui ajoutent des fonctionnalités telles que la répulsion ou le clustering (processus hard, processus Cox).

Les réseaux en treillis tels que le réseau de Manhattan [3] ont été utilisés pour la modélisation de réseaux *ad hoc* en milieu urbain, pourtant ces modèles ont été critiqués comme étant dans les extrêmes de la régularité. Dans l'analyse des réseaux véhiculaires, les modèles traditionnels supposent le cas limite de la géométrie de l'autoroute ou de la géométrie de l'intersection. L'absence de macro-modèles pour les villes est l'un des facteurs qui nous ont conduit vers le corpus de travail. Une étude que nous avons réalisée sur l'estimation de la mobilité des utilisateurs mobiles avec l'aide des informations fournis par le réseau montre que la géométrie de l'environnement a un impact énorme sur la mobilité d'un utilisateur.

Cette thèse présentera notre modèle de niveau macro pour la topologie sur laquelle évoluent des entités de communication véhiculaire dans les villes en exploitant l'auto-similarité. Le modèle est appelé hyperfractale et présente deux variantes : le modèle hyperfractale pour la densité des véhicules et le modèle des unités du bord de la route (RSU). Le modèle exploite l'auto-similarité de la carte de densité des entités de communication véhiculaire et évite les extrêmes de régularité et de hasard.

## 0.1 Les Modèles d' Hyperfractales

Dans tout environnement urbain, il existe une hiérarchie des rues basée sur leur importance dans le schéma d'urbanisation (boulevards, rues, ruelles). Le niveau qu'une rue occupe dans le plan d'urbanisation vient en conséquence de la densité de trafic qu'il supporte. Une observation intéressante et intuitive est que la longueur cumulée d'un type de rue diminue quand l'importance de la rue augmente. Par exemple, la longueur cumulée des boulevards est inférieure à la longueur cumulée des rues, qui, à son tour, est inférieure à la longueur cumulée des allées. Il est donc naturel que la densité moyenne du trafic par longueur cumulée de chaque type de rue suive une loi d'échelle de puissance. Dans ce qui suit, nous analyserons un cas particulier, lorsque la loi de puissance provient d'une distribution fractale. Les villes sont organiquement organisées en structures auto-similaires et représentent de bons candidats à être modélisés en utilisant la géométrie fractale.

Pour construire une fractale, Mandelbrot commence avec un objet géométrique appelé initiateur. A cela il applique un motif qui se répète à toutes les échelles en l'appelant le

générateur. La fractale est obtenue en appliquant le générateur à l'initiateur, en dérivant un objet géométrique qui peut être considéré comme composé de plusieurs initiateurs au niveau suivant de la hiérarchie ou de l'échelle inférieure. L'application du générateur à la nouvelle échelle entraîne une élaboration plus poussée de la géométrie de l'objet à une échelle encore plus fine, et le processus se poursuit donc indéfiniment vers la limite. En pratique, l'itération s'arrête à un niveau au-dessous duquel d'autres copies mises à l'échelle de l'objet original ne sont plus pertinentes aux fins de la modélisation. En substance, cependant, la vraie fractale n'existe que dans la limite, et donc ce que l'on voit à chaque itération est simplement une approximation de fractale.

Nous proposons d'utiliser notre modèle appelé hyperfractale, un modèle axé sur l'auto-similarité de la topologie. Le modèle hyperfractale permet d'échapper aux extrêmes de la régularité ou du hasard.

Le modèle proposé n'est pas une fractale mais une hyperfractale, en ce sens que la dimension est supérieure à la dimension de l'espace euclidien. De façon informelle, le modèle hyperfractale est un modèle de processus ponctuel de Poisson qui supporte une mesure avec des propriétés de mise à l'échelle différentes d'un ensemble fractale pur. Initialement, la carte est supposée être le carré unité. Le support de la population est une grille de rues similaire à une grille de Manhattan mais avec une résolution infinie. Un exemple est illustré par la Figure 2a. Dans la première étape, les lignes formant le niveau 0 sont dessinées en noir épais. Dans la deuxième étape, chacune des quatre zones obtenues est à nouveau considérée comme une carte indépendante avec une mise à l'échelle spécifique et les lignes formant le niveau 1 sont dessinées en noir plus fin. Le processus se poursuit de la même manière dans la troisième étape, où chacune des 16 zones est de nouveau divisée par 16 lignes tracées en traits noirs très fins.

La carte contient  $n$  noeuds mobiles. Le processus d'assignation des points aux lignes est effectué récursivement, de la même manière que le processus d'obtention du *Cantor Dust* [4]. Les deux lignes de niveau 0 forment une croix centrale qui divise la carte en exactement 4 quadrants. On note par  $p$  la probabilité que le noeud mobile soit situé sur la croix centrale selon une distribution uniforme et  $q = 1 - p$  la probabilité complémentaire. Avec une probabilité  $q/4$ , le mobile est situé dans l'un des quatre quadrants. La procédure d'assignation se poursuit récursivement dans chaque quadrant et s'arrête lorsque le noeud mobile est affecté à une croix de niveau  $m \geq 0$ . Un croisement de niveau  $m$  est constitué de deux segments de lignes de niveau  $m$  qui se croisent et chaque segment de la croix est considéré comme un segment de niveau  $m$ . Deux segments appartenant à la même ligne sont nécessairement de même niveau.



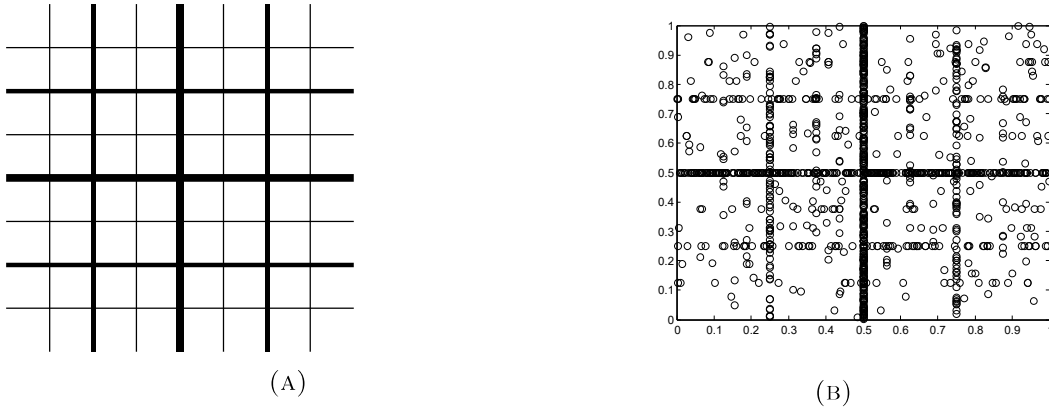


FIGURE 2: (A) Le support; (B) Hyperfractale,  $d_F = 3$ ,  $n = 1,200$  noeuds;

Une rue de niveau  $H$  consiste en l'union de segments consécutifs de niveau  $H$  dans la même ligne. La longueur d'une rue correspond à la longueur du côté de la carte. La Figure 2b montre la population obtenue dans le processus d'assignation des rues après 4 itérations. Comme on peut facilement le constater, la densité de la population diminue quand le niveau de la rue augmente.

En prenant la densité de l'unité pour la carte initiale, la densité des noeuds mobiles dans un quadrant est de  $q/4$ . Soit  $\lambda_H$  la densité des noeuds mobiles affectés sur une rue de niveau  $H$ . Il satisfait:

$$\lambda_H = (p/2)(q/2)^H$$

La mesure, dans le sens de Lebesgue, qui représente la densité réelle des noeuds mobiles dans la carte a de fortes propriétés d'échelle. La plus importante est que la carte dans son ensemble est reproduite à l'identique dans chacun des quatre quadrants, mais avec un poids de  $q/4$  au lieu de 1. La mesure a donc une structure qui rappelle la structure d'un ensemble fractale, tel comme la carte du Cantor [4]. Une différence cruciale réside dans le fait que la dimension fractale ici,  $d_F$ , est en fait *plus grande* que 2, la dimension euclidienne. En effet, considérer la carte dans seulement la moitié de sa longueur consiste à considérer la même carte mais avec un poids réduit d'un facteur  $q/4$ . On obtient:

$$\left(\frac{1}{2}\right)^{d_F} = q/4 \quad \text{thus} \quad d_F = \frac{\log(\frac{4}{q})}{\log 2} > 2$$

Cette propriété ne peut s'expliquer que via le concept de mesure. Notez que lorsque  $p \rightarrow 0$ ,  $d_F \rightarrow 2$  et que la mesure tend vers la mesure uniforme dans le carré de l'unité. En d'autres termes, une hyperfractale avec une valeur asymptotique de  $d_F = 2$  est un processus ponctuel de Poisson uniforme.

Des analyses typiques de la géométrie aléatoire ont été faites pour le modèle d'hyperfractale pour les noeuds. En quelques mots, les auteurs ont :

- initié le développement de la méthodologie de la géométrie stochastique et des outils pour manipuler le modèle hyperfractale afin de faciliter d'autres études sur les communications entre dispositifs à grande échelle.
- initié la dérivation d'outils pour le calcul ultérieur de métriques d'intérêt et facilite le chemin pour une étude plus approfondie du modèle : la notion de point typique, Campbell-Mecke, le principe de Mass-Transport, la transformée de Laplace.

### 0.1.1 Un Modèle de Propagation qui Génère la Nécessité d'Elargir le Modèle Topologique. L'Effet Canyon

Le modèle de propagation *canyon* implique que le signal émis par un nœud mobile ne se propage que dans la rue où il se trouve. Si le réseau est statique, compte tenu du processus de construction donné, la probabilité qu'un nœud mobile soit placé dans une intersection passe à zéro lorsque la largeur de la rue passe à zéro et les nœuds positionnés sur deux rues différentes ne peuvent jamais communiquer. Notez que lorsqu'une rue a une largeur positive, la largeur de l'intersection est négligeable par rapport à la longueur de la rue et le réseau sera toujours partitionné.

### 0.1.2 Le Modèle Hyperfractale pour les Relais

Il n'est pas surprenant que les emplacements des infrastructures de communication en milieu urbain présentent également un comportement auto-similaire. Nous appliquons donc un autre processus hyperfractale pour sélectionner les intersections où un relais de communications est installé.

La procédure d'attribution des relais aux intersections est illustrée de manière intuitive dans la Figure 3.

Notons  $\pi$  une probabilité fixe et  $q' = 1 - \pi$  la probabilité complémentaire. Une étape de sélection d'une intersection nécessite deux processus: le processus dans le quadrant et le processus dans le segment. La sélection commence par le processus dans le quadrant : avec la probabilité  $\pi^2$ , la sélection est le croisement central des deux rues du niveau 0. Avec la probabilité  $\pi(1 - \pi/2)$ , le relais est placé dans l'un des quatre segments de rue du niveau 0 commençant à ce point : Nord, Sud, Ouest ou Est, et le processus se poursuit

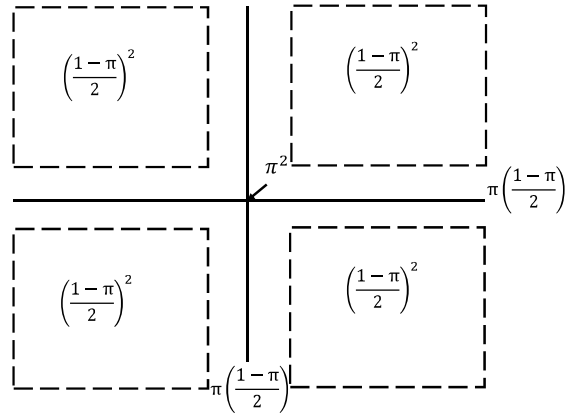


FIGURE 3: La procédure d'emplacement des relais

sur le segment avec le processus en cours. Sinon, avec la probabilité  $(1 - \pi/2)^2$ , le relais est placé dans l'un des quatre quadrants délimités par la croix centrale et le processus in-quadrant continue récursivement.

La sélection est effectuée  $M$  fois. A chaque cycle, la probabilité qu'une intersection entre deux rues de niveaux respectifs  $H$  et  $V$  soit sélectionnée est  $p(H, V) = \pi^2 \left(\frac{1-\pi}{2}\right)^{H+V}$ .

Si un croisement est sélectionné plusieurs fois, un seul relais est installé dans le croisement respectif. Le nombre de passages  $M$  est une variable de Poisson de la moyenne  $\rho$ . Par conséquent, une intersection de niveau  $(H, V)$  a la probabilité  $\exp(-\rho p(H, V))$  de ne pas avoir de relais et les événements relatifs à chaque intersection sont indépendants.

Le placement du relais est hyperfractal avec la dimension  $d_r$ :

$$d_r = 2 \frac{\log(2/q)}{\log 2}.$$

Une carte complète avec des noeuds et relais est présentée en Figure 4.

## 0.2 Des Applications pour les Réseaux sans Fil

### 0.2.1 Procédure de Validation avec des Données

Une exigence obligatoire lors de la fourniture d'un nouveau modèle pour les réseaux sans fil est le développement d'une procédure qui permet la transformation des données dans le modèle avec des paramètres de modèle spécifiques. Des procédures de traitement ponctuelles typiques de l'ajustement des données ont été développées dans la communauté de

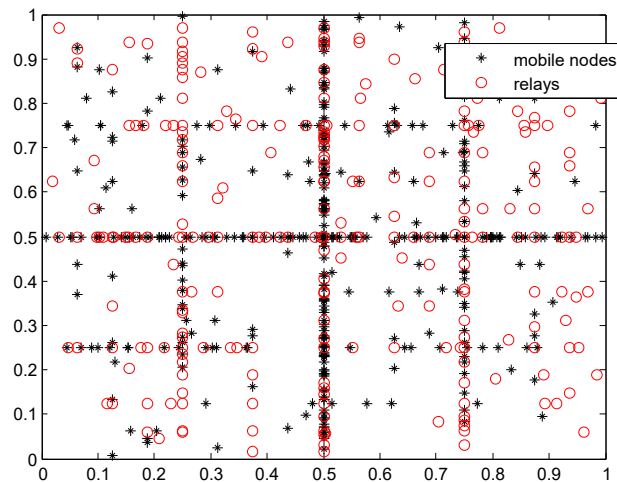


FIGURE 4: Carte avec noeuds et relais

recherche sur la base des différentes méthodes. Par exemple, dans R, un langage couramment utilisé par la communauté de la géométrie stochastique, les fonctions permettent d'ajuster les points à plusieurs types de processus : Poisson, Strauss, Softcore, etc. Malheureusement, les procédures existantes d'ajustement des données ne peuvent pas être utilisées pour le modèle hyperfractale car l'interaction entre les points est différente et ne peut pas être reconnue par le logiciel existant.

Pour valider notre modèle et prouver son utilité et sa facilité d'utilisation, nous avons développé une procédure de transformation des cartes de flux de trafic en hyperfractales, plus précisément le calcul de la dimension fractale des cartes de flux de trafic. On peut utiliser une telle procédure pour calculer une dimension fractale d'une ville / région, puis calculer des métriques d'intérêt. Un exemple de ces métriques est l'heure de diffusion.

Soulignons que dans la définition du modèle hyperfractale, nous n'avons pas fait d'hypothèses ou de conditions sur les propriétés de géométrie telles que la forme. Le modèle n'a besoin que de densité et de longueur. Par exemple, une hyperfractale n'a pas besoin que les rues principales / de premier niveau soient en croix ou qu'il existe exactement deux rues de niveau 1 qui ont la longueur exacte. Ce qui est nécessaire est la mise à l'échelle entre la longueur des différents niveaux du support. En tenant compte de ces observations (qui viennent naturellement du processus de construction), nous élaborons maintenant une procédure de calcul de la dimension fractale d'une carte de densité de trafic.

La procédure peut être adaptée en ajoutant trois critères pour augmenter la précision de l'ajustement : à savoir, densité-longueur, densité d'intersection spatiale et intersection d'intervalle de temps.

## Les critères de densité à longueur et le calcul de la dimension fractale

C'est le critère utilisé pour calculer la dimension fractale de la carte.

La procédure pour le calcul de la dimension fractale a les quatre étapes suivantes.

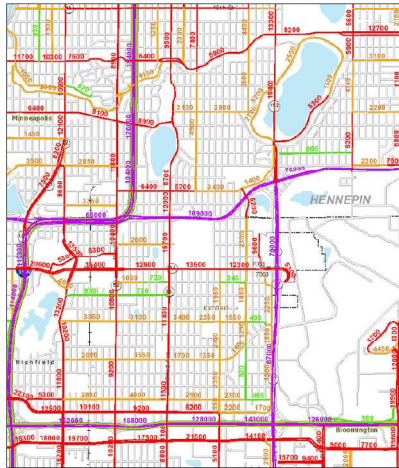
- Nous commençons par recueillir les données, la longueur des rues et les statistiques de trafic. Par exemple, nous avons utilisé les statistiques de trafic annuelles moyennes.
- Ensuite, nous considérons une seule rue comme un alignement de segments consécutifs dont les densités, du segment le moins dense au segment le plus dense, ne varient pas plus que d'un facteur  $A > 1$ . Nous appelons la densité de la rue la densité moyenne de son segment. Dans un modèle de ville hyperfractale pure, nous avons  $A = 1$ . Ceci est assez similaire au concept standard de quantification.
- L'étape suivante consiste à classer les rues par ordre décroissant de densité et à calculer le vecteur des sommes cumulées des segments de rues ordonnés par leur densité décroissante.
- Nous établissons ensuite la densité des rues triées par rapport à la longueur cumulée des rues triées. En parallèle, nous traçons la fonction de répartition de densité avec une valeur de départ de  $d_F$  et en utilisant la mesure de la longueur cumulée et par ajustement de courbe, déterminons la meilleure approximation pour  $d_F$ .

Il existent d'autres critères pour la validation de calcul de la dimension fractale.

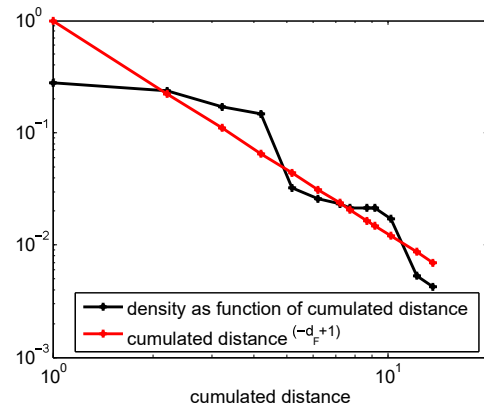
Enfin, pour illustrer comment le modèle hyperfractale peut être utilisé pour représenter la distribution des véhicules dans les rues, nous présentons ici quelques résultats d'ajustement des données.

### 0.2.2 Etude de la Vitesse de Propagation de l'Information dans un Réseau Urbain Tolérant aux Retards

La première application est la vitesse de propagation de l'information d'une diffusion dans un réseau urbain tolérant aux retards qui est déconnecté à tout moment, c'est-à-dire où les chemins multipistes de bout en bout n'existent pas (nécessitant un modèle d'acheminement différé). Nous prouvons des limites sur le temps de diffusion moyen dans une configuration hyperfractale et montrons que la performance est due en partie



(A) Instantané de la carte du trafic de Minneapolis



(B) Calcul de la dimension fractale

FIGURE 5: Procédure pour Minneapolis

à un phénomène auto-similaire intéressant, que nous dénotons comme téléportation de l'information, qui résulte de la topologie et permet une accélération de la temps de diffusion.

On a développé des borne inférieurs et supérieurs pour le temps de broadcast d'un paquet d'information dans un réseaux vehiculaire representé une hyperfractale.

Dans ce travail, nous utilisons le processus d'hyperfractale pour les noeuds comme modèle pour les emplacements des véhicules dans le réseau. Nous n'utilisons pas ici le processus pour les relais, fait qui conduira à la génération du réseau tolérant aux délais. Etant donné l'absence des relais, la propagation des paquets à travers les intersections, même à l'aide de la mobilité, nécessitera l'existence de tampons pouvant contenir le paquet plus longtemps.

Les mobiles se déplacent sur les lignes qui supportent la carte hyperfractale. Lorsqu'un nœud atteint une limite, il retourne à la carte du même point, suite à une mobilité de billard. Au départ, dans un souci de simplicité, la vitesse des mobiles est considérée comme constante et identique,  $v$ , quel que soit le niveau et la densité des nœuds sur les lignes.

Ici encore, nous utiliserons l'effet canyon comme phénomène de propagation caractéristique en milieu urbain. Le protocole de diffusion considéré est single-hop broadcast, ce qui signifie que chaque véhicule transporte l'information pendant son voyage et cette information est transmise aux autres véhicules dans son voisinage immédiat (voisins les plus proches du nœud infecté) lors du prochain cycle de diffusion.

Après les dérivations des bornes supérieures et inférieures sur le temps moyen de diffusion, on arrive au résultat unifiant suivant.

**Corollary 0.1.** *Le temps de diffusion moyen  $T_{broadcast}$  lorsque  $n \rightarrow \infty$  satisfait:*

$$\lim_{n \rightarrow \infty} \frac{\log T_{broadcast}}{\log n} = 1 - \delta \quad (1)$$

avec  $\delta = \frac{1}{d_F - 1}$ .

En étudiant la propagation épidémique de l'information dans les hyperfractales, nous avons découvert le phénomène de téléportation de l'information.

Dans un processus de point de Poisson uniforme bidimensionnel, le paquet d'information se répand uniformément comme un disque complet qui se développe à un débit constant, ce qui coïncide avec la vitesse de propagation de l'information. Fait intéressant, dans une hyperfractale, le phénomène est complètement différent, en raison de l'effet canyon et de la répartition de la population spécifique au nouveau modèle, comme illustré en Figure 6.

Deux contagions de nœuds infectés sur les lignes de niveau 0 sont mises en évidence. Ces zones ne sont pas connectées à la zone infectée principale sur la ligne d'où elles proviennent, la ligne de niveau  $H = 0$ . Les nœuds de ces zones sont infectés en recevant le paquet de nœuds circulant sur des lignes perpendiculaires. Cela génère plusieurs zones de contagion. Sur cette ligne, le paquet est diffusé à partir de toutes les sources de contamination apparues et la diffusion est accélérée. C'est un phénomène qui caractérise de manière unique la diffusion dans les configurations hyperfractales.

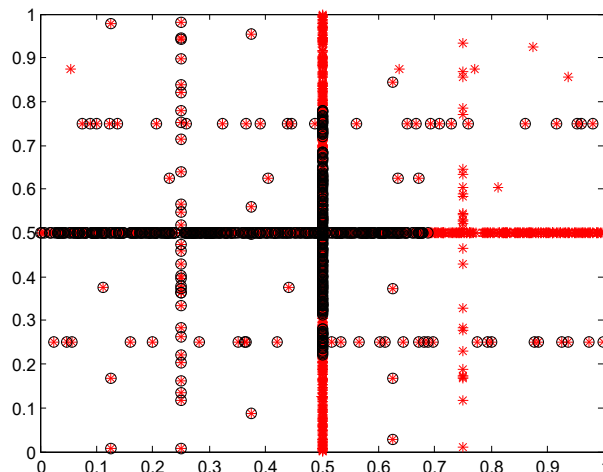


FIGURE 6: La téléportation d'information

Le phénomène de téléportation permet une accélération du temps de diffusion. Notez que l'accélération elle-même est un phénomène auto-similaire et prend place récursivement: la propagation au niveau  $H_i$  est accélérée par la téléportation provenant des lignes  $H_{i+1}$ ,  $H_{i+2}$ ,  $H_{i+3}$  et ainsi de suite. Dans un hyperfractal avec téléportation, le temps de diffusion évolue comme:  $\mathcal{O}(n^{1-\delta})$ .

Toutes ces analyses ont été validées par des simulations effectuées dans un simulateur auto-développé dans MatLab mais aussi en QualNet.

### 0.2.3 Le Routage de Bout en Bout dans un Réseau Hyperfractale avec Relais

La deuxième application est le routage de bout en bout dans un réseau hyperfractale avec relais représentant les unités de bord de route dans les communications V2I (véhicule à infrastructure).

Les modèles hyperfractaux pour les nœuds et les relais conviennent parfaitement à l'analyse des performances clés des réseaux ad hoc en milieu urbain. Dans ce qui suit, nous montrerons comment, en modélisant un réseau de véhicules avec des unités côté route en utilisant des hyperfractales, des calculs peuvent être effectués afin d'observer le compromis entre l'énergie de bout en bout et le retard. Cela plaide également pour l'utilité de nos modèles.

Dans l'étude des réseaux ad hoc et des sous-catégories de réseaux de véhicules ad hoc, la topologie apparaît fréquemment comme un facteur déterminant dans le calcul de l'énergie ou du délai de bout en bout. Par conséquent, il est tout à fait naturel d'utiliser les modèles hyperfractaux pour l'analyse de telles mesures.

La stratégie de routage considérée est la stratégie de routage du plus proche voisin. Le saut suivant est toujours le prochain voisin dans une rue, c'est-à-dire qu'il n'existe aucun autre nœud entre l'émetteur et le récepteur.

Nous définissons le **délai de transmission de bout en bout** comme le nombre total de sauts que le paquet prend sur son chemin vers la destination.

La transmission se fait en mode semi-duplex, un nœud n'est pas autorisé à émettre et à recevoir pendant le même intervalle de temps. Le signal reçu est affecté par le bruit de bruit gaussien blanc additif (AWGN)  $N$  et la perte de chemin avec exposant  $\alpha > 2$ . Nous faisons l'hypothèse simplifiée que tous les nœuds d'une rue transmettent la même puissance nominale  $P_m$  qui ne dépend que du nombre de nœuds de la rue.



Notons par  $t$  un noeud et par  $P(t)$  la puissance de transmission nominale de ce noeud.

**Definition 0.2.** Soit  $\mathcal{T}$  une suite de noeuds qui constitue un chemin de routage. La longueur du chemin est  $D(\mathcal{T}) = |\mathcal{T}|$ . Les chemins énergétiques pertinents sont les suivants:

- L'énergie cumulée de chemin est la quantité  $C(\mathcal{T}) = \sum_{t \in \mathcal{T}} P(t)$ .
- L'énergie maximale de chemin est la quantité  $M(\mathcal{T}) = \max_{t \in \mathcal{T}} P(t)$ .

L'énergie cumulée de chemin présente un intérêt puisque nous souhaitons optimiser la quantité d'énergie dépensée dans la communication de bout en bout, et respectivement l'énergie maximale du chemin lorsque nous voulons trouver le chemin dont l'énergie maximale ne dépasse pas un seuil donné en fonction de la durabilité énergétique des noeuds ou du protocole. Par exemple, il est probable qu'aucun noeud ne puisse supporter une puissance nominale de  $P_{\max}$  qui est l'énergie nécessaire pour transmettre dans une plage correspondant à la longueur totale d'une rue. Dans ce cas, il est nécessaire de trouver un chemin qui utilise des rues avec suffisamment de population pour réduire la puissance nominale du noeud.

Nous montrons les limites théoriques pour le compte de bonds de communication de bout en bout sous deux contraintes d'énergie différentes : soit l'énergie totale accumulée, soit l'énergie maximale par noeud. Nous avons en outre calculé une limite inférieure sur la capacité de débit du réseau avec des contraintes sur l'énergie du chemin.

Les résultats sont obtenus en observant le comportement du routage dans un chemin direct, un chemin dévié avec trois segments, soit un chemin dévié avec cinq segments (Figure 7).

Regardons la Figure 8 pour comprendre les compromis entre l'énergie cumulée de bout en bout et le nombre de sauts pour un couple émetteur-récepteur. La paire a été sélectionnée au hasard parmi les simulations effectuées sur une carte hyperfractale avec  $n = 800$  noeuds, coefficient de perte  $\alpha = 4$ , dimension fractale des noeuds  $d_f = 4,33$  et dimension fractale des relais  $d_r = 3$ . Le tracé montre l'énergie cumulée minimale pour la transmission de bout en bout pour un nombre fixe et autorisé de sauts,  $k$ , dans les marqueurs de cercle rouges. Notez que l'énergie ne diminue pas de manière monotone, car forcer à prendre un chemin plus long peut ne pas permettre de prendre le meilleur chemin. Cependant, en considérant l'énergie minimale cumulée de tous les chemins *jusqu'à un certain nombre de sauts*, (les marqueurs d'étoiles noires dans la Figure 8), l'énergie diminue et montre clairement le comportement attendu. En d'autres termes, l'énergie cumulée minimale diminue effectivement lorsque le nombre de sauts est autorisé à croître (et la communication de bout en bout est autorisée à choisir des chemins plus longs, mais moins coûteux).

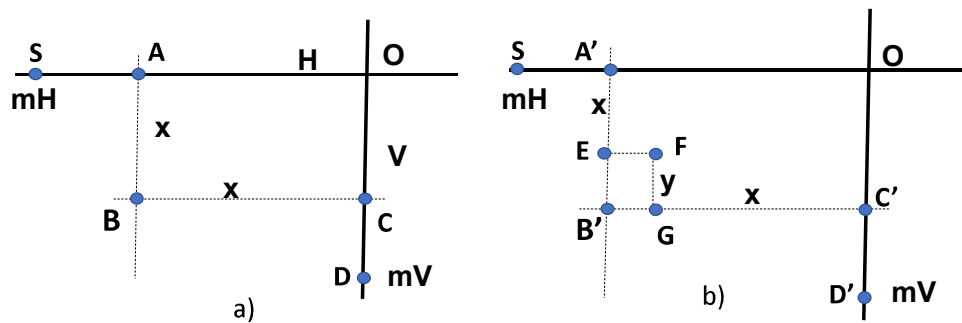


FIGURE 7: a) Chemin dévié avec trois relais fixes (à gauche), b) cinq relais fixes (à droite).

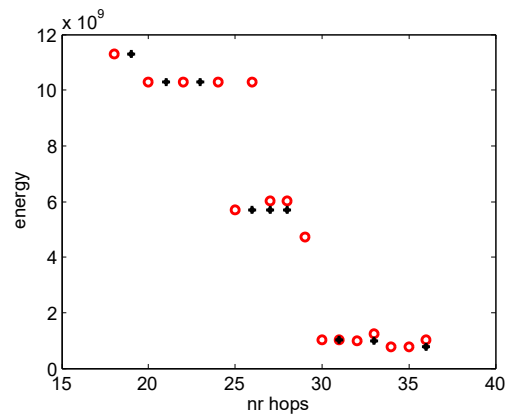


FIGURE 8: Énergie de bout en bout minimale cumulée par rapport aux sauts pour une paire émetteur-récepteur.

Toutes ces analyses ont été validés par des simulations effectuées soit dans un simulateur auto-développé dans MatLab, soit dans QualNet.

#### 0.2.4 Goulot d'Étranglement

Une autre analyse a été effectuée pour observer le goulot d'étranglement dans les stratégies de routage considérées.

Notez que, désormais, nous utilisons le terme nœud pour désigner à la fois les mobiles et les nœuds et les relais.

La charge  $\gamma(x)$  d'un nœud  $x$  est le nombre de chemins routés via le nœud respectif. Nous ne fournissons pas analytiquement une technique de routage telle que la charge soit

équilibrée. Au lieu de cela, nous calculons ici la charge des nœuds de transmission sous la contrainte du routage des coûts de chemin minimum (soit la technique de routage vers le plus proche voisin, soit un délai minimum).

Bien que la stratégie de routage ne soit pas optimale en ce qui concerne l'équilibrage de la charge, nous la choisissons comme technique de routage de référence afin de mieux comprendre la charge obtenue lors de la minimisation des coûts. De plus, une technique de routage à délai minimal est intéressante car elle maximise le débit du réseau.

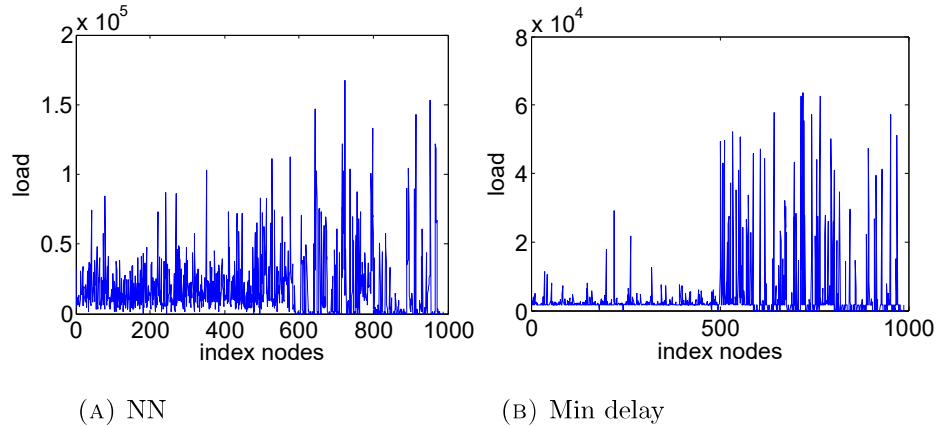


FIGURE 9: Répartition de la charge dans un hyperfractal avec  $d_f = 3.3$ ,  $d_r = 2.3$ , index des noeuds jusqu'à l'index 500, index des relais à partir de l'index 500

Lorsque vous utilisez la stratégie de routage à délai minimal, la distribution de la charge change considérablement, voir la figure 9b. Pour la même configuration hyperfractale,  $d_f = 3.2$ ,  $d_r = 2.3$ , les relais sont fortement chargés, tandis que les nœuds mobiles supportent un trafic beaucoup plus léger.

Nos résultats ont montré que la charge est mieux équilibrée lorsque la dimension fractale des relais est plus élevée.

# Chapter 1

## Introduction and Motivation

### 1.1 Technological Context

During the last few years we have witnessed some of the intense moments in the evolution of communication networks and I consider myself lucky to have my PhD work in this period. It is in the past three years that we stopped talking of telecommunications networks in the user-to-network sense of communication but started exploring the new vast fields opened by the “emancipation” of the object aka “object”. The main new challenge is not to make people communicate, but allow smart objects to exchange messages for decreasing the pressure and amount of human supervised communications.

The main concept sparking this revolution is the Internet of Things (IoT), that has brought with itself the concepts of Industry 4.0 [5] and Vehicular Communications [6]. Yet these are not considered to be under the umbrella of the mobile communications in a traditional sense. The discussions around the goals of the 5th Generation (5G) of communications have lead to the idea that there will be a logical split (overlapping exists) between the so-called composing slices of the new communication system. The slices are as follows: the evolution of Long Term Evolution (LTE) becomes the Enhanced Mobile Broadband (EMB), the second slice is the massive IoT and the third slice is the slice of the ultra-reliable and low latency communications with their tough constraints.

Nokia, together with all major players in the ICT (Information and Communications Technology), believes that the IoT has the potential to ignite a new industrial revolution because it will simplify peoples’ lives, make cities smarter and industries more efficient [7]. Bell Labs Consulting estimates IoT’s worth to be 36 times the potential value of today’s Internet by year 2020.

An intelligent infrastructure takes in account the behavior and necessities of the citizens. This leads to smarter, safer and more sustainable cities. Technology aims to make cities respond faster to demographic and economic changes and adjust easier to these shifts. However, smarter infrastructure and applications only make a difference when they actually make people's life better and easier, and not more complicated. The user is no longer to adapt his consuming mode to the network, but the network must adapt its services in order to better serve the user. One can argue that, by increasing the number of applications and social services, the social interactions between humans have decreased. Also, by increasing the number of connected devices that people have to handle (smart phone, smart watch, tablet, bluetooth, etc), the manipulation of the objects has become a nuisance and has lead to a waste of energy and attention. That is why a responsive, flexible technology that works for humanity will make cities indeed "smart", creating a safer and sustainable environment.

### **Challenge: The pressures of urban growth**

At the turn of the 20th century, just 15% of the world population lived in cities. According to the United Nations (UN), the year 2007 witnessed the turning point when more than 50% of the world population were living in cities, for the first time in human history [8]. The urbanization is estimated to reach 70% percent in 2070 [9].

The global population shift to urban areas creates new challenges for cities: better ways to promote a growing economy, improve operating efficiency, and maintain the safety and well-being of citizens. We must, now more than ever, address the city's impact on the environment. Although it is commonly understood that smart city services can address these challenges, the best path to developing them is often unclear and communications are often disregarded when migrating towards a smart city infrastructure.

As Figure 1.1 shows, in a smart city, tremendous amount of communications are happening simultaneously: drones can communicate with buildings, buses with bus stops, traffic agents with traffic poles, traffic lights with vehicles. Notice how often the vehicles appear in the 5G communications scenarios. Indeed, the driverless car initiatives push towards the development of vehicular communications in all of their options: vehicle-to-vehicle (V2V), vehicle-to-infrastructure (V2I), vehicle-to-everything (V2X).

More than 1.25 million people die on the roads each year, with 90 percent of cases being caused by human error [10]. The national departments of transportation want to increase safety for travelers and roadside workers. It is believed that automated driving supported by V2X communications has the potential to save lives by preventing millions of traffic

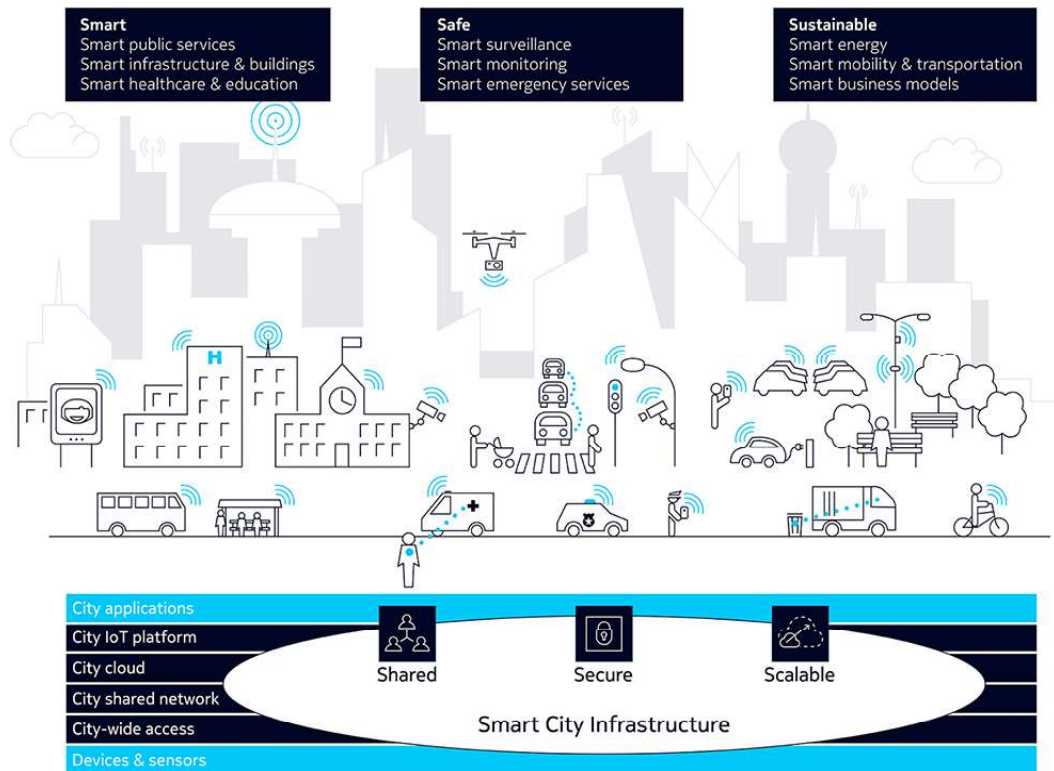


FIGURE 1.1: Property of Nokia Networks: Smart Cities that Enrich Life

accidents. Connectivity with other vehicles and pedestrians, centralized cloud-based back-office systems, traffic control centers and roadside equipment are to enable services such as danger warnings, cooperative adaptive cruise control, platooning and more. Real-time communication helps vehicles deal with situations that neither the driver nor the vehicle's built-in sensors can identify, enabling safer and predictive driving. Safety-critical V2X use cases for highways demand a latency below 100 ms end-to-end; in some situations even 50 ms latency is required. Such demands are not supported by today's cellular networks and highway agencies do not hold licenses to operate cellular networks along their highways. Furthermore, the 3G/4G networks are not adapted for communications along roads or highways. An IEEE 802.11p-based radio technology, also referred to as Dedicated Short Range Communication (DSRC) or Intelligent Transport Systems (ITS)-G5, is seen as an alternative to V2X over cellular (C-V2X) [11]. But that requires building a costly new footprint of DSRC-infrastructure along the highways and adding another new dedicated DSRC-communication module in addition to existing cellular modems that are already embedded in many vehicles.

Nokia identified some of the demanding requirements of the highway and automotive industry as follows:

- Robust end-to-end latency for safety-critical V2X use cases below 20 ms;
- Enabling predictive driving based on a long-distance view beyond the range of in-vehicle sensors and direct vehicle-to-vehicle communication;
- Greater network capacity to support multimedia services for traveler comfort in addition to safety-critical V2X use cases;
- Improved network coverage through a neutral host approach by leveraging existing highway infrastructure, e.g. toll gantries, for mounting cellular antennas of communications service providers and existing communications networks of highway agencies for backhauling;
- Building upon telecommunications standards to integrate V2X into existing cellular modems that are already embedded in many vehicles;
- Alignment with the 5G technology roadmap including LTE-Advanced, LTE-Vehicular and others.

In an intelligent transportation system (ITS), V2I sensors also called road-side units (RSU) can capture infrastructure data and provide travelers with real-time advisories about such things as road conditions, traffic congestion, accidents, construction zones and parking availability [12]. Nevertheless, one of the main functionalities of the infrastructure is assisting in the vehicular communications. V2I communication is typically wireless and bi-directional: data from infrastructure components can be delivered to the vehicle over an ad hoc network and vice versa. Such V2I sensors can include overhead RFID readers and cameras, traffic lights, lane markers, streetlights, signage and parking meters. Considerations have been made for dedicated infrastructure, yet a more economic sensible way of assisting the vehicular communications is to exploit the already existing telecommunications and traffic poles. The design of the topology of the RSU is therefore closely tied to the deployment of the vehicular communications and the vehicular traffic.

Given the number of connected devices, stochastic geometry remains a good ally in providing the tools needed for computing metrics in networks of this size.

## 1.2 Motivation

Future communication scenarios have a heterogeneity and diversity that is no longer answered by the stochastic geometry models designed for 3rd Generation (3G) or 4th Generation(4G) communications. Indeed, at the time of 3G/4G, the requirements for the design of topological models for networks were the robustness and adaptability to all scenarios. In 3G/4G, these scenarios meant mostly mobile communications between individuals. In 5G, as earlier stated, this is no longer the case. Another constraint that models designed for 3G/4G communications had to deal with was the lack of data for fitting the models or adapting the models for the specific scenarios. Nowadays, the the world of artificial intelligence and massive machine learning, the huge amount of data allows for the development of models that can be adapted and fine-tuned for each scenario and situation. We are no longer in the moment where we ask: “Would your model work for day time and night time as well? Rush hour and business hours? ” Machine learning and data analysis allow for real-time recalculation of models parameters in order for the models to fit with a maximum precision the reality and offer extremely accurate estimation of metrics for the exploitation of a communication network.

With these considerations in mind, we set ourselves to the design and exploration of new topological models for some specific communication scenarios in 5G. While learning from the tremendous bouquet of knowledge gathered in the stochastic geometry community while working for the 4G communication models, we allow ourselves to dive into new spaces, in particular, observing and getting inspiration from the fascinating fractal geometry.



### 1.3 Contributions and Structure of the Thesis

In this thesis, we propose a novel stochastic model for representing car traffic in urban environment. The model is analyzed and exploited. By combining stochastic geometry with fractal geometry, this new model aims for a more realistic representation of human activity in cities. The structure of this thesis is organized as follows.

The present chapter is **Chapter 1**.

**Chapter 2** overviews the state-of-the-art in classic stochastic geometry models applied to wireless communications. First, we review the Poisson point process, the most commonly used model for wireless networks and remind its basic properties and tools. Secondly, we present state of the art works on wireless network models, as well as seminal works done in the community. We briefly present our preliminary work done for the mobility estimation by using means of stochastic geometry. This work has lead to useful observations that were some of the generators behind the hyperfractal model idea.

In **Chapter 3**, we start by revisiting basic notions about fractals and we present a pioneering work done by Philippe Jacquet in the modeling the locations of sensor networks with fractals, as an example of some of the first such works done in wireless networks. Then, we introduce **the main contribution** of this thesis, the hyperfractal model for urban networks. The model has two components: (i) the model for mobile nodes and (ii) the model for infrastructure. The hyperfractal model for nodes is described, together with its properties and tools that we derived in order to handle the model. Then, we present the hyperfractal model for relays. Again, we present the tools we have derived for handling the models and a metric relevant for the model that we computed as an example of how to use these tools. We further present our preliminary work of generalization of the models in classic stochastic geometric model.

**Chapter 4** presents our method for fitting the model with real traffic traces and real city maps. In particular, we describe an algorithm that computes the fractal dimension of an actual city from street length and traffic traces. Several examples are presented in detail.

In **Chapter 5**, we present a first application of the hyperfractal model studied during this thesis, the modeling and evaluation of the energy consumption and delay in an end-to-end transmission performed in a vehicular network with relaying infrastructure. The chapter terminates by analyzing the load of the routing links and identifying the bottleneck.

**Chapter 6** presents a second application of the hyperfractal model studied during this Ph.D, the modeling and evaluation of the information dissemination. We observe that

when the relaying infrastructure is not used, the network is disconnected and the information propagates like in a delay tolerant network. An interesting phenomenon in this model is debated, what we call information teleportation phenomenon, that is characteristic to hyperfractals and arises as a consequence of the scaling law of the population in the model.

Finally, **Chapter 7** presents the concluding remarks, on-going works and opens the path for future exploration of the model and its capabilities.

## 1.4 Publications

### Under Peer Review

[J1] **Dalia Popescu**, Philippe Jacquet, Bernard Mans, Robert Dumitru, Andra Pastrav, Emanuel Puschita, “Information Dissemination Speed in Delay Tolerant Urban Vehicular Networks in a Hyperfractal Setting”, submitted

[C1] **Dalia Popescu**, Bartłomiej Blaszczyszyn, Philippe Jacquet, “Stochastic geometry of some fractal models for urban vehicular networks”, submitted

### In Proceedings

[C2] Philippe Jacquet, **Dalia Popescu**, Bernard Mans, “Energy Trade-offs for End-to-End Communications in Urban Vehicular Networks Exploiting an Hyperfractal Model”, ACM International Conference on Modeling, Analysis and Simulation of Wireless and Mobile Systems, October 2018

[C3] Philippe Jacquet, **Dalia Popescu**, Bernard Mans, “Broadcast Speedup in Vehicular Networks via Information Teleportation”, IEEE Conference on Local Computer Networks (LCN), October 2018

[C4] **Dalia Popescu**, Philippe Jacquet, “Vehicle to Infrastructure Communications Design in Urban Hyperfractals”, International Workshop on Signal Processing Advances in Wireless Communications, SPAWC 2018

[D1] Demo “Fractals and Hyperfractals for Wireless Networks” for Nokia 5G Smart Campus Event

[C5] Philippe Jacquet, **Dalia Popescu**, “Self-similar Geometry for Ad-Hoc Wireless Networks: Hyperfractals”, Geometric Science of Information, 2017

[C6] Milan Bradonjic, Philippe Jacquet, **Dalia Popescu**, “Energy Savings for Virtual MISO in Fractal Sensor Networks”, 55th Annual Allerton Conference on Communication, Control, and Computing, 2017

[C7] Philippe Jacquet, **Dalia Popescu**, “Self-similarity in urban wireless networks: Hyperfractals”, Workshop on Spatial Stochastic Models for Wireless Networks (SpaSWiN), 2017

[C8] Aravinthan Gopalasingham, **D.G Herculea**, Chung Shue Chen, Laurent Roullet, “Virtualization of Radio Access Network by Virtual Machine and Docker: Practice

and Performance Analysis”, IFIP/IEEE International Symposium on Integrated Network Management May 2017

[C9] Majed Haddad, **D.G Herculea**, Eitan Altman, Nidham Ben Rached, Veronique Capdevielle, Chung Shue Chen, Frédéric Ratovelomanana, “Mobility State Estimation in LTE”, 2016 IEEE Wireless Communications and Networking Conference, Doha, 2016, pp. 1-6.

[C10] **D.G Herculea**, Chung Shue Chen, Majed Haddad, Véronique Capdevielle , “Straight: stochastic geometry and user history based mobility estimation ”, July 2016 HotPOST '16 @ MobiHoc

### **Posters, Public Talks, etc**

LINCS Internal Workshops, 2016, 2017, 2018

Journées Spécifiques Pôle RESCOM — GDR RSD — CNRS: Journée Thématique sur les Réseaux Véhiculaires

## Chapter 2

# Classic Stochastic Geometry

In mathematics and telecommunications, stochastic geometry models of wireless networks refer to mathematical models based on stochastic geometry that are designed to represent aspects of wireless networks [13]. The models generated with the help of tools of stochastic geometry and related fields like point processes, spatial statistics, geometric probability, percolation theory, etc. are further analyzed with the aim of better understanding wireless communication networks and accurately predict various network performance metrics.

In the 1960s, a pioneering stochastic geometry model [14] was developed to study wireless networks. This was followed by models based on geometric probability [15, 16]. Later the use of these models increased significantly and they became massively used for studying a number of wireless network technologies including mobile ad hoc networks, sensor networks, vehicular ad hoc networks, cognitive radio networks and several types of cellular networks, such as heterogeneous cellular networks [17, 18]. Key performance and quality of service quantities are often based on concepts from signal processing such as the signal-to-interference-plus-noise ratio (SINR), which forms the mathematical basis for defining network connectivity and coverage.

The principal motivation behind the usage of these stochastic geometry models is that it is acceptable to assume that the locations of nodes or the network structure are random in nature due to the size and unpredictability of users in wireless networks. Furthermore, the size of the objects is negligible when considered in comparison to the size of the network. The use of stochastic geometry tools can allow for the derivation of closed-form or semi-closed-form expressions for these quantities without resorting to exhaustive, time-consuming simulations or to deterministic models which are limited and possibly incorrect.

Some of the key quantities that are usually studied with the help of stochastic geometry are the following:

- *SINR*, signal to noise plus interference ratio [19]. Due to the scarcity of radio resources, several transmissions are always concurrent and the SINR is the main KPI for the decision of correct reception at the receiver side.
- *Coverage* is a major factor in mobile network planning, as a good coverage is the critical requirement in the deployment of networks.
- *Network capacity* is very relevant in mobile architecture design and resource planning. It is crucial to estimate the capacity that can be delivered to users in order to guarantee a good quality of service and in order to prevent from any user to be in outage.
- *Shot noise* [20]. Stochastic geometry has been often motivated for the study of wireless networks by the need to understand the type of noise that arises in electronics. An example of use of stochastic geometry is the tool for finding the average of the sum of functions of a point process, Campbell's formula [21], which will be reminded several time throughout this manuscript.
- *Network interference as shot noise* began to be studied once the Fourier and Laplace transform techniques were developed [22]. The tools were necessary for analyzing the interference experienced by a user in a wireless network in which the locations of the (interfering) nodes or transmitters are positioned according to a Poisson process.
- *SINR coverage and connectivity models* [23] were proposed in late 2000s in the framework of stochastic geometry.

## 2.1 Notions of Classic Stochastic Geometry

### 2.1.1 Model fundamentals

A wireless network consists of nodes that transmit and receive the data inside the network: base stations and users in a cellular network for phone communications, sensor nodes in a sensor network, IoT devices, drones, cars, etc. Before going into the development of stochastic geometry models and tools for the analysis of the wireless networks, more fundamental models are required for mathematically representing the signal propagation and the node positioning. For instance, one of the first steps is the modeling of the radio propagation. The choice of these models takes into account the environment, wireless network type, technology used (microwave/millimeter-wave), specific architecture (cellular/ad-hoc/etc), channel/medium access control (MAC) protocol, which controls the channels and, hence, the communicating structures of the network.

One of the building blocks of a stochastic geometry wireless network model is the *propagation model*. As electromagnetic signals (waves) propagate through air (and other materials) at an elevated frequency, they are negatively affected by multipath propagation. This is due to reflection, refraction, diffraction and dispersion generated when signals collide with obstacles such as buildings. Realistic and easy models to handle with are needed for the propagation. A common approach is to consider two separate parts: the random and deterministic, or non-random, components of signal propagation. The deterministic component is usually represented by some path-loss or attenuation function that uses the distance propagated by the signal from its source for modeling the power decay of electromagnetic signals. The function is as follows:  $l(|x - y|) = |x - y|^{-\alpha}$ , where the path-loss exponent  $\alpha > 2$  and  $|x - y|$  denoted the distance between point  $y$  and the signal source at point  $x$ . The random component's aim is to capture the effect generated by the absorption and reflection. This effect is called fading and some of the models are: Rayleigh (exponential), log-normal, Rice, Nakagami, etc.

The second and most important task in stochastic geometry network models is choosing a fit mathematical model for the location of the network nodes and the interaction between them. The standard assumption is that the nodes are represented by points, idealized due to their small size in comparison to the size of the network, in some space, most often, two-dimensional Euclidean, which means they form a stochastic or random structure known as a spatial point process.

Let us further overview some basic notions of point processes and other tools in stochastic geometry as they will be frequently used throughout this manuscript. Most of these notions have been taken from [24–26].

The most basic objects studied in stochastic geometry are point processes. Visually, a point process can be depicted as a random collection of points in space. More formally, a point process (PP) is a measurable mapping  $\Phi$  from some probability space to the space of point measures (a point measure is a measure which is locally finite and which takes only integer values) on some space  $\mathbb{G}$ . Each such measure can be represented by a discrete sum of Dirac measures on  $\mathbb{G}$ . In the following, we will only refer to the space  $\mathbb{R}^d$ .

A few dichotomies concerning point processes on Euclidean space  $\mathbb{R}^d$  that will be relevant in the development of this manuscript are as follows:

- A point process can be *simple* or not. It is simple if the multiplicity of a point is at most one, no two points are at the same location.
- A point process can be *stationary* or not. The process is stationary if its distribution is invariant by translation through any vector  $v \in \mathbb{R}^d$ , i.e.  $\mathbf{P}\{v+\Phi \in \Gamma\} = \mathbf{P}\{v+\Phi \in \Gamma\}$  for any  $v \in \mathbb{R}^d$  and  $\Gamma$ .
- A point process can be *Poisson* or not. A formal definition of the Poisson point process (PPP) is given in the following subsection. A Poisson point process offers a handy computational framework for different quantities of interest.
  - The homogeneous Poisson point process is stationary and simple. This may be considered as the simplest (and most natural) point process.
  - The framework for non-homogeneous Poisson point process is also well developed, although more technical than that of the homogeneous case. They can be used to model distributions of users which are not uniform across space.
  - There is also a comprehensive computational framework for stationary point processes which are not Poisson. This is Palm calculus [17].
- A point process can be *isotropic* or not. Isotropy holds if the law of the point process is invariant to rotation. The homogeneous Poisson point process is isotropic. If a point process is isotropic and stationary, it is called motion-invariant.
- A point process can be *marked* or not; marks assign labels to the points of the process, and they are typically independent of the point process and independent and identically distributed. The study of marked point processes may require the handling of Palm calculus.



### 2.1.2 Poisson Point Process

**Definition 2.1.** Let  $\Lambda$  be a locally finite measure on  $\mathbb{R}^d$ . A point process  $\Phi$  is said to be Poisson with intensity measure  $\Lambda$  if for all pairwise disjoint sets  $B_1, \dots, B_k \in \mathcal{B}$ , the random variables  $\Phi(B_1), \dots, \Phi(B_k)$ ; i.e.,  $\forall n_1, \dots, n_k \in \mathbb{N}$

$$P(\Phi(B_1) = n_1, \dots, \Phi(B_k) = n_k) = \prod_{i=1}^k e^{-\Lambda(B_i)} \frac{\Lambda(B_i)^{n_i}}{n_i!}$$

**Definition 2.2.** If  $\Phi$  is a Poisson point process on  $\mathbb{R}^d$  with intensity measure  $\Lambda(dx) = \lambda dx$  where  $\lambda \in \mathbb{R}_+^*$  and  $dx$  denotes the Lebesgue measure, then  $\Phi$  is called a homogeneous Poisson point process of intensity  $\lambda$ .

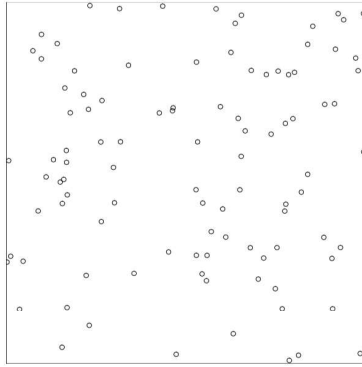


FIGURE 2.1: Poisson point process

#### Typical Point

The notion of *typical point* is particularly important for a point process, as it is comprised in the definition and derivation of most of the tools. The typical point is meant to simplify computations as a computation done for the typical point should be representative for all points in the process. One cannot simply pick a point uniformly from an infinite number of points, and if a rule defines how to pick such a point, we introduce biasing since the rule will have to depend on the point's vicinity (or some other property of the point process realization).

The typical point is strongly connected to the notion of Palm distribution [17]. One can interpret the Palm distribution of  $\Phi$ ,  $P^0$ , as the conditional probability given that  $\Phi$  has a point at the origin. The intuition behind the existence of the typical point is: the conditional distribution of points “seen” from the origin given that the process  $\Phi$  has a point there is exactly the same as the conditional distribution of points “seen” from an

arbitrary location  $x$  given that  $\Phi$  has a point at  $x$ . In this context,  $P^0$  (resp.  $P^x$ ) is often called the distribution of seen from its “typical point” located at 0 (resp. at  $x$ ).

**Distance towards the nearest point of a Poisson point process**, also called the contact distribution is formulated as follows.

Let  $\Phi$  be a homogeneous Poisson point process on  $\mathbb{R}^d$  with intensity  $\lambda$ . For a given  $x \in \mathbb{R}^d$ , let  $R = \inf_{X \in \Phi} |X - x|$ ; Note that:

$$P(R \geq r) = P(\Phi(B(x, r)) = 0) = e^{-\lambda k_d r^d}$$

where  $B(x, r) = \{y \in \mathbb{R}^d : |y - x| < r\}$  and  $k_d$  is the volume of the unit ball in  $\mathbb{R}^d$ .

### Laplace transform

Let  $\Phi$  be a Poisson point process on  $\mathbb{R}^d$  with intensity measure  $\Lambda$ . Then for all measurable functions  $f : \mathbb{R}^d \rightarrow \mathbb{R}_+$ ,

$$\mathcal{L}_\Phi(f) = \mathbf{E} \left[ e^{(-\int_{\mathbb{R}^d} f d\Phi)} \right] = \exp \left( - \int_{\mathbb{R}^d} (1 - e^{-f}) d\Lambda \right)$$

**Campbell-Mecke averaging formula for Poisson point process** gives a method for calculating expectations of sums of measurable functions  $f$  with ranges on the real line. Let  $\Phi$  be a process on  $\mathbb{R}^d$  with intensity measure  $M$ . Then for any measurable function  $f : \mathbb{R}^d \rightarrow \mathbb{R}$  which is either non-negative or integrable with respect to  $M$ , the integral  $\int_{\mathbb{R}^d} f d\Phi$  is almost surely well defined and

$$\mathbf{E} \left[ \int_{\mathbb{R}^d} f(x) d\Phi(dx) \right] = \int_{\mathbb{R}^d} f(x) M(dx)$$

### Mass Transport Principle (MTP)

This principle comes from graph theory and more precisely from unimodularity. We remind the reader we have introduced the notion of typical point in a point process. In which regards finite graphs, the typical vertex can be naturally defined as the vertex uniformly sampled from all vertices. Unimodular (infinite) graphs can be seen as graphs which exhibit enough regularity allowing one to come up with an equivalent notion of the typical vertex. A complete treatment of this subject can be found in [27]. The analogy from unimodular graphs to point processes has been done in [26]. Here, the most fundamental property of unimodular graphs, called the mass transport principle, has been extended to point processes. Based on this extension, one can now make use of

this property for the translation of properties from the typical point to all other points of the process. The mass transport principle for Poisson point process is formulated as follows.

For any translation invariant  $f(x, y, \Phi)$ ,  $(f(x + a, y + a, \Phi + a) = f(x, y, \Phi)$ , for any  $a$ ):

$$\mathbf{E} \left[ \sum_{x_i \in \Phi \cup \{x^0\}} f(x^0, x_i, \Phi \cup \{x^0\}) \right] = \mathbf{E} \left[ \sum_{x_i \in \Phi \cup \{x^0\}} f(x_i, x^0, \Phi \cup \{x^0\}) \right] \quad (2.1)$$

A clear example of Mass Transport Principle in wireless communications is the statement: the mean total rate received by a node is equal to the mean total transmitted rate.

### 2.1.3 Poisson Line Process

Let  $\mu$  be a locally finite measure on  $\mathbb{R} \times [0, \pi)$  invariant with respect to cylinder shears, then there exists a finite measure  $G$  on  $[0, \pi)$  such that

$$\mu(dr \times d\theta) = dr \times G(d\theta) \quad (2.2)$$

Let  $\Phi = \sum_{n \in \mathbb{Z}} \delta_{(r_n, \theta_n)}$  be a Poisson point process on  $\mathbb{R} \times [0, \pi)$  with intensity measure of the form (2.2). Equivalently  $\Phi$  is an i.i.d. marked stationary Poisson point process with intensity  $\lambda = G([0, \pi))$  and mark distribution  $G(d\theta)/G([0, \pi))$ . Then  $\Phi_d = \sum_{n \in \mathbb{Z}} \delta_{d(r_n, \theta_n)}$  is a Poisson line process.

### 2.1.4 Voronoi Tessellations

A tessellation is a collection of open, pairwise disjoint polyhedra or polygons in the case of  $\mathbb{R}^2$ , whose closures cover the space, and which is locally finite, i.e., the number of polyhedra intersecting any given compact set is finite [17].

A Voronoi diagram is a partitioning of a plane into regions based on distance to points in a specific subset of the plane. That set of points (called seeds, sites, or generators) is specified beforehand, and for each seed there is a corresponding region consisting of all points closer to that seed than to any other. These regions are called Voronoi cells.

Let  $\Phi_2$  be a simple stationary and ergodic point process on  $\mathbb{R}^2$  with intensity  $\lambda_2 \in \mathbb{R}_+^*$ . The Voronoi cell of each  $x \in \mathbb{R}^2$  is defined by:

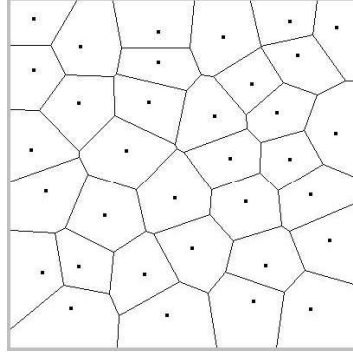


FIGURE 2.2: Voronoi tessellation

$$V(x, \Phi_2) = \{y \in \mathbb{R}^2 : |y - x| \leq \inf_{Z \in \Phi_2} |y - Z|\}$$

which is a convex set.

Voronoi tessellation-based models of cellular access network were considered to derive closed-form expressions for the mean number of users in a cell, the mean length of connections, and the total power received at the base station.

The work of [28] shows a relevant example of infrastructure modeling with tessellations and how environment geometry reflects into the telecommunication structure.

## 2.2 State of the Art of Stochastic Modeling of the Wireless Networks Topologies

In the past decades, the research community has successfully modeled network topologies by extensively using *Poisson Point Process (PPP)*. The seminal work of [29] has enriched the community knowledge on the achievable limits of capacity, routing, etc. Further works, e.g., [18, 30, 31], have studied in detail the routing and communication properties of these topologies.

In [32] the authors overview results driven by stochastic geometry and random graphs on connectivity, capacity, outage probability and other fundamental limits of wireless networks. The authors start by giving the mathematical preliminaries, basic notions, notations and properties of point processes, boolean models and random geometric graphs. Then, using stochastic geometric tools they characterize interference, outage and throughput. Basics of percolation and connectivity are reviewed in order to further pass to the

analysis of capacity. Other applications are also shortly reviewed such as routing, information propagation and secrecy. Different spatial stochastic models like Poisson point process, Poisson hard-core process, Strauss process and the perturbed triangular lattice are used in [33] to fit the locations of base-stations in cellular networks. The data was obtained from a public database. The authors introduce a metric called deployment gain in order to estimate the coverage performance achieved by a data set.

A Matern hard core process is used in [34] in order to model concurrent transmissions in carrier-sense multiple access (CSMA) networks. As the field of multi-tier and cognitive wireless networks received increased interest, the need for characterizing the interference in these new type of scenarios was answered in numerous works [35]. In [36], the authors provide an extensive survey on the literature related to stochastic geometry models for single-tier as well as multi-tier and cognitive cellular wireless networks. The authors overview the models and methods used for multi-tier networks together with the relevant metrics. Information dissemination within a network modeled by a Poisson point process has been studied (e.g. [37], [38])

As the study of *cellular networks with tools of stochastic geometry* became more intense, special attention has been given to enhancing the accuracy of the estimation of signal-to-interference-plus-noise-ratio (SINR). In this sense, the authors of [39] have shown that the SINR values experienced by a user with respect to different base stations are related to an instance of the two-parameter Poisson-Dirichlet process.

In the recent years we have experienced the emergence of *millimeter wave technology for the cellular networks*. Stochastic geometry again has proved its utility for modeling and analyzing the networks under the new technology and with the peculiarities of this technology. New frameworks have been specially tailored [40] including new path-loss model for the different distribution of line-of-sight and non-line-of-sight propagation considerations, blockage models that become crucial when handling millimeter wave systems and Monte Carlo simulations where the analytical tools had to be extended by fittings. Other works, for example [41], propose the use of Ginibre point process as a model for wireless networks with repulsion.

One of the first works that addresses the *modeling of vehicular networks by means of stochastic geometry* has been done in [42]. In that sense, the authors initiate the modeling of vehicular networks through a one dimensional network obtained as nodes randomly located on a straight line with slotted Aloha and nearest neighbor transmissions. They derive close formulas for the capture probability, the density of progress and the average

delay, relevant metrics for vehicular communications. The study is further extended in [43] and [44].

The authors of [45] develop a model for vehicular networks in two steps. First, they generate a Poisson line process to model the road infrastructure and, in the second phase, they generate independent Poisson Point processes on the lines, in order to model the locations of vehicles on road. They obtain therefore a Poisson Cow Point Process. The focus of [46] is the scenario of vehicle to vehicle and vehicle to infrastructure communications accounting for the clustering effect near the intersections.

In [47], the authors develop a model starting from two data sets, one from Beijing, representative for large cities, and one from the city of Porto, representative for small cities. By analyzing the empirical probability mass function of the point counts they find that the Log Gaussian Cox Process (LGCP) fits with good accuracy the data. Let us emphasize that the authors provide a model for the locations of random vehicles in cities, and do not take into account specific urban propagation phenomenons. Particular setups and results on information dissemination in vehicular networks have been proven in [48, 49], etc. The particular setup of highway has been studied under the constraints imposed by the millimeter wave technology in [50].

Some first attempts to combine the stochastic geometry with fractal geometry have been done in [51] and [52], where the authors use classic stochastic geometry to model the position of base-stations but fractal geometry to model the coverage.

More references will be given in each chapter for the specific application treated.

## 2.3 Mobility Estimation in Cellular Networks by Means of Stochastic Geometry

A preliminary study we have performed during the first part of the Ph.D period consisted in the estimation of mobile user equipment (UE) speed by exploiting network information and stochastic geometry. This study came as a continuation of the work on mobility estimation by means of signal processing with the intention to exploit network provided information and stochastic geometry. The lessons learned from this study were fundamental for the creation of the hyperfractal model.

UE's speed information is useful for optimizing handover (HO), reduce call drop or networking signaling flow, optimizing the UE-to-evolved NodeB (eNB) attachment and radio

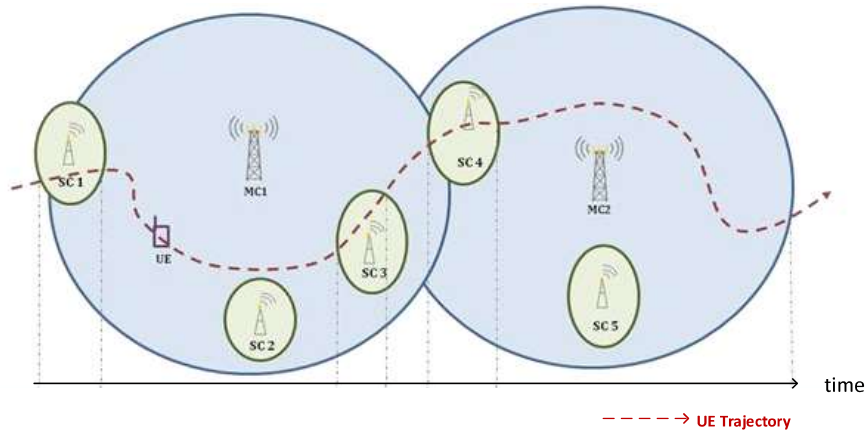


FIGURE 2.3: UE mobility through heterogeneous networks.

resource utilization efficiency, for example during channel allocation decision and in multi-carrier deployment scenarios. For instance, one may favor the HO of high-speed UEs to large coverage cells (e.g., macro cells) or to higher coverage carriers in multi-carrier scenarios. On the other hand, for macro cell traffic offloading purpose, low or medium speed UEs are preferred to HO to small cells, see Figure 2.3. It is also known that UE's speed information can be beneficial to the optimal configuration of HO parameters, for example in setting the filtering coefficients of power measurements, as well as for determining most suitable transmission scheduling strategy [53].

In this preliminary study, we address the problem of UE mobility estimation for the enhancement of HO procedure in mobile cellular networks. We propose a novel scheme to estimate the UE mobility class based on the behavior of the UEs in the network, the correlation between the mobility and the characteristics of the environment, and the UE history information available at the eNBs. We use stochastic geometry for network modeling. The method is following the Long Term Evolution (LTE) Mobility State Estimation (MSE) legacy model and has negligible additional computational complexity to the eNB and the UE.

### 2.3.1 Mobility State Estimation

There exists a rich literature on user speed estimation methods that are built on physical layer signal measurements and exploit signal processing techniques (see for example [54–56]). However, these methods are computational complex and not in line with the 3rd Generation Partnership Project (3GPP) legacy procedures. Most of these methods assume that the information of the reference signal received power (RSRP) strengths is available

anytime for the eNBs. In reality, RSRP are transmitted only periodically. Additionally, authors only consider constant speeds.

An approach of high interest to the industry is to exploit UE history information that is exchanged between eNBs during HO procedures (through the X2 interface). In 3GPP, the purpose of UE history information is to provide target eNB, with a list of UE's previously visited cells and associated (per-cell) information elements. As standardized, the UE history information contains the IDs of the last visited cells (up to 16), and the durations that the UE stayed in each cell (called the cell residence time). The goal is to use these information elements to derive UE mobility state with high accuracy, very low computational complexity, compatible to 3GPP standards and legacy architectures, and valid for various network environments.

### The 3GPP LTE MSE Procedure

The legacy LTE MSE procedure in 3GPP [57, 58] consists in counting the number of HOs (denoted by  $N_{HO}$ ) or re-selections (denoted by  $NCR$ ) that the UE does during a sliding time window (denoted by  $TCR_{\max}$ ), for categorizing the UE into one of three states: “Normal” (in this study we call it “Low”), “Medium” or “High”, with respect to the two MSE thresholds  $NCR_{\text{medium}}$  and  $NCR_{\text{high}}$  deployed as follows: If a UE's  $NCR$  count is smaller than the threshold  $NCR_{\text{medium}}$ , then the UE's mobility state is determined as “Normal”. If the UE's  $NCR$  is greater than  $NCR_{\text{medium}}$  but less than  $NCR_{\text{high}}$ , the UE's mobility state is determined as “Medium”. If the UE's  $NCR$  is greater than  $NCR_{\text{high}}$ , then the UE's mobility state is determined as “High” ( see Figure 2.4) .

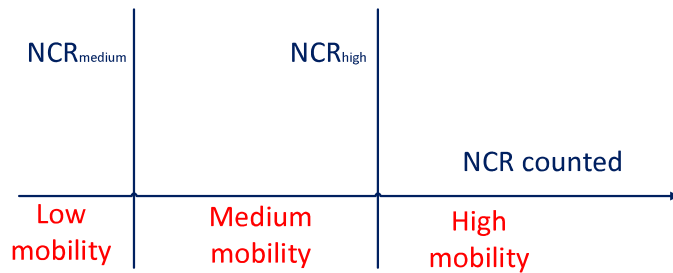


FIGURE 2.4: The 3GPP LTE MSE algorithm.

Note that the above standard procedure often leads to inaccuracy due to its over-simplified modeling and assumptions.



Enhancements to the legacy LTE MSE procedure have been proposed in several papers [59–61] and were debated in detail in our work published in [62]. We refer the reader to this piece of work for a detailed comparison.

### 2.3.2 System Model

The network consists of a number of  $M_C$  macro cells. The coverage area of each cell is represented by its Voronoi region. For our computation, we do not mean the radio range of a cell is limited by its Voronoi region. The locations of macro cell eNBs are extracted from the city of Cologne network topology and the resulting Voronoi regions are obtained as displayed in Figure 2.5.

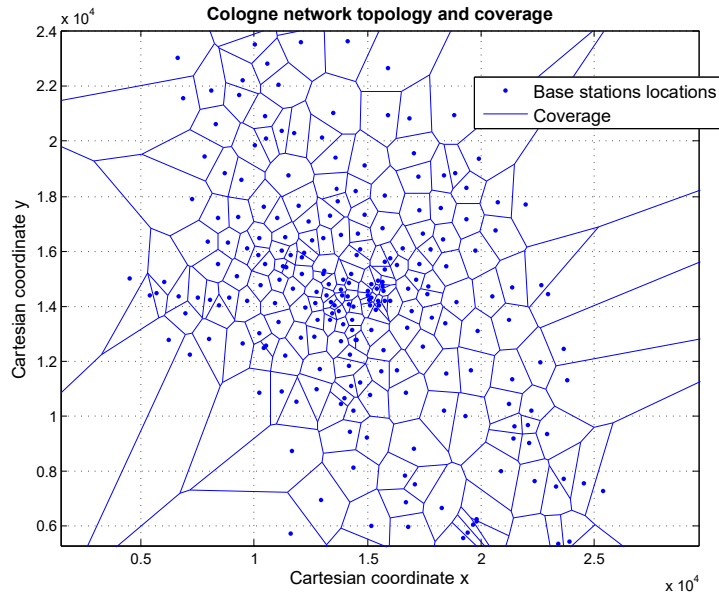


FIGURE 2.5: Macro cell network topology.

A set of UEs are extracted from the Kolntrace data [63]. At every time instance (with the resolution of 1 second), one has the following trace available from [63]: the Cartesian coordinates of UE  $k$  on the  $X$  and  $Y$  axes and the speed of UE in kmph. Given the above data and the network topology model, we can determine the time-stamp of HO to a cell and the time-stamp of HO from the cell. Meanwhile, we use  $T_h$  to denote the time spent by a user in a cell. The UE trajectories are the measured trajectories or simulated according to Kolntrace. Note that the traces contain UEs of various speed.

### 2.3.3 Stochastic Geometry and User History based Mobility Estimation: STRAIGHT

In [64], the authors propose a mobility estimator for cellular networks that is based on the following dependency between the UE velocity and average cell residence time:

$$\mathbf{E}[T_h] = \frac{\pi R}{2\mathbf{E}[V]} \quad (2.3)$$

where:  $T_h$  is the HO call cell residence time, defined as the time spent by a mobile in a given cell to which the call was handed over from a neighboring cell before crossing to another cell,  $R$  is the cell radius,  $V$  is the user speed. This expression assumes uniformly distributed mobiles in a cellular network and, secondly, the mobiles moving in straight lines with direction uniformly distributed in  $[0, 2\pi)$ . Equation (2.3) can be re-written as:

$$\mathbf{E}[V] = \frac{\pi R}{2\mathbf{E}[T_h]} \quad (2.4)$$

for showing that the user speed is proportional to the ratio of cell radius over the cell residence time.

The assumption of linear trajectory of UEs is clearly unrealistic. One can easily find that UEs have erratic trajectories and with many direction changes which will thus lengthen the cell residence time and lead to incorrect estimation of the UE's speed. As the time a UE stays in a cell depends not only on the UE's speed but also on its trajectory, we can interpret that the erratic trajectory can be translated into an increase in its travel distance.

From (2.4), one may also interpret  $\frac{\pi R}{2}$  as the average distance traveled by an UE in the cell and thus the increase in traveled distance would mean an increase to a notion of the cell radius, such that a "virtual" or equivalent cell radius should be used to replace the simple  $R$  in (2.4) for taking into account erratic trajectory or similar factor.

Figure 2.6 depicts the concept of equivalent cell radius. That is, a UE that has an erratic path through a cell  $i$  of radius  $R$  is similar to that the UE has a straight path through the cell with radius  $R_{eq}$ . In short, an increase in a UE's drift can be considered as contributing to an increase of the equivalent cell radius.

To be precise, let  $\eta$  be the "**stretch**" **parameter** defined as  $\eta = \frac{R_{eq}}{R}$ , where  $R$  is the actual radius of a cell and  $R_{eq}$  is the equivalent cell radius of the cell. It expresses a dilatation or stretch of the actual cell radius induced by the typical trajectories of the users in the cell.

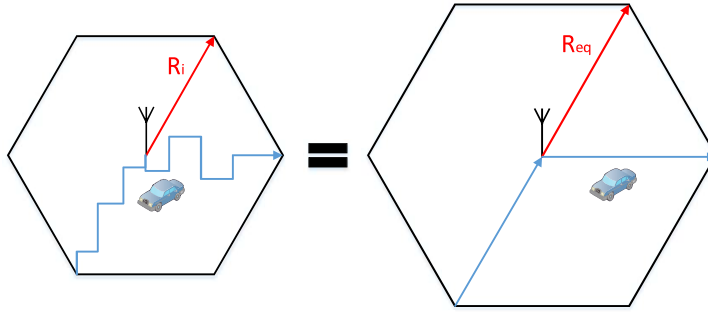


FIGURE 2.6: Principle of the equivalent cell radius.

By applying this transformation (i.e., using the notion of equivalent cell radius), we can resort to the straight path assumption and use equation (2.4) for estimating the UE's speed such that:

$$\mathbf{E}[V] = \frac{\pi\eta R}{2\mathbf{E}[T_h]} \quad (2.5)$$

where the parameter  $\eta$  would depend on the environment, network topology, and the characteristics of mobile UEs passing through the cell area. For example, we may have a specific value for each cell or a specific value for each type of cell. In addition, this parameter may have similar or correlated value among neighboring cells.

The main steps of the proposed UE's speed procedure are summarized in the following. During the **off-line** part each eNB builds the network topology map (Figure 2.5 is an example) in its memory. Furthermore, each eNB learns its own parameter  $\eta$ , the value of which can be shared with neighboring eNBs (through the X2 interface).

During the **on-line** part of the scheme, the mobility estimation is performed as follows. At the HO moment, the eNB inquires the user for the UE history information containing previous cell ID, and the residence time in the previous cell. Knowing the neighboring eNB's parameter value  $\eta$ , the eNB uses equation (2.5) to estimate the UE's speed in the previously visited cell. At last, the eNB classifies the speed to one of the three mobility classes defined by 3GPP.

### 2.3.4 Stretch Parameter Computation

To determine  $\eta$ , we propose two methods for the computation. Both of them include a learning phase. The two methods are different in the manner of computation of the cell radius.

The **first method** is based on the consideration that the locations of the eNBs are known and can be spread over the whole network. We consider the locations of ENBs are modeled by Poisson point process (PPP). Next, we draw the Voronoi tessellations accordingly and approximate the coverage area of each cell by its Voronoi region. The radius of each cell is computed by considering the area of the Voronoi cell, denoted by  $A$ . Using the value of  $A$ , we can draw a circle of equivalent area, whose radius is given by  $R = \sqrt{\frac{A}{\pi}}$ . It can have very different values as the actual cell size depends not only on the eNB transmission power but also on the physical environment and local geometry (e.g., rural or city center, etc.).

The computation is done as following: for each of the users in the training set, we compute the sojourn time in each cell. The average speed during the sojourn time is computed as the average over the speed measured in each second. Next, the stretch parameter for that cell when crossed by the particular car is computed. After the operation is done for each vehicle in the training set, the stretch parameter for each cell is computed as the average over all the values obtained for the particular cell. Note that this method leads to improved estimation accuracy as it computes a value of the cell radius for each cell. However, it would require additional computational complexity or cost to the eNB since each eNB must compute the Voronoi tessellations or broadcast throughout the network.

The **second method** for computing the radius of each cell again uses stochastic geometry modeling.

We use the interesting results presented in [65]. It states that the rate at which a Poisson point process (in  $\mathbb{R}^2$ ) with intensity  $\lambda$  crosses the  $x$  or  $y$  axis is given as  $Rate(\lambda) = \frac{4\sqrt{\lambda}}{\pi}$ .

Therefore, we denote the expected length of a typical line segment by  $\mathbf{E}(seg)$  and is obtained as:

$$\mathbf{E}(seg) = \frac{\pi}{4(\lambda)^{\frac{1}{2}}}$$

This is actually the mean traveled distance in a cell under a straight path assumption.

The expected length of a typical line segment can be computed by first computing the intensity of the PPP that generated the eNBs. For an increase in accuracy, the generating process can be considered as inhomogeneous, composed by three (or more) homogeneous processes (a different  $\lambda$  for each type of the environment). It is easy to observe that there exists a direct **dependency between the intensity of the generating PPP and the environment**. For example, a dense PPP is characteristic to urban environment, while a sparser process is characteristic for suburban/rural environment.

Parameter	Value
Environment type	urban, suburban, highway, rural
Macro cells	235, variable size
Trajectories	variable, experimental data
Speed	variable, from 0 to 120 kmph
No. of UEs used for learning	300 UEs
No. of UEs to test speed estimation	45 UEs
Time resolution of data in Kolntrace	1 second
LTE MSE $TCR_{max}$	30 seconds [59] for LTE MSE 1 100 seconds [66] for LTE MSE 2
LTE MSE $NCR_{medium}$	3
LTE MSE $NCR_{high}$	5

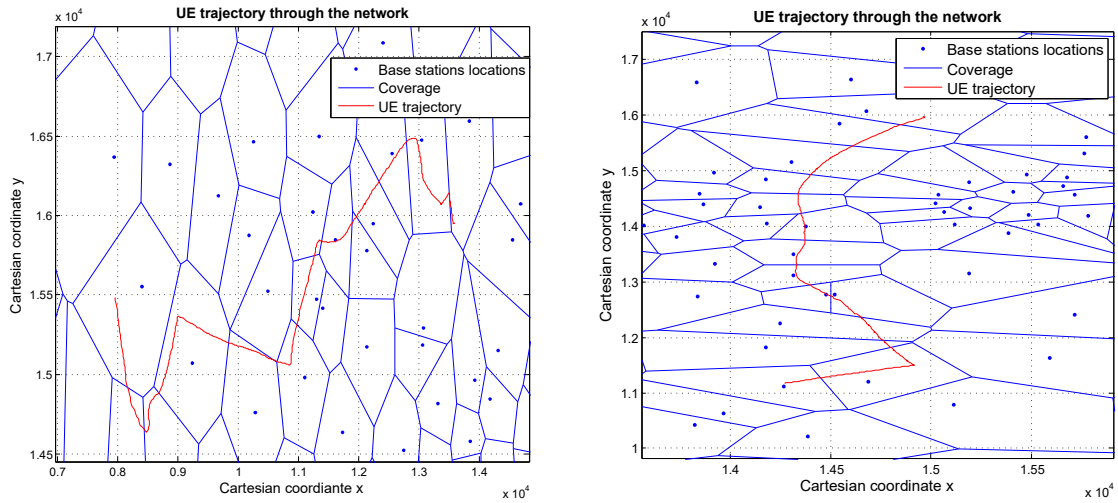
TABLE 2.1: Simulation parameters.

Now that we have the radius for each Voronoi cell, the parameter  $\eta$  can be learned through the same mechanism described for the first method. By considering the diameter of the cell to be the expected length of the typical line segment, the method requires only the knowledge of the parameter  $\lambda$  for each of the environment where the network is deployed. Therefore, the computational complexity is lower than that of the first method. However, since it uses the same value of cell radius for each environment type, the scheme may lead to lower accuracy in determining the cell radius also in computing the parameter  $\eta$ .

### 2.3.5 Performance Evaluation

We evaluate the mobility estimation using the mobility traces from [63]. Other parameters are shown in Table 2.1. LTE MSE procedure is evaluated with two parameter configurations, the standard one and the configuration used in more recent publications. Note that the network comprises 235 macro cells with variable cell size, covering diverse environments (city center, suburban, highway, and rural). The data is obtained from the Kolntrace project. Figure 2.7 shows the trajectories of two UEs throughout the macro cell network. One can see how erratic the trajectory a UE may be during a travel.

In this work, we present the performance results obtained by using the first method for the computation of the stretch parameter,  $\eta$ .



(A) UE 1 trajectory.

(B) UE 2 trajectory.

FIGURE 2.7: Examples of UE trajectories in the network.

TABLE 2.2: Mobility class estimation accuracy.

	STRAIGHT	LTE MSE 1	LTE MSE 2
Low Mobility Class	66%	95%	57.58%
Medium Mobility Class	37%	3.75%	43.13%
High Mobility Class	78%	4%	15.63%

According to 3GPP, the estimated UE's speeds will be classified into three mobility classes [57, 58]: Low Mobility Class from 0 to 40 kmph, Medium Mobility Class from 40 to 90 kmph, and High Mobility Class for speed exceeding 90 kmph.

As an illustration, Figure 2.8 shows the average speed of UEs when crossing cells  $M_8$  and  $M_{68}$ . An interesting observation is that the UEs crossing cell  $M_8$  are either in Low Mobility Class, either in Medium Mobility Class, while the UEs crossing cell  $M_{68}$  are either in Medium Mobility Class or High Mobility Class. That shows that even if the UE's speeds in one cell can vary considerably, the average values of the UE's speeds reside in two adjacent mobility classes. This observation is consistent with our thought that the environment has a strong impact on the mobility and speed of the user and its trajectory.

Table 2.2 shows the correct classification probabilities for the two algorithms. One can observe that the performance obtained by the LTE MSE procedure has high accuracy ( $> 90\%$  for the first configuration) for UEs with Low Mobility Class and obtains a dramatic drop for UEs of Medium and High Mobility Class. This is due to the fact that the LTE MSE with configuration 1 will tend to claim UEs in Low Mobility Class. The performances

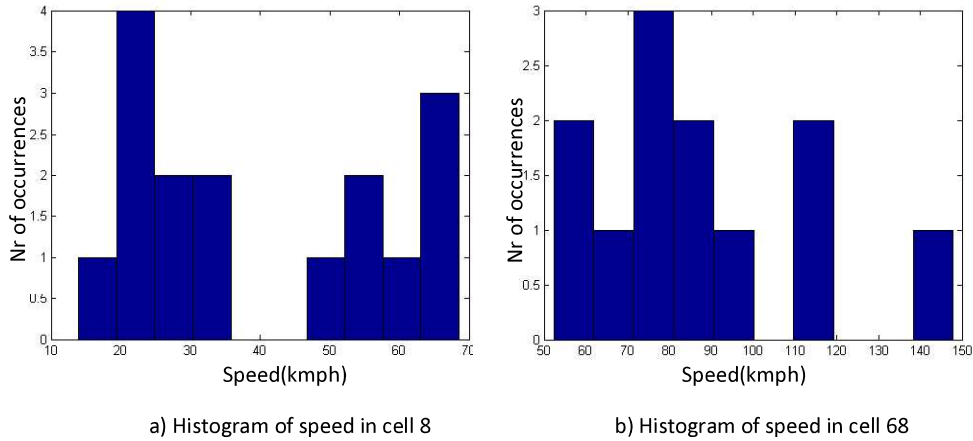


FIGURE 2.8: Histogram of UEs' speed in cells.

achieved by our proposed scheme clearly outperform LTE MSE 1 even when dealing with challenging situations of Medium and High mobility classes. For the second configuration of LTE MSE, STRAIGHT is outperformed in the medium mobility regime.

Further considerations are given by computing the MSE state distribution defined as the probability of a UE being estimated to be in a particular mobility state class. Table 2.3 shows the results obtained for our scheme and for LTE MSE scheme with the two configurations, in comparison. We denote STRAIGHT as A, LTE MSE configuration 1 as B and LTE MSE configuration 2 as C for reasons of space.

TABLE 2.3: MSE state distribution

	A	B	C	A	B	C	A	B	C
Low Mobility	66%	95%	57.5%	27.5%	95.63%	44.3%	0%	92%	50%
Medium Mobility	16.6%	4.5%	28.7%	37%	3.7%	43.1%	21.9%	3%	34.3%
High Mobility	16.6%	0%	13.6%	35%	0.6%	12.5%	78%	4%	15.6%

As an overall performance, the probability to be classified in the correct class is 60.33% for our scheme and 34, 25% for LTE MSE with configuration 1 and 38, 73% for LTE MSE with configuration 2 which clearly shows the superiority of the proposed scheme.

### 2.3.6 Lessons Learned

This section presented my work on UE's speed estimation based on the UE history information. The proposed algorithm can be easily applied to today's LTE or future cellular networks for enhanced UE's speed estimation accuracy. The method uses the UE cell sojourn time and also exploits the properties of UE mobility behavior and the physical environment. The results of simulations performed with realistic data have shown that STRAIGHT can provide a much better accuracy in comparison to existing legacy LTE MSE procedure and can satisfactorily estimate UE's speeds of various classes including low mobility class and also challenging situations of medium mobility class and high mobility class.

Furthermore, the study exploits the geometry of the network and shows that the trajectory of the user is dependent on the geometry of the environment. Here, we do not mean only the geometry of the environment in the sense mentioned earlier, where we specify that the size of the cells depends on the environment, but the erratic nature of the trajectory.

We made here a first observation that the trajectories of users are imposed by the architecture of the city and this impact is not a negligible one. Yet, at the time of this study, there were no methods for quantifying the environment geometry's impact on wireless networks and even less, on the environment's self-similarity reflection in the UE behavior in the network.

Again, as the scope of this subsection was to show how our motivation of considering more carefully the environment's geometry for the modeling of wireless networks was born, we have not presented here all the details of this work and we refer the reader to [62] for a detailed description of the algorithm and evaluation of performances.



## Chapter 3

# Self-Similar Geometry. The Hyperfractal Model

### 3.1 Self-similar Geometry. Fractals

Throughout this manuscript, the word “fractal” is used either as an adjective, either a substantive.

Fractal geometry was invented almost entirely by Benoit B. Mandelbrot in a period of time stretching over thirty years, starting with 1950. The fractals became easier to understand and accessible to everyone after their popularization in his most appraised work [4]. The increase of computational power awoke the interest for the science of form in the fields of physics and biology. Mathematicians too became interested in the possibility of using this new geometry for visualizing solution spaces of dynamic systems whose behavior could no longer be regarded as smooth, but discontinuous and chaotic. The fractal geometry revolves around the idea that the world is chaotic, discontinuous, irregular in its superficial physical form but that beneath this first impression lies an order which is regular, unyielding and of infinite complexity [1].

Fractals, such as the examples in Figure 3.1, are a forest of mathematical models for very irregular and detailed sets.

In [67], a fractal is defined as follows. “In mathematics, a self-similar object is exactly or approximately similar to a part of itself (i.e. the whole has the same shape as one or more of the parts). Many objects in the real world, such as coastlines, are statistically self-similar: parts of them show the same statistical properties at many scales. Self-similarity

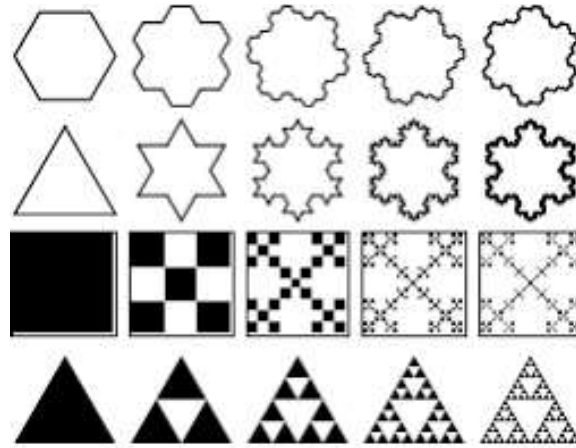


FIGURE 3.1: Gosper island, Koch snowflake, box fractal, Sierpiński sieve

is a typical property of artificial fractals. Scale invariance is an exact form of self-similarity where at any magnification there is a smaller piece of the object that is similar to the whole. For instance, a side of the Koch snowflake is both symmetrical and scale-invariant; it can be continually magnified three times without changing shape.”

To build a fractal, Mandelbrot starts with a geometric object called an initiator. To this he applies a pattern which repeats itself at every scale calling this the generator. The fractal is obtained by applying the generator to the initiator, deriving a geometric object which can be considered to be composed of several initiators at the next level of hierarchy or scale down. Applying the generator again at the new scale results in further elaboration of the object’s geometry at yet a lower scale. The process is continued indefinitely. In practice, the iteration stops at a level below which further scaled copies of the original object are no longer relevant for the purpose of the modeling. In essence, however, the true fractal only exists in the limit, and thus what one sees is simply an approximation to it.

Let us further explore the underlying meaning of fractals in order to better understand the motivation of using this model and the derivations that will further follow.

### 3.1.1 Fractal Dimension

To quantify the wilderness of fractals, one can use the notion of fractal dimension. There are many and more or less intuitive definitions of fractals and fractal dimension [68]. Note that there is not one complete definition of the fractal dimension. Several definitions exist together with methods for computing it. By using these definitions, one can obtain different values for some sets.

Dietrich Stoyan says in “Fractals, Random Shapes and Point Fields” [68]: “the mathematical theory of fractals is rather complicated, yet the methods of measurement of fractal dimension are easily understood, and they give the feeling of the underlying meaning.”

In order to better understand the notion of fractal dimension, we shall start by introducing the concept of topological dimension.

### **Lebesgue covering dimension or topological dimension**

The Lebesgue covering dimension or topological dimension of a topological space [69] is one of the ways of defining the dimension of the space in a topologically invariant way [70]. An open cover of a topological space  $X$  is a family of open sets whose union contains  $X$ . The ply or order of a cover is the smallest number  $n$  such that each point of the space belongs to at most  $n$  sets in the cover. A refinement of a cover  $C$  is another cover, each of whose sets is a subset of a set in  $C$ ; its ply may be smaller than, or possibly larger than, the ply of  $C$ . The covering dimension of a topological space  $X$  is defined to be the minimum value of  $n$ , such that every open cover  $C$  of  $X$  has an open refinement with ply  $n + 1$  or lower.

As an example, finite systems of points have topological dimension zero and curves have topological dimension one. In the case of infinite systems, it makes sense to make more subtle distinctions, therefore, introduce the fractal dimension.

We will present here some definitions given for fractals by Prof. Emma Carberry at MIT. We found these definitions relevant for our use of these concepts later throughout this manuscript. Note that these notions will be used several times throughout the manuscript.

**Definition 3.1.** A subset of  $\mathbb{R}^n$  is (affine) self-similar if a subset of this subset is mapped to the original subset by a nontrivial affine transformation :  $f(x) = \mathbf{A}x + \mathbf{b}$ , where  $\mathbf{A}$  is an  $n \times n$  invertible matrix and  $\mathbf{b}$  is an  $n$  dimensional vector. The transformation is known as a self-similarity transformation.

**Definition 3.2.** Given a self-similar set, we define the **fractal dimension**  $d_F$  of this set as  $\frac{\log k}{\log M}$  where  $k$  is the number of disjoint regions that the set can be divided into, and  $M$  is the magnification factor of the self-similarity transformation.

**Definition 3.3.** A fractal is a subset of  $\mathbb{R}^n$  that is self-similar and whose fractal dimension exceeds its topological dimension.

In the following, we will use the example of the Sierpinski triangle for a better understanding of the computation of the fractal dimension.

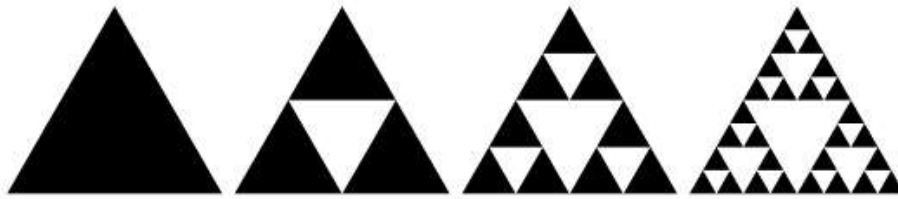


FIGURE 3.2: Sierpinski triangle construction process

### 3.1.2 The Sierpinski Triangle

Also called the Sierpinski gasket or the Sierpinski sieve, the Sierpinski triangle is a fractal and attractive fixed set with the overall shape of an equilateral triangle, subdivided recursively into smaller equilateral triangles [71]. Sierpinski's triangle is highly cited when the aim is to provide an example of self-similar sets. Its construction is illustrated in Figure 3.2 and described in Algorithm 1. Observe the initiator which is the triangle itself and the generator, the half of the side of the triangle.

---

#### Algorithm 1 Sierpinski's Triangle Construction

---

- 1: **procedure** SIERPINSKI
  - 2:     Start with an equilateral triangle.
  - 3:     Subdivide it into four smaller congruent equilateral triangles and remove the central triangle.
  - 4:     Repeat step 2 and step 3 with each of the remaining smaller triangles forever.
- 

For integer number of dimensions  $d$ , when doubling a side of an object,  $2^d$  copies of it are created. Let us look at Figure 3.2. For the Sierpinski triangle, doubling its side creates 3 copies of itself. Therefore, according to Definition 3.2, the Sierpinski triangle has fractal dimension  $\log(3)/\log(2) = \log_2 3 = 1.585$ , which follows from solving  $2^d = 3$  for  $d$ .

The area of a Sierpinski triangle is zero (in Lebesgue measure). The area remaining after each iteration is clearly  $3/4$  of the area from the previous iteration, and an infinite number of iterations results in zero. Note that Sierpinski triangle each has topological dimension 1, which is in line with Definition 3.3.

### 3.2 Self-Similarity of Human Society Geometry. Self-Similarity of Wireless Networks

From rapid prototyping to tissue-engineering, fractals have been extensively used in biology and medicine. In fact, as nature is seen as having a fractal “nature”, it is easy to understand why fractals have been used from the modeling of the universe to the modeling of the behavior of atoms. One may argue that the universe itself is fractal as a whole, the debate on this topic having led to the birth of fractal cosmology [72].

Cities yield some of the best examples of fractals (see Figure 3.3) as we shall further argue throughout this section.



FIGURE 3.3: Paris view from space at night. Courtesy of NASA/ESA

From Plato onwards, there has been an effort into demonstrating cities as examples of Euclidean geometry and proofs of the man’s power over nature. This has led to the separation of art from science as if the human society development is purely artificial. However this simplistic point of view has always been contradicted to some extent and more strongly in the last 50 years. When it has been realized that the physical form of cities is generated by social and economic constraint, the idea that the organically growth of cities is optimal has received more credibility. The view about the shape and form of cities has become that their irregularity and messiness is simply a superficial manifestation of a deeper order. In his remarkable work, [1, 2], Michael Batty argues that “cities are fractal in form” and that much of the pre-existing urban theory is a theory of the fractal city.

As the organization of economic activities in cities displays self-similarity properties, it comes as a natural consequence that urban road networks, as location of human activities, inherits self-similarity. This has been shown in [73]. Furthermore, it is immediate to notice that vehicular traffic inherits the same self-similarity. The self-similarity of urban traffic in time has been proven by data fitting in [74, 75]. These works support the adequacy of self-similar processes in modeling the vehicular traffic time series over various time scales. Furthermore, [76] shows that the requests for cars in platforms such as Uber display a self-similar pattern.

Passing now to networks, one does not lack references to the self-similarity of traffic in networks [77, 78]. In [79], the authors use self-similarity to simulate the network traffic and in [80] the authors show that the traffic in Ethernet is self-similar. [81] proposes a multi-fractal model for high-speed networks and the authors of [82] propose self-similarity for the simulation of IP traffic. In which regards wireless networks, fractal geometry has not been exploited extensively. In [83], the authors use the properties of fractals in order to miniaturize an antenna. Yet the subject where the self-similarity has been used the most intensively in the area of wireless networks is for the modeling of the coverage and coverage border [84, 85]. In [86], the authors claim that the placement of base-station is self-similar, which seems rather intuitive as the base-stations, themselves, follow social agglomerations where the cellular traffic is more intense.

A pioneering work has been done by using Poisson shots on Cantor maps for representing sensor networks. This model is, in fact, the precursor of the hyperfractal model and will further be debated in more details due to the importance it for the topic of this thesis.

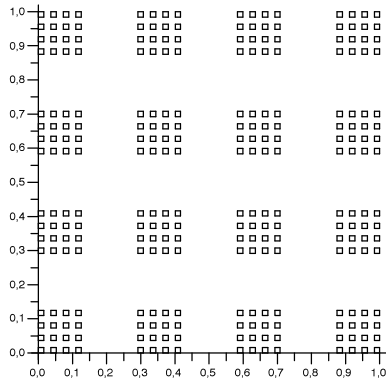
### **3.3 Poisson-Shots on Fractal Maps as Precursors of the Hyperfractal Model**

The precursor model of the hyperfractal model is the model called Poisson shots on fractal maps, and more precisely, the Poisson shots on Cantor maps. This model was generated by the motivation to model a network of transmitters and receivers in a setup that resembles the Virtual Multiple-Input-Single-Output (Virtual-MISO) communication scenario yet other communication scenarios can be envisaged.

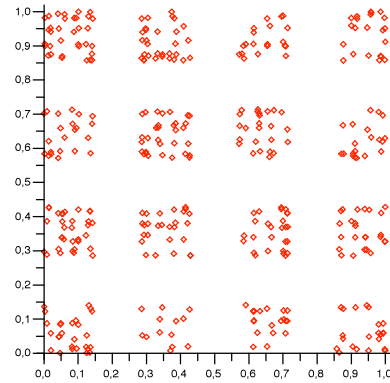
We shall briefly remind this model that was developed in [87] due to the importance it had in the process of generation of the hyperfractal model.

### 3.3.1 Definition of Poisson-shots on Fractal Maps

The Cantor maps are the support of the population of transmitters and receivers in the following model from [88]. The sensor networks inherit the property of self-similarity from the Cantor map. As the communication scenario is not relevant in this part of the manuscript, we shall not elaborate on this but only focus on the mathematical model that served as inspiration for the main contribution of this thesis.



(A) The network support

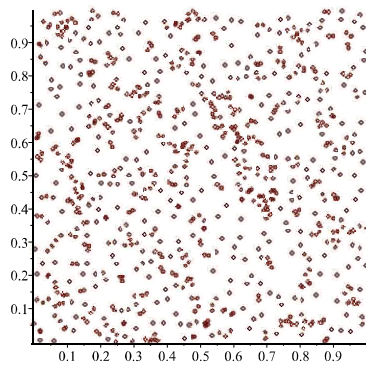
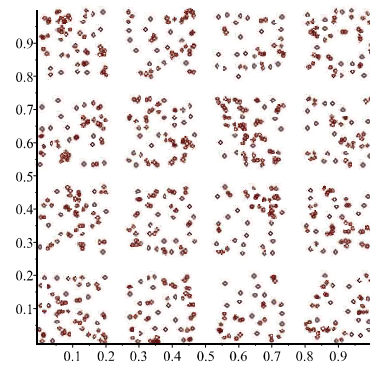
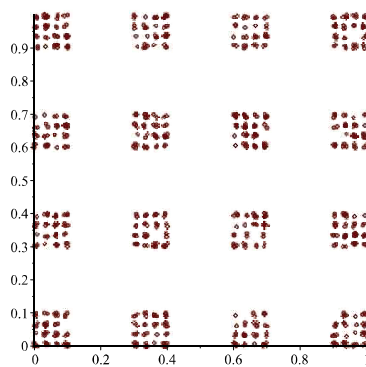
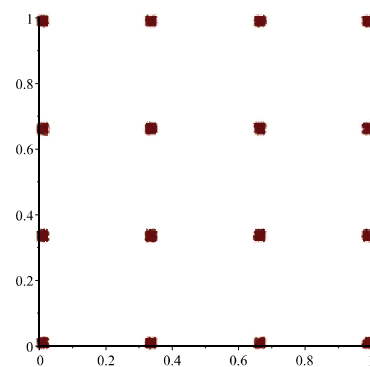
(B) Poisson shot on  $\mathcal{K}^2(1/8, 4)$ .

Let us first define the binary Cantor map and more generally the  $\ell$ -ary Cantor map, where  $\ell \geq 2$  is an integer. The reader is referred to [87, 88] for a more complete and detailed presentation.

**Definition 3.4** ( $\ell$ -ary Cantor maps). Let  $\ell \geq 2$  be an integer and  $0 \leq a \leq 1/\ell$ . The  $\ell$ -Cantor finite map is the fractal set  $\mathcal{K}(a, \ell)$  that satisfies  $\mathcal{K}(a, \ell) = \cap_{k \geq 0} \mathcal{K}_k(a, \ell)$  and  $\mathcal{K}_0(a, \ell) = [0, 1]$  and  $\mathcal{K}_{k+1}(a, \ell) = \bigcup_{j=0}^{\ell-1} (j(a+b) + a\mathcal{K}_k(a, \ell))$  with  $a+b = (1-a)/(\ell-1)$ . The infinite  $\ell$ -Cantor map  $\mathcal{K}^*(a, \ell)$  satisfies  $\mathcal{K}^*(a, \ell) = \cup_{k \geq 0} a^{-k} \mathcal{K}(a, \ell)$ . The fractal dimension is  $d_F = -\frac{\log \ell}{\log a}$ .

One can observe that the finite Cantor map is contained in the interval  $[0, 1]$ . The fractal dimension is obtained by observing that reducing distance by factor  $a$  gives exactly the  $\ell$ th part of the set:  $a^{d_F} = 1/\ell$ . The fractal dimension of  $\mathcal{K}(a, \ell)^2$  embedded in  $(\mathbb{R}^+)^2$  is  $-2\frac{\log \ell}{\log a}$ . Notice how the method used for determining the fractal dimension is similar to the method used for finding the fractal dimension of Sierpinski's triangle and following Definition 3.2.

**Definition 3.5** (The infinite Cantor map). The infinite Cantor map is the fractal set  $\mathcal{K}^*(a)$  on  $\mathbb{R}^+$  that satisfies  $\mathcal{K}^*(a, \ell) = \cup_{k \geq 0} a^{-k} \mathcal{K}(a, \ell)$ ,

(A)  $l = 4, a = 0.25$ .(B)  $l = 4, a = 0.2$ (C)  $l = 4, a = 0.1$ .(D)  $l = 4, a = 0.02$ FIGURE 3.5: Variation of parameter  $a$ 

We notice that the infinite Cantor map spans in the whole  $\mathbb{R}^+$  and that  $\mathcal{K}(a) = \mathcal{K}^*(a) \cap [0, 1]$ .

As a demonstration of the previous definitions, Figure 3.4a presents the network support  $\mathcal{K}^2(1/8, 4)$  and Figure 3.5 presents a Poisson shot on the Cantor map  $\mathcal{K}^2(1/8, 4)$ . The population analyzed in our model is obtained as such a Poisson shot.

Furthermore, this representation of the Poisson shots on Cantor maps can be used to represent a Poisson point process and all the stages between a Poisson point process and a Poisson shot on a Cantor map. Figure 3.5 illustrates four topologies obtained for different values of  $a$  and  $l$ . Notice how for  $a = 0.25$  we obtain, in fact, a Poisson point process and with the decay of parameter  $a$ , a certain clustering appears and the fractal dimension becomes lower and lower.



### 3.3.2 Towards the Hyperfractal

One can notice that the locations of the Poisson shots on the Cantor map may represent location of IoT devices in rooms, or buildings, or blocks, or cities, etc, or other unit of organization that has a self-similar structure and can be represented through a Cantor set.

While working on the mobility estimation through means of stochastic geometry we observed the impact of urban environment on the trajectories of the UEs. Learning that the locations of the devices inside buildings have a fractal distribution by inheriting the properties of the environment, the question came very soon: **What about the devices in between the buildings, on the streets? Do the locations of these devices inherit the self-similarity of the environment?**

Given the Poisson shot on Cantor map model and the previous observation on the UEs trajectories through the city, it fast came to our mind the idea that we could model the distribution of population of UEs (cars, IoT devices, etc) on streets in a space that is complementary to the space occupied by the population in a Poisson shot in a Cantor map. More precisely, our intuition was to place the streets between the Cantor sets and make the street width negligible. The following section will give all the theoretical development of the model, together with the intuition behind it.

## 3.4 The Hyperfractal Model

As vehicular communications comprise vehicle-to-vehicle type of communications (V2V) and vehicle to infrastructure type of communications (V2I), we identify two actors in the communication scenario: the vehicle and the infrastructure device. As the location of vehicles and their number are very different from the locations and number of infrastructure elements, we design the hyperfractal model in two options, one dedicated to the vehicles that will be called **mobile nodes** from now on, and one for the adjacent infrastructure devices that will be called **relays** from this time on.

### 3.4.1 Propagation Model as Feature of the Topological Model. Urban Canyon Model

The main goal is to develop a model for communications of vehicles in urban settings. As cars move on the streets of the city, the consequences of the radio propagation in this environment cannot be overlooked for an accurate modeling. Buildings are made of concrete, glass and steel which generate a formidable obstacle for radio wave propagation. This is the so-called **canyon effect** (see Figure 3.6) that implies that the signal emitted by a mobile node propagates only on the axis where it stands on [89, 90] and cannot penetrate the barrier created by the building walls.

This effect is further exacerbated when deploying millimeter wave (mmWave) technology. Measurements for mmWave have shown that the buildings materials (tinted glass) are highly attenuative and very reflective [91]. Communication in millimeter wave is directive

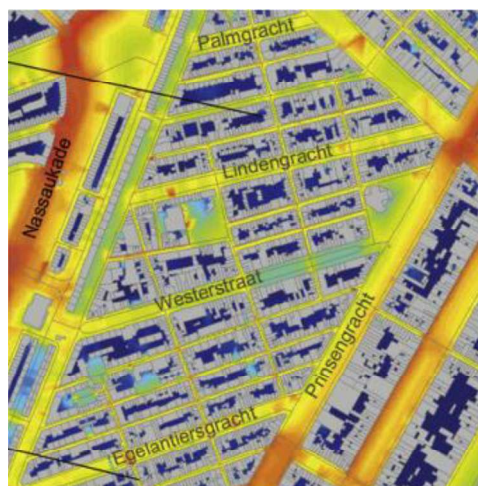


FIGURE 3.6: Signal strength heat map in a city. Canyon effect

and possible with good quality when vehicles are in line-of-sight [92, 93]. This features and the urban architecture characteristics lead to the existence of dead zones of coverage and decrease drastically the possibility of routing a packet through intersections. We therefore decide that the canyon effect is a fundamental characteristic of the communication scenarios addressed by the hyperfractal model and we include it in the design of the model, from the very beginning.

### 3.4.2 The Support

The map model lays in the unit square embedded in the 2-dimensional Euclidean space. The support of the population is a grid of streets. Let us denote this structure by  $\mathcal{X} = \bigcup_{l=0}^{\infty} \mathcal{X}_l$  with

$$\begin{aligned} \mathcal{X}_l := & \{(b2^{-(l+1)}, y), b = 1, 3, \dots, 2^{l+1} - 1, y \in [0, 1]\} \\ & \cup \{(x, b2^{-(l+1)}), b = 1, 3, \dots, 2^{l+1} - 1, x \in [0, 1]\}, \end{aligned}$$

where  $l$  denotes the level and  $l$  starts from 0, and  $b$  is an odd integer. Notice that  $\mathcal{X}$  is a dense subset. The construction of the first three levels,  $l = 0, 1, 2$ , is displayed in Figure 3.7. Observe that in the first stage, the “central cross”  $\mathcal{X}_0$  splits  $\mathcal{X} - \mathcal{X}_0$  in 4 “quadrants” which all are homothetic to  $\mathcal{X}$  with the scaling factor  $1/2$ .

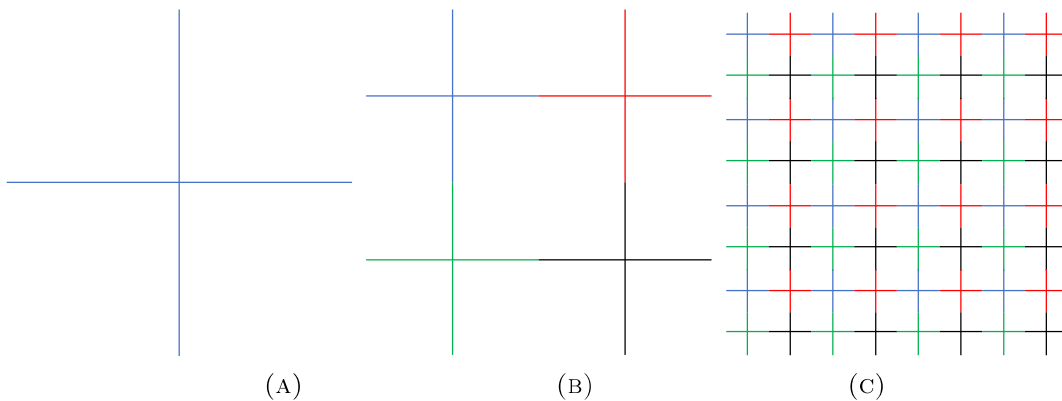


FIGURE 3.7: Hyperfractal support construction process

Observe that, similar to the Sierpinski’s triangle construction process, we obtain smaller and smaller “crosses”. The complete hyperfractal support is obtained, however, by summing the totality of the crosses obtained in all the stages. The number of stages goes to infinity. Figure 3.8 shows the complete support for three stages.

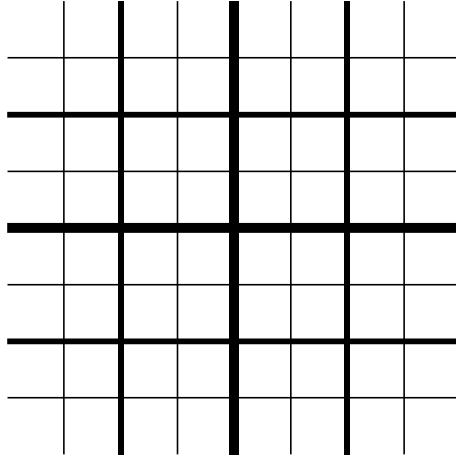


FIGURE 3.8

*Remark 3.6.* The 1-dimensional Lebesgue measure of  $\mathcal{X}$  is  $\infty$ . The 2-dimensional Lebesgue measure of  $\mathcal{X}$  is 0. The Lebesgue covering dimension of  $\mathcal{X}$  is 2, easily obtained by applying Minkowski–Bouligand dimension (box-counting dimension) [94].

We remind the reader that a fractal is a subset of  $\mathbb{R}^n$  that is self-similar and whose fractal dimension exceeds its Lebesgue covering dimension (also called topological dimension), as per Definition 3.3. The fact that the Lebesgue covering dimension of  $\mathcal{X}$  is 2 implies that its fractal dimension will be higher than 2.

### 3.4.3 The Hyperfractal Model for Mobile Users

The mobile users are represented with the Poisson point process  $\Phi$  on  $\mathcal{X}$ . The total intensity of process  $\Phi$ , or mean number of points is  $a$  with  $0 < a < \infty$ . The total number of available points is  $n$ .

The process  $\Phi$  is constructed in the following way:

- one samples the total number of mobiles users  $\Phi(\mathcal{X}) = n$  from Poisson( $a$ ) distribution;
- each mobile is placed independently with probability  $p$  on  $\mathcal{X}_0$  according to the uniform distribution;
- with probability  $(1 - p)/4$  it is recursively located in the similar way in one the four quadrants of  $\bigcup_{l=1}^{\infty} \mathcal{X}_l$ ;
- for each of the obtained quadrants, the previous two steps are repeated;

Figure 3.9 shows a hyperfractal with  $n = 1200$  nodes obtained following the described procedure.

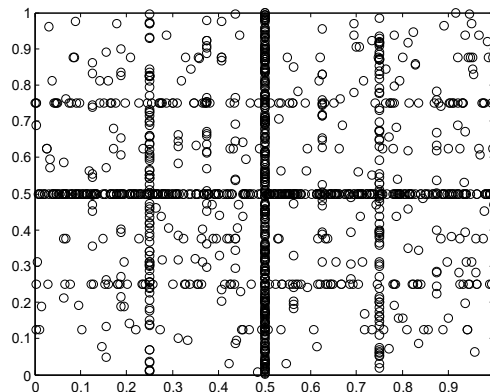


FIGURE 3.9: Hyperfractal with  $n = 1,200$  mobile nodes,  $d_F = 3$

The process  $\Phi$  has 1-dimensional intensity:

$$\lambda_l = (p/2)(q/2)^l a \quad (3.1)$$

on  $\mathcal{X}_l$ ,  $l = 0, \dots, \infty$ , with  $q = 1 - p$  for some parameter  $p$  ( $0 \leq p \leq 1$ ).

Following the construction procedure it is easy to observe that the process  $\Phi$  is neither stationary nor isotropic.

However, the process has the following self-similarity property: **the intensity measure of  $\Phi$  on  $\mathcal{X}$  is reproduced in each of the four quadrants of  $\bigcup_{l=1}^{\infty} \mathcal{X}_l$  with the scaling of its support by the factor  $1/2$  and of its value by  $q/4$ .** Therefore the measure has a structure which recalls the structure of a fractal set, such as the Cantor map [4]. One can define the fractal dimension of this measure.

*Remark 3.7.* The fractal dimension  $d_F$  of the intensity measure of  $\Phi$  satisfies

$$\left(\frac{1}{2}\right)^{d_F} = \frac{q}{4} \quad \text{thus} \quad d_F = \frac{\log(\frac{4}{q})}{\log 2} \geq 2.$$

The fractal dimension  $d_F$  defined above is greater than 2, the Euclidean dimension of the square in which it is embedded, thus we named the model *hyperfractal*, for the first time in [95]. Also, the fractal dimension is higher than the Lebesgue covering dimension of the support  $\mathcal{X}$ , verifying Definition 3.3. Notice that the hyperfractal is not a subset, like fractals are. The self-similarity is generated by the support  $\mathcal{X}$  plus the measure defined on the support.

When  $p = 1$  the model reduces to the Poisson process on the central cross while for  $p \rightarrow 0$ ,  $d_F \rightarrow 2$  it corresponds to the uniform measure in the unit square.

### 3.4.4 Hyperfractal Model for Relays

It is expected that the road-side units for vehicular communications will be installed on traffic light poles and traffic cameras. Not surprisingly, these elements also display self-similar behavior as their placement is dependent of the traffic density. Hence we apply another hyperfractal process for selecting the intersections where a road-side relay is installed or the existing traffic light is used as road-side unit.

We denote the relay process by  $\Xi$ . In order to facilitate the definition of process  $\Xi$ , we shall make use of an auxiliary Poisson process  $\Phi^r$ . Both process  $\Xi$  and  $\Phi^r$  have as support the 0-dimensional subset of  $\mathcal{X}$  made of the intersections of segments constituting  $\mathcal{X}$ .

Starting from a total budget of points  $M$ , the process  $\Phi^r$  is constructed as following:

---

**Algorithm 2** Construction of  $\Phi^r$

---

- 1: **procedure** PLACEMENT( $M, \pi$ )  $i=1$ ;
  - 2:     **repeat**
  - 3:         one samples the total number of relays  $\Phi^r(\mathcal{X}) = M$
  - 4:         with probability  $\pi^2$ , the placement is on the central crossing  $\mathcal{X}$ ;
  - 5:         with probability  $\pi \left(\frac{1-\pi}{2}\right)$ , the relay is placed in one of the four street segments of level  $\mathcal{X}_0$  starting at this point: North, South, West or East;
  - 6:         the process continues on the segment with the in-segment process;
  - 7:         with probability  $\left(\frac{1-\pi}{2}\right)^2$ , the relay is placed in one of the four quadrants delimited by the central cross and the in-quadrant process continues recursively;
  - 8:          $i = i + 1$ ;
  - 9:     **until**  $i > M$
- 

Following the placement process,  $\Phi^r$  has discrete intensity

$$p(h, v) = \rho\pi^2 \left(\frac{1-\pi}{2}\right)^{h+v} \quad (3.2)$$

on all intersections  $\mathcal{X}_h \cap \mathcal{X}_v$  for  $h, v = 0, \dots, \infty$  for some parameter  $\pi$ ,  $0 \leq \pi \leq 1$  and  $\rho > 0$ . That is, on any such intersection the mass of  $\Phi^r$  is a Poisson random variable with parameter  $p(h, v)$  and  $\rho$  is the total expected number of points of  $\Phi^r$  in the model. The expression in equation (3.2) comes straight-over after the construction process. This process be detailed in an intuitive manner in the following.

The self-similar structure of  $\Phi^r$  is well explained by its construction in which we first sample the total number of points from a Poisson distribution of intensity  $\rho$  and given  $\Phi^r(\mathcal{X}) = M$ , each point is independently placed.

Note the Poisson process  $\Phi^r$  is not simple since an intersection can carry several points.

Let us go back now to our main interest, the process for relays,  $\Xi$ . After defining process  $\Phi^r$ , the process  $\Xi$  is very easily defined.

**Definition 3.8.**  $\Xi$  is the support measure of process  $\Phi^r$ .

In other words, only one relay is installed in every crossing where  $\Phi^r$  has at least one point.

The construction of process  $\Xi$  is further illustrated in an intuitive way in Figure 3.10.

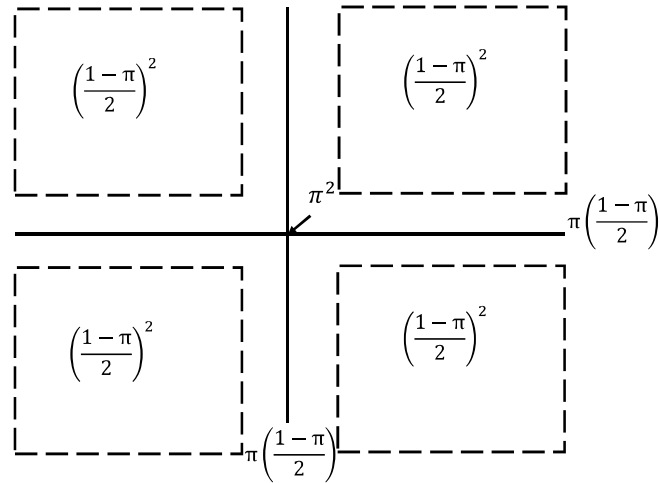


FIGURE 3.10: Relays process construction

*Remark 3.9.* Note that the relays form a non-homogeneous binomial point process (i.e. points are placed independently) on the crossings of  $\mathcal{X}$  with a given intersection of two segments from  $\mathcal{X}_u$  and  $\mathcal{X}_v$  occupied by a relay point with probability  $1 - \exp(-\rho p(h, v))$ .

Similarly to the process of users, we can define the fractal dimension of the relay process.

*Remark 3.10.* The fractal dimension  $d_r$  of the probability density of  $\Xi$  is equal to the fractal dimension of the intensity measure of the Poisson process  $\Phi^r$  and verifies

$$d_r = 2 \frac{\log(2/(1-\pi))}{\log 2}. \quad (3.3)$$

It can be assumed that  $\Phi$  and  $\Phi^r$  (and consequently  $\Xi$ ) are independent, but we do not need this assumption throughout the following derivations in this chapter. The assumption of independence, will be, however, used in the following chapters. A complete hyperfractal map with mobile nodes and relays is illustrated in Figure 3.11.

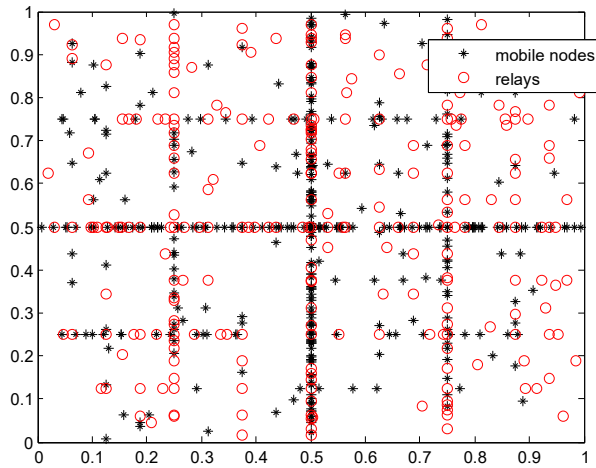


FIGURE 3.11: Complete hyperfractal map with mobiles and relays



### 3.5 Stochastic Geometry of the Hyperfractal Model

In this section we formally define and prove some basic properties regarding the typical user and the typical relay in the hyperfractal model described in the previous section. Some stochastic geometry tools are also provided in order to facilitate the future usage of the model by the research community.

As we mentioned in the previous chapter, the typical point of a stationary point process is one of the most important notions considered in stochastic geometry. The typical point is on the ground of Palm theory [96], having the Campbell-Mecke formula as the central property. We remind the reader (and refer to previous chapter) that in random graph theory, the root of an infinite unimodular rooted graphs is considered as its typical node, with the mass transport principle as the central property. Both approaches seek at generalizing the notion of the typical node as the one uniformly sampled from the whole population. It is straightforward to observe that this does not make sense for infinite populations.

Point processes  $\Phi$ ,  $\Phi^r$  and  $\Xi$  defined in the previous section are *not* stationary but are almost surely finite. Given this property, their respective typical points can be simply defined as the points uniformly sampled from the whole realization, given it is non-null. This approach, combined with the self-similar properties of the considered hyperfractal model lead to some interesting and useful observations that we present in this chapter.

In fact, as it will be shown in the following section, it is customary to define the typical points of the above processes in a more constructive way and prove the aforementioned uniform sampling properties among other results.

#### 3.5.1 Typical Points of $\Phi$ , $\Phi^r$ and $\Xi$

Let  $L + 1$  be an integer geometric random variable with parameter  $p$  (i.e.,  $\mathbb{P}(L = l) = p(1 - p)^{l-1}$ ) and given  $L$ , let  $x_0$  be the random location uniformly chosen on  $\mathcal{X}_L$ . We call  $x_0$  the *typical mobile user* of  $\Phi$ . More precisely, we shall consider point process  $\Phi \cup \{x_0\}$  where  $x_0$  is sampled as described above and independently of  $\Phi$ .

Similarly, let  $U + 1, V + 1$  be two independent geometric random variables with parameter  $\pi$  and given  $(U, V)$  let  $x_*$  be a crossing uniformly sampled from all the intersections of  $\mathcal{X}_U \cap \mathcal{X}_V$ . We call  $x_*$  the *typical auxiliary point* of  $\Phi^r$ . More precisely, we shall consider point process  $\Phi^r \cup \{x_*\}$  where  $x_*$  is sampled as described above and independently of  $\Phi^r$ .

The definition of the *typical relay node*  $\xi_0$  is less explicit and shall not be treated in this manuscript.

In what follows, we shall prove that our typical points support both the Campbell-Mecke formula and the Mass-Transport Principle therefore justifying our definition.

### 3.5.2 Fundamental Properties of the Typical Points

**Theorem 3.11** (Campbell-Mecke formula). *For all measurable functions  $f(x, \phi)$  where  $x \in \mathcal{X}$  and  $\phi$  is a realization of a point process on  $\mathcal{X}$ :*

$$\mathbf{E} \left[ \sum_{x_i \in \Phi} f(x_i, \Phi) \right] = a \mathbf{E} [f(x_0, \Phi \cup \{x_0\})] \quad (3.4)$$

$$\mathbf{E} \left[ \sum_{x_i \in \Phi^r} f(x_i, \Phi^r) \right] = \rho \mathbf{E} [f(x_*, \Phi^r \cup \{x_*\})] \quad (3.5)$$

*Proof of Theorem 3.11.* First, let us consider the process of users  $\Phi$ . We remind the reader that the process  $\Phi$  is non-stationary. By applying Campbell-Mecke formula and Slivnyak theorem [17] for the non-stationary Poisson point processes  $\Phi$ , we obtain:

$$\mathbf{E} \left[ \sum_{x_i \in \Phi} f(x_i, \Phi) \right] = \int_{\mathcal{X}} \mathbf{E} [f(x, \Phi \cup \{x\})] \mu(dx), \quad (3.6)$$

where  $\mu(dx)$  is the intensity measure of the process  $\Phi$ . Specifying this intensity measure in the right hand side term of (3.6), this becomes

$$\sum_{l=0}^{\infty} \int_{\mathcal{X}_l} \mathbf{E} [f(x, \Phi \cup \{x\})] a(1-p)^l p dx.$$

In the above expression one can recognize  $\mathbf{E} [f(x^0, \Phi \cup \{x_0\})]$  which concludes the proof of (3.4).

The proof of (3.5) follows exactly the same lines. □

**Theorem 3.12.** *The total expected number of relay nodes  $\mathbf{E} [\Xi(\mathcal{X})]$  admits the following representation*

$$\mathbf{E} [\Xi(\mathcal{X})] = \sum_{k=0}^{\infty} (k+1) 2^k \left( \frac{1-\pi}{2} \right)^{nk}. \quad (3.7)$$

*Proof.* By the definition of  $\Xi$ , one can express the left hand side of (??) in the following way:

$$\mathbf{E} \left[ \sum_{x_i \in \Xi} f(x_i, \Xi) \right] = \mathbf{E} \left[ \sum_{x_i \in \Phi^r} \frac{f(x_i, \text{supp}(\Phi))}{\Phi^r(\{x_i\})} \right],$$

where  $\text{supp}(\Phi)$  denotes the support of  $\Phi$ . Using (3.5), we thus obtain:

$$\mathbf{E} \left[ \sum_{x_i \in \Xi} f(x_i, \Xi) \right] = a \mathbf{E} \left[ \frac{f(x_*, \text{supp}(\Phi^r \cup \{x_*\}))}{1 + \Phi^r(\{x_*\})} \right]. \quad (3.8)$$

Which becomes:

$$\mathbf{E}[\Xi(\mathcal{X})] = a \mathbf{E} \left[ \frac{1}{1 + \Phi^r(\{x_*\})} \right].$$

In order to prove (3.7), observe that  $N_\pi := \Phi^r(\{x_*\})$  is a mixture of Poisson random variables and  $\mathbf{E} \left[ \frac{1}{1+N_\pi} \right]$  can be calculated.  $\square$

Let us validate numerically the finding in Theorem 3.11. We generate hyperfractal maps with several values of  $n$  and  $\rho_n = n$ ,  $d_F = 3$ . Let us remind that the theorem gives the expression of  $\mathbf{E}[\Xi(\mathcal{X})]$  as a sum with  $k \rightarrow \infty$ . In reality, a limited number of terms of the sums will suffice to approximate  $\mathbf{E}[\Xi(\mathcal{X})]$  with acceptable accuracy. We denote by  $k_{max}$  the number of terms used to compute the sum.

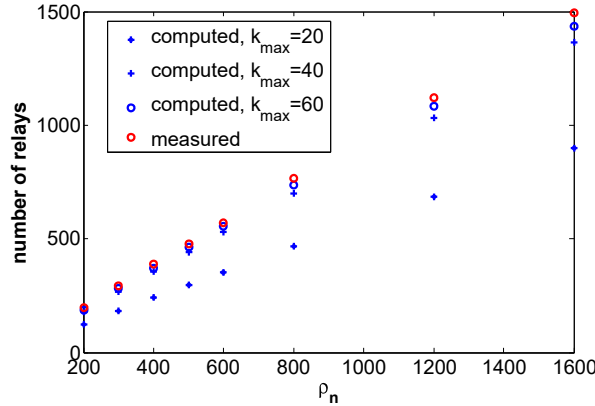


FIGURE 3.12: Measured versus computed number of relay in the map for several values of  $k_{max}$

Figure 3.12 shows that the computed values of number of relays approaches the measured value for  $k_{max} = 40$ . The precision is further enhanced when  $k_{max} = 60$ .

Now we shall state another fundamental property of the typical nodes equivalent to the Campbell-Mecke expression.

**Corollary 3.13** (The Mass Transport Principle (MTP)). *For all measurable functions  $f(x, y, \phi)$  of  $x, y \in \mathcal{X}$  and a realization of a point process on  $\mathcal{X}$ :*

$$\begin{aligned} & \mathbf{E} \left[ \sum_{x_i \in \Phi \cup \{x_0\}} f(x_0, x_i, \Phi \cup \{x_0\}) \right] \\ &= \mathbf{E} \left[ \sum_{x_i \in \Phi \cup \{x_0\}} f(x_i, x_0, \Phi \cup \{x_0\}) \right] \end{aligned}$$

and similarly for  $(x_*, \Phi^r)$  and  $(\xi_0, \Xi')$ .

*Remark 3.14.* The MTP allows us to easily prove that the typical node can be seen as uniformly sampled from the total population of nodes given this latter is not null.

*Remark 3.15.* The Mass Transport Principle is very useful in proving various conservation principles regarding the typical node. For example suppose all nodes transmit with equal transmission power 1, whatever the medium access control protocol employed. Denote by  $R = f(x, y, \Phi)$  the bit-rate available from  $x$  to  $y$ , for example  $R = f(x, y, \Phi) = \log(1 + SINR_{x \rightarrow y})$ . We define the following notions:

- total rate out from node  $x$ ,  $R_{x \rightarrow} := \sum_y R_{x \rightarrow y}$ .
- total rate to the node  $x$ ,  $R_{x \leftarrow} := \sum_y R_{y \rightarrow x}$ .

Under these assumptions and notations, making use of the MTP, the following result holds. The total expected rate into node  $x^0$  is equal to the total expected rate out from the node  $x^0$ :  $\mathbf{E}[R_{x_0 \rightarrow}] = \mathbf{E}[R_{x_0 \leftarrow}]$ .

### 3.5.3 An Alternative Method for Computing the Number of Relays in the Map

The previous section gave us the exact value of number of relays in the map by means of stochastic geometry. We shall now make an alternative computation of this quantity.

**Theorem 3.16.** *The average total number of relays in the map is:*

$$R(\rho) = O(\rho^{2/d_r} \log \rho) \tag{3.9}$$

*Proof.* The probability that a crossing of two lines of level  $H$  and  $V$  is selected to host a relay is  $1 - (1 - p(H, V))^M$ . When  $M$  is large, the probability is approximately  $1 - \exp(-Mp(H, V))$ .

The average number of relays on a streets of level  $H$  is denoted by  $L_H(\rho)$  and satisfies the identity:

$$L_H(\rho) = \sum_{V \geq 0} 2^V (1 - \exp(-p(H, V)\rho)).$$

We notice that  $L_H(\rho) = L_0((q'/2)^H \rho)$  and that  $L_0(\rho)$  satisfies the functional equation:

$$L_0(\rho) = 1 - \exp(-\pi^2 \rho) + 2L_0((q'/2)\rho).$$

It is known from [97],[98] that this classic equation has a solution such as  $L_0(\rho) = O(\rho^{2/d_r})$ .

The average total number of relays in the city is obtained as:

$$R(\rho) = \sum_{H, V \geq 0} 2^{H+V} (1 - \exp(-p(H, V)\rho))$$

and satisfies the functional equation

$$R(\rho) = 1 - \exp(-\pi^2 \rho) + 4L_0(p(q'/2)\rho) + 4R((q/2)^2 \rho).$$

From the same reference, [97], [98], one gets

$$R(\rho) = O(\rho^{2/d_r} \log \rho)$$

Since  $2/d_r < 1$  the number of relays is much smaller than  $\rho$ . □

Notice that the expression in Theorem 3.16 is less precise than the one in Theorem 3.11. Notice also that it is a closed formula which expresses the average total number of relays in the map as a function of the fractal dimension of the relay process.

## 3.6 Concluding Remarks

This section has provided the definition and properties of the main contribution of this thesis: the hyperfractal model. We first gave a brief overview of the fractal geometry and fractals, passing through the examples of usage of fractal geometry in the modeling of human society. In particular, we debated the modeling of urban environment and with its specific activities and we arrived to the modeling of wireless networks by means of fractal geometry. This chapter has not only given the intuition behind the choice of fractals for the proposed model but also presented the precursor of the hyperfractal model.

We have defined the hyperfractal model with its two options, the option for nodes and the option for relays, in a both theoretical and algorithmic manner. We have also presented tools that allow the manipulation of the model in the framework of stochastic geometry but also an example of alternative computation of metrics.

## Chapter 4

# Model Fitting with Traces. Computation of Fractal Dimension

A mandatory requirement when providing a novel model for the topology of wireless networks is to validate it with real data. An immediate requirement is to provide a procedure that allows transforming the data into the model. Usual procedures of data fitting for point process have been developed in the research community using diverse methods. For example, in the programming language called R, a commonly used language by the stochastic geometry community, the functions and libraries allow fitting the points to several types of processes: Poisson, Strauss, StraussHard, MultiStrauss, MultiStraussHard, Softcore, etc [99]. Unfortunately, existing procedures of data fitting cannot be used for the hyperfractal model as the interaction between points are different and cannot be recognized by existing software.

To validate the hyperfractal model and to prove its utility and ease of use, we developed a procedure of transforming traffic flow maps into hyperfractals, more precisely the computation of fractal dimension of the traffic flow maps. One can use such a procedure to compute the fractal dimension of a neighborhood, or of a city or a region and then, with the help of the derived expressions for the hyperfractals, compute metrics of interest. Example of such metrics are the broadcast time, the end-to-end delay and energy, etc as it will be shown in the following chapters.

## 4.1 Theoretical Foundation

Let us emphasize that in the definition of the hyperfractal model, we did not make assumptions or conditions on geometric properties such as shape. In order to preserve the self-similarity, the constraints are only on the density of population on streets and the length of streets. For example, a hyperfractal does not need that either the main/first level streets to be in a cross with a 90 degree angle or that there exist exactly two streets of level one that have the exact length. What is indeed necessary is the scaling between the length of different levels of the support  $\mathcal{X}_l$  and the scaling of the 1-dimensional intensity per level,  $\lambda_l$ , which are the only factors that generate the fractal characteristics of the model.

Taking into account these observations (that follow naturally from the construction process), we elaborated a procedure of computation of the fractal dimension of a traffic density map. The procedure can be adapted by adding three criteria to increase the precision of the fitting: namely, density-to-length, spatial intersection density, and time interval to intersection.

### 4.1.1 Density-to-Length Criteria and the Computation of the Fractal Dimension

This is the criteria used for computing the fractal dimension of the map. In a hyperfractal, the cumulated length of the street up to level  $H$  is  $2^{H+1} - 1$ . At this level,  $H$ , the density of the nodes on the streets is  $\frac{p}{2} \left(\frac{q}{2}\right)^H$ . We define as cumulated distance  $l_\Sigma$  as the sum of all streets of level  $H' < H$ . Let us define the density as a function of the cumulated distance  $l_\Sigma$ . It can be expressed as:

$$\lambda(l_\Sigma) = \Theta \left( l_\Sigma^{\log(q/2)/\log 2} \right)$$

Which can be further reduced to:

$$\lambda(l_\Sigma) = \Theta \left( l_\Sigma^{1-d_F} \right) \quad (4.1)$$

Notice that this is an expression that shows the decrease of the density of population with the increase of cumulated length by using the fractal dimension.

The **procedure for the computation of the fractal dimension** has the following five steps.



(i) The first step is the data collection, the length of streets and traffic statistics. For example, we used average annual traffic statistics, yet other kind of traffic statistics can be used, with different refinement and granularity.

(ii) Next, we consider a single street as an alignment of consecutive segments whose densities, from the less dense segment to the densest segment, do not vary more than by a factor  $f_A > 1$ . We consider the density of the street the average density of its segment. In a pure hyperfractal city model we have  $f_A = 1$ . This is quite similar to the standard concept of quantization.

(iii) The following step is to rank the streets in decreasing order of density:  $\lambda_1 \geq \lambda_2 \geq \dots \geq \lambda_i \geq \dots$ . Please be reminded that the building procedure of the hyperfractal acts similarly.

(iv) We compute the vector of cumulated sums of the segments of streets ordered by their decreasing density.

(v) We next plot the density of sorted streets versus cumulated length of sorted streets. In parallel, we plot the density repartition function with a starting value of  $d_F$  and by using the measure cumulated length and by curve fitting, determine the best approximation for  $d_F$ .

### 4.1.2 The Spatial Intersection Density Criterion

This provides the density statistics of the street intersections in the map. An accurate computation of the street intersection statistics is important for the validity of wireless metrics, as it will be shown in the following chapters.

For characterizing the street intersection statistics, we shall start by looking at the variation of the distance towards the intersection with a street whose density is in an interval  $[a, b]$ . More precisely we define  $L([a, b])$  as the largest distance from any point in any street of  $\mathcal{H}$  (resp.  $\mathcal{V}$ ) to an intersection with a street in  $\mathcal{V}$  (resp.  $\mathcal{H}$ ) whose density is in the interval  $[a, b]$ .

There should exist  $C_l > 1$  such that

$$L([\lambda, C_l \lambda]) = O\left(\lambda^{1/(d_F-1)}\right) \quad (4.2)$$

when  $\lambda$  decreases. In the pure hyperfractal model one must take  $C_l = 2/q$ , otherwise some value of  $\lambda$  would not correspond to any street density.

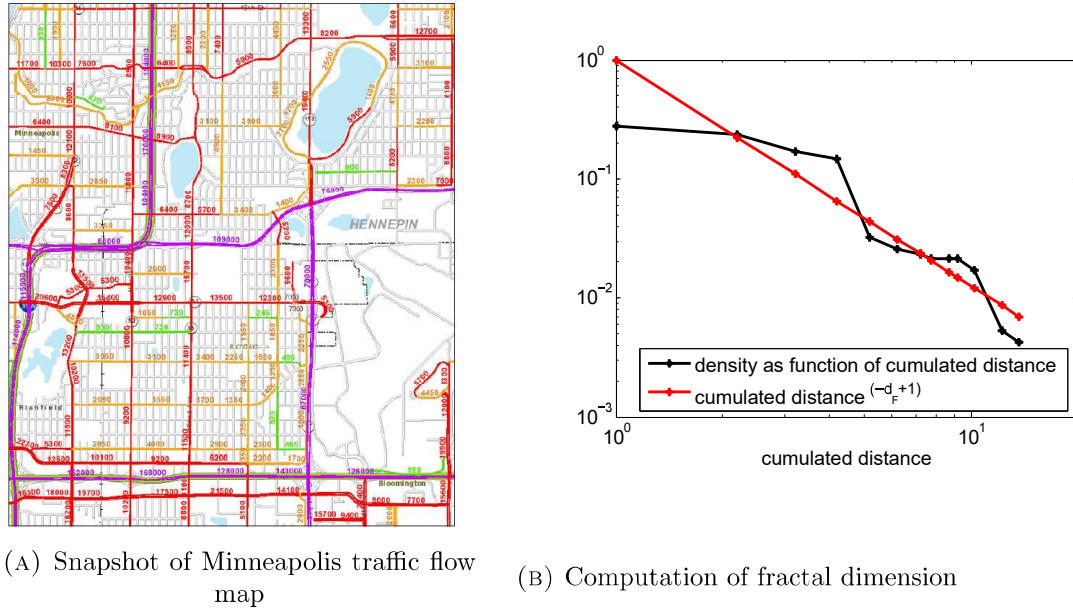


FIGURE 4.1: Procedure for Minneapolis

### 4.1.3 The Time Interval Intersection Criterion

This criteria can make the model fitting more precise when dealing with metrics where time is of crucial importance. It is relevant for particular wireless metrics, like broadcast, but not all others. More specifically, the criteria is necessary for the validation of Lemma 6.7 that gives the estimate of the packet turn time at an intersection.

The average time interval  $I(n_1, n_2)$  between two event crossing by mobile nodes at an intersection of two streets containing respectively  $n_1$  and  $n_2$  mobile nodes:

$$I(n_1, n_2) \leq \frac{S}{n_1 + n_2} \quad (4.3)$$

where  $S$  is a fixed parameter that relates to the average slowness of mobile nodes (defined informally as the average time to travel across one unit of distance). Formally, in our model,  $S = 1/v$ , when considering constant speed.

## 4.2 Data Fitting Examples

Finally, in order to illustrate how the hyperfractal model can be used for representing vehicles distribution on streets, we present here some data fitting results. Using public measurements ([100–103]), we show that the data validates the hyperfractal scaling of density and length of streets.

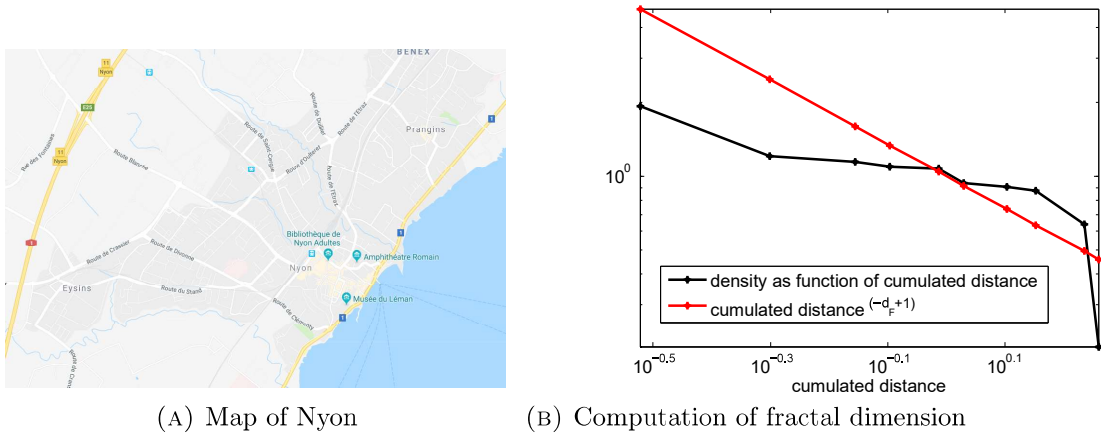


FIGURE 4.2: Procedure for Nyon

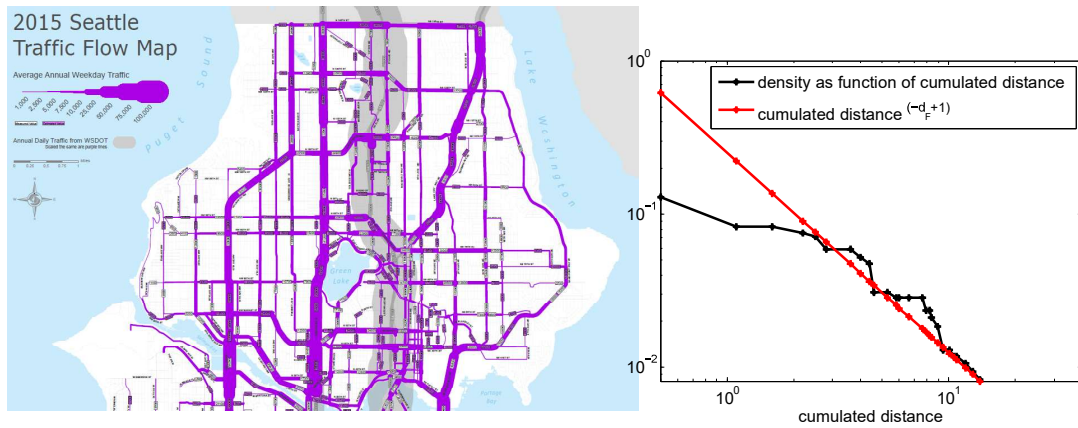
Figure 4.1a shows the snapshot of a traffic flow map displaying the average annual weekday traffic in a neighborhood of Minneapolis, in the United States. The most dense streets are represented in purple, the second densest streets are represented in red, then follow the yellow streets and at last the streets represented in green. Notice how the cumulated length of the purple streets is visibly lower than the cumulated length of the red streets. By applying the described fitting procedure and using equation (4.1), the estimated fractal dimension for Minneapolis is  $d_F = 2.9$ . In Figure 4.1b we demonstrate the fitting of the data for the density repartition function.

A second example of data fitting uses the measurements performed in the town of Nyon, in Switzerland (see Figure 4.2a). By making use of the density-to-length criteria, the fractal dimension is computed to be  $d_F = 2.3$  and the fitting is further displayed in Figure 4.2b.

Other two examples show the use of procedure for computing the fractal dimension of an area in Seattle, USA, (in Figure 4.3) and respectively Adelaide, Australia, (in Figure 4.4).

The computed value for Seattle is  $d_F = 2.3$  and for Adelaide  $d_F = 2.8$ .

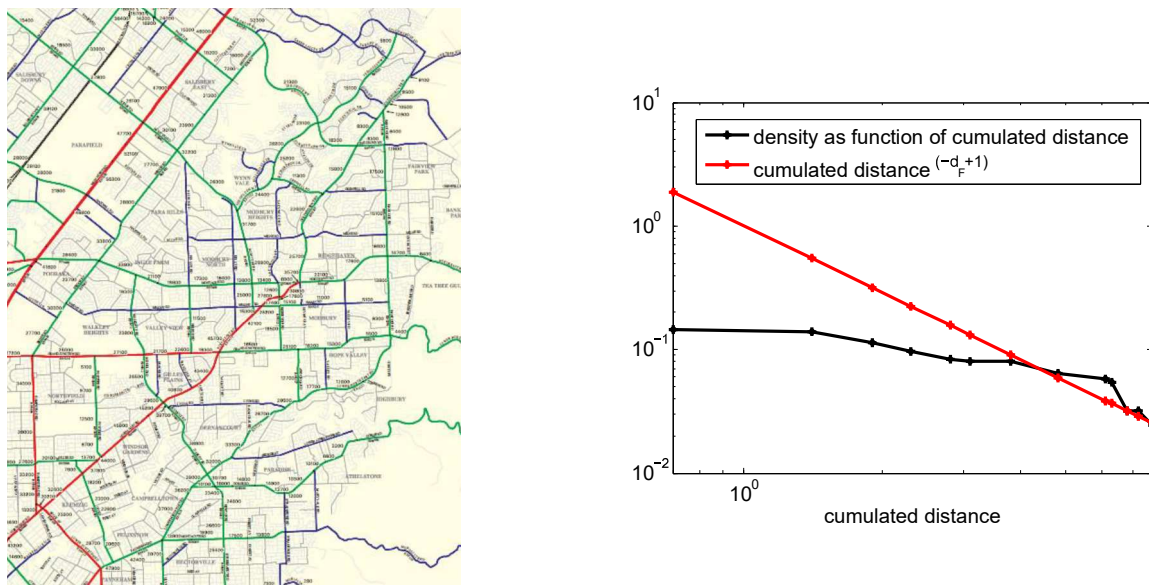
The fitting procedure presented here allows for the computation of the fractal dimension of the map according to the provided data. We do not suggest, however, that the annual average traffic flow is an ideal data set, as it does not capture variations such as day/night, rush hour/light traffic, and so on. An accurate modeling will need to adapt to the dynamics of the traffic measurements (and thus of the network), and the fractal dimension for each of these situations should be computed in each situation. In particular, the metrics of the network should be computed with the appropriate fractal dimension, depending on the situation analyzed (rush hour, night, etc).



(A) Snapshot of Seattle traffic flow map

(B) Computation of fractal dimension

FIGURE 4.3: Procedure for Seattle



(A) Annual Average Traffic Estimates in Adelaide

(B) Computation of fractal dimension

FIGURE 4.4: Procedure for Adelaide

At the moment of the writing of this manuscript, we did not develop yet a procedure for the computation of the fractal dimension of the relay process  $\Xi$ . Although we believe the procedure will be similar to the procedure of the computation of the fractal dimension of the process  $\Phi$ , the main issue in proceeding with the development of such a procedure is the lack of available datasets for validating the procedure. While the desirable dataset for validating such a procedure is a dataset of RSU (road side units), the lack of deployment of V2X infrastructure can delay this procedure for too long. That is why, we count, for future work, of validating a procedure of computation of the fractal dimension of the process of relays  $\Xi$  by using dataset of traffic lights.

Note that the same observations on the density decrease with the cumulated length increase are the key drivers for the generalization of the two processes,  $\Phi$  and  $\Xi$  to classic stochastic geometry models, as it will be described in a future chapter.

### 4.3 Concluding Remarks

This chapter has provided the procedure for computing the fractal dimension of a city/area/neighborhood with several criteria for several levels of accuracy. Such a procedure is mandatory when proposing a novel model for the topology of devices. The procedure has been presented in NOKIA 5G Campus Event.

Note that the our main intention is to provide a future user a procedure though which one can:

- take as an input the measurements of a traffic flow;
- transform into a hyperfractal with specific parameters ( $d_F$ ,  $n$ , etc);
- and easily compute metrics of interest.

The existence of such a method makes complete the methodology of usage of the hyperfractal model.

## Chapter 5

# Application to Ad-Hoc Networks. End-to-End Energy versus Delay

The hyperfractal models for nodes and relays, are very fit for the analysis of key performances of ad-hoc networks in urban environment. In the following, we shall show how, by modeling a vehicular network with road-side units by using hyperfractals, computations can be done in order to observe the trade-off between the end-to-end energy and delay. Secondary results on the bottleneck and network capacity under specific routing techniques are also provided. This further advocates for the usefulness of our models.

### 5.1 Introduction and Motivation

In the study of ad-hoc and, as a sub-class of ad-hoc, vehicular networks, topology arises frequently as a determinant factor in the computation of energy or end-to-end delay. Therefore, it is only natural to use the hyperfractal models for the analysis of such metrics.

Efficient communications for vehicular networks will be a vital part of the 5th generation of communication systems. Vehicular networking emerges as a key area of future communications networks with many innovation opportunities yet significant challenges. For instance, vehicular networks will continue to scale up to reach tremendous network sizes (with diverse hierarchical structures and node types), while vehicular interactions will become more complex. Automated and autonomous driving in such a complex environment requires more and more sensors that generate an increasing amount of data and require high bandwidth and data rates [104]. Millimeter wave technology (mmWave) can ensure this high data rates [105].

With many GHz of spectrum to offer, millimeter wave bands are increasingly attractive as one of the runners-up for enabling the 5th generation of wireless communications. While for a long time these frequencies have been disregarded for traditional cellular communications due to their large near-field loss and poor penetration (blocking) through concrete, water, foliage, and other common material, recent research and experiments have shown that communications are feasible in ranges of 150-200m dense urban scenarios with the use of such high gain directional antennas [106]. Furthermore, its tight requirements (e.g. line of sight, short range) are easily answered as the embedding space of vehicular networks leads to a highly directive topology (as much as it is possible, roads are built as straight lines) [107].

Given the numerous challenges of mmWave and the important place the vehicular communications hold in the new communications era, a realistic modeling of the topology for accurate estimation of network metrics and energy in particular is highly desirable.

The problem of energy optimization is critical for wireless nodes. A wireless transmission is done by electromagnetic waves that are generated by the antenna of the device when an electric field passes through it. Amongst other factors, the distance at which the wave will reach is influenced by the power of the electric field passing through the antenna. Yet there are numerous electromagnetic waves in concurrent transmissions and some of these waves will arrive at the receiver's antenna, therefore, for increasing the probability of recovering the transmitted message, the received signal strength has to overcome a specified threshold, which translates, again, in the increase of transmission power at the transmitter side.

Meanwhile, there are numerous regulations regarding the maximum allowed transmission power as it is harmful for humans and living beings (in particular in mmWave bands), the telecommunication industry is trying to limit the energy consumption due to the cost of electricity and the high environmental fingerprint (see for example one of the motivations of the Cloud-RAN technology [108]), and the number of wireless devices of small dimensions with a limited battery is exploding due to the massive IoT slice of 5G.

Sensors are particularly concerned about the energy consumption as they tend to use small batteries for energy supply that are in many instances non-replenishable. Significant attention has been given by the research community to this aspect. In [109] and [110], the authors develop a protocol based on opportunistic routing and asynchronous periods of activity in order to minimize the network energy consumption and end-to-end delay. More specifically, their work looks at sleep-wake periods. By considering an uncoordinated sleep mechanism, [111] provides a queuing analysis of the trade-offs between delay and energy.

On the other hand, the authors of [112] estimate the network lifetime (defined here as the time until the first node is drained of energy) and optimize it by exploiting the mobility of the sink. The network lifetime is also studied in [113] by considering clustering.

Considerable work has been done on the problem of energy efficiency for broadcast and multicast [114, 115]. In [116] the trade-offs between throughput and delay are computed when each user is allowed to send redundant packets along multiple paths towards its destination. A thorough analysis using queuing is provided. In [117], the authors propose an enhancement for opportunistic routing with the purpose to optimize energy consumption. In [118], the authors optimize relay placement in a sensor network such that constraints on connectivity, energy and performance are fulfilled.

In this chapter, we initiate the development of applications using the hyperfractal for the modeling of ad-hoc networks with the purpose of increasing the understanding of the hyperfractal model, demonstrate its capabilities and the tractability of expressions. For this, we study the achievable trade-off between the energy consumption and delay for end-to-end routing a piece of information between two nodes in a vehicular network with relays by exploiting the properties of the model, yet the study can be used for other scenarios of ad-hoc communications.

On one hand, our aim is to showcase the computation of key performance indicators (KPIs) in a end-to-end transmission in a hyperfractal setup. We advocate that computations of KPIs by exploiting the self-similarity and scaling properties of the hyperfractal model can provide tractable results with little complexity. On the other hand, we aim at exploring more fundamental properties of the hyperfractal like connectivity under specific constraints. Our studies have as secondary results observations on load and routing bottleneck.

## 5.2 System Model

The network topology model for this study will consider both the hyperfractal model for nodes,  $\Phi$ , which will represent positions of cars on streets and the hyperfractal model for relays,  $\Xi$ , which will represent the positions of road-side units, that assist in the vehicular networks. We are developing here a scenario that contains therefore both V2V (vehicle to vehicle) communications and V2X (vehicle to infrastructure).



As we primarily seek to understand the relationship between end-to-end communications and energy costs, we do not consider other detailed aspects of the communication protocol, such as the distributed aspects needed to gather position information and construct routing tables in every node. In fact, one can consider, in this case, that the source needs to know only the destination and the path towards the destination in terms of city map, not the specific sequence of nodes.

The considered routing strategy is the nearest neighbor routing strategy. The next hop is always the next neighbor on a street, i.e. there exists no other node between the transmitter and the receiver. Denote by  $d(i, j)$  the euclidean distance between nodes  $i$  and  $j$ ,  $r_{ij}$  represents the cost of directly transmitting a packet from node  $i$  to node  $j$ . Thus:

$$\begin{cases} r_{ij} = 1 & \text{if nodes } i \text{ and } j \text{ are aligned} \\ & \text{and } \nexists k \text{ such that } d(i, j) = d(i, k) + d(k, j) \\ r_{ij} = \infty & \text{otherwise} \end{cases}$$

The nearest neighbor routing strategy is a commonly routing strategy in stochastic geometry as it is a consequence of the interference model. It is a common fact that the signal strength of the nearest neighbor is the highest and the other neighbors resent more interference.

### 5.2.1 Preliminary Study on Connectivity with no Energy Constraints

A first study on the routing metrics in the hyperfractal model was performed under no constraints on transmission energy or radio range. Throughout this preliminary study it is assumed that each two nodes are connected if they belong to the same street, no matter the distance between the nodes. Following the construction process which assigns a relay in the central cross with high probability and given the assumption of connectivity that we make throughout this study, there will always be a connectivity competent around the relay with coordinates  $[\frac{1}{2}, \frac{1}{2}]$ . As we will be addressing the case when  $n \rightarrow \infty$ , we shall refer to this component as to the “giant component”.

A first result on the connectivity in the giant component under the assumptions described is given in the following.

**Definition 5.1.** Define by  $e(\rho)$  the fraction of mobile nodes outside the giant component. We further define by  $E(\rho, n)$  as the average number of mobile nodes outside the giant component,  $E(\rho, n) < ne(\rho)$ .

**Theorem 5.2.** *In a hyperfractal map with  $d_F$  the fractal dimension of the measure of nodes process  $\Phi$ ,  $d_r$  the fractal dimension of the measure of relays process  $\Xi$ ,  $n$  mobile nodes and  $\rho$  the Poisson variable generating the relay process, the fraction of mobile nodes in the giant component tends to 1 when  $\rho \rightarrow \infty$  and the average number of mobile nodes outside the giant component is  $O(n\rho^{-2(d_F-2)/d_r})$  when  $\rho \rightarrow \infty$ .*

**Remark:** For a configuration where  $d_F - 2 > d_r/2$ , the average number of mobile nodes outside the giant component tends to zero when  $\rho = O(n)$ .

Let us now give the proof of Theorem 5.2.

*Proof.* Let us first introduce the following notion.

**Definition 5.3.** Define as  $g(\rho)$  the cumulated density of nodes of process  $\Phi$  of lines connected to the central cross with a single relay.

We remind the reader that there is a set of vertical lines and a set of horizontal lines connected to the central cross with a single relay. The proof shall start by referring to a horizontal line, but it can be a vertical line in a similar way.

Given a horizontal line of level  $H$ , the probability that the line is connected to the vertical segment in the central cross is  $1 - e^{-\rho\pi^2(q/2)^H}$ . On each line of level  $H$  the density of mobiles is  $(p/2)(q/2)^H$ . The same reasoning is applied for the vertical line, therefore there are  $2^H$  of such lines intersecting each of the lines forming the central cross. One obtains  $g(\rho)$  as:

$$g(\rho) = 2 \sum_{H \geq 1} 2^H (p/2)(q/2)^H (1 - e^{-\rho\pi^2(q/2)^H}) \quad (5.1)$$

The quantity  $g(\rho)$  is a lower bound of the fraction of mobile nodes connected to the central cross as a line can be connected to the central cross via a sequence of relays, while above we consider the lines which are connected via a single relay. The fraction of nodes connected to the central nodes including those nodes in support of level 0,  $\mathcal{X}_0$  which are in density  $p$ . Therefore the quantity representing the fraction of nodes connecting to the central cross is lower bounded by the quantity  $p + g(\rho)$ .

The fraction of nodes outside the giant component is therefore the complementary of this quantity:

$$e(\rho) = 1 - p - g(\rho) = 2 \sum_{H \geq 1} 2^H \left(\frac{p}{2}\right) \left(\frac{q}{2}\right)^H e^{-\rho\pi^2(q/2)^H} \quad (5.2)$$

We shall now use a tool called the Mellin Transform [97]. This will be frequently used in the development of our results as it is a handy tool when working with harmonic sums that go to infinity.

The Mellin Transform  $e^*(s)$  of  $e(\rho)$  is :

$$e^*(s) = \int_0^\infty e(\rho)\rho^{s-1}d\rho = \Gamma(s)2 \sum_{H \geq 1} 2^H \left(\frac{p}{2}\right) \left(\frac{q}{2}\right)^H \left(\pi^2 \left(\frac{q'}{2}\right)^H\right)^{-s} = \frac{pq\left(\frac{\pi^2 q'}{2}\right)^{-s}}{1 - q\left(\frac{q'}{2}\right)^{-s}} \Gamma(s) \quad (5.3)$$

The Mellin transform is defined for positive residue,  $R(s) > 0$ , and has  $s$  a simple pole at  $s_0 = \frac{\log(1/q)}{\log(2/q')} = \frac{-2(d_F-2)}{d_r}$ .

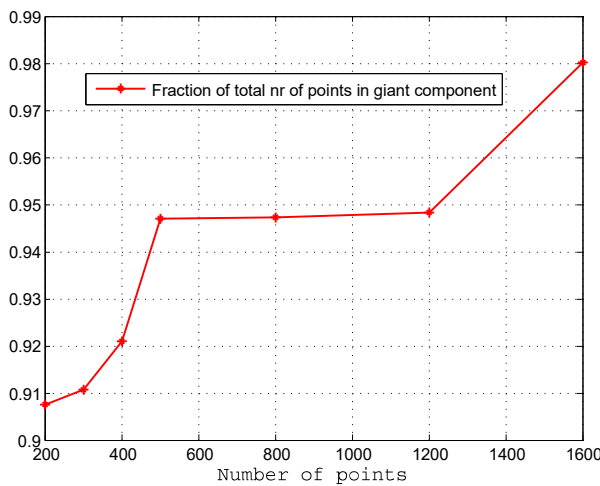
Using the inverse Mellin transform [97] we recover  $e(\rho)$  as:

$$e(\rho) = \frac{1}{2i\pi} \int_{c-i\infty}^{c+i\infty} e^*(s)\rho^{-s}ds$$

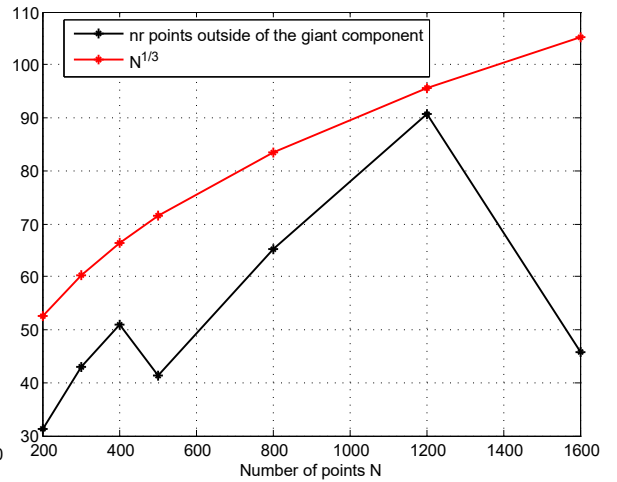
for any given number  $c$  within the definition domain of  $e^*(s)$  and obtain  $e(\rho) = O(\rho^{-s_0})$ .

We remind that both  $d_F$  and  $d_r$  are greater than 2 and so the theorem is proved. □

Let us validate Theorem 5.2 by numerical evaluation. The configuration studied is chosen as to validate the constraint,  $d_F - 2 > \frac{d_r}{2}$ ,  $d_F = d_r = 3$ ,  $n = \rho = 200, 300, 400, 500, 800, 1200$  and 1600 nodes.



(A) Fraction of points in the giant component



(B) Number of points outside the giant component

Figure 5.1a illustrates the variation of fraction of mobile nodes that are not included in the giant component. As claimed by Theorem 5.2, the fraction decreases with the increase of number of mobiles. Furthermore, the actual number of mobiles comprised in the giant component nodes follows the scaling law  $O(n^{\frac{1}{3}})$  as shown in Figure 5.1b .

### 5.3 Main Results

The previous preliminary results on connectivity were derived under no constraints on energy and radio range. As the energy consumption is an important KPI in ad-hoc networks, we initiate a comprehensive study with observations on the achievable end-to-end delay when constraints on transmission power are considered.

**Definition 5.4.** We define the **end-to-end transmission delay** as the total number of hops the packet takes in its path towards the destination.

We consider this as a good definition for the end-to-end delay as it is universal and not dependent on the access protocol. In fact, the results computed in such a manner, can be fitted to any of the access protocols (aloha, cdma, etc.). The transmission is done in a half-duplex way, a node is not allowed to transmit and receive during the same time-slot. The received signal is affected by additive white Gaussian noise (AWGN) noise  $N$  and path-loss with pathloss exponent  $\alpha > 2$  .

Denote by  $P_{max}$  the maximum allowed transmission power. It is assumed that all nodes on a street transmit with the same nominal power  $P_m$  which depends only on the number of nodes on the street as follows:

$$P_m = \frac{P_{max}}{m^\alpha}. \quad (5.4)$$

Usually, the received power is expressed as  $P_{received} = P_{max}/(distance^\alpha)$ , where  $P_{max}$  is the transmission power. In this case, we take the distance to be 1 when talking about nodes located on opposite ends of streets (normalized) therefore  $P_{received} = \frac{P_{max}}{1^\alpha}$ . When an extra node is located at the middle of the streets and we use the nearest neighbor routing technique,  $P_{received} = \frac{P_{max}}{(1/2)^\alpha}$ , when there is one more node  $P_{rec} = \frac{P_{max}}{(1/3)^\alpha}$  and so on. Therefore, on a street with  $m$  nodes, a good approximation is to suppose  $P_m = \frac{P_{max}}{m^\alpha}$ . The transmission power is often decided through some prior sensing, so this can be considered realistic.

An immediate consequence of this reasoning is that the cumulated energy to cover a whole street containing  $m$  nodes with uniform distribution via nearest neighbor routing is :

$$mP_m = P_{\max}/m^{\alpha-1} \quad (5.5)$$

Observe that, in this case, the larger the population of the street the smaller the nominal power and the smaller the energy to cover the street.

Relays stand in intersections, and thus on two streets with different values of  $m$ . Therefore, they will need to employ two different values for the transmission power. It is a common fact, for example for LTE devices, to have two different radio interfaces therefore we will make the same assumption for relays. The simulations will be done for the case with a single radio interface as well.

The giant component described previously is considered with no constraints on energy, in other words no constraint on the radio range. Here, given that the transmitting energy is dependent of the average density of the nodes on the streets and that the transmission energy per node is limited by the protocols to a value of  $P_{\max}$ , the connectivity is much more restricted and directly dependent on the constraints on energy.

We introduce the following notions and notations. Denote by  $t$  a node and by  $P(t)$  the nominal transmission power of this node.

**Definition 5.5.** Let  $\mathcal{T}$  be a sequence of nodes which constitutes a routing path. The path length is  $D(\mathcal{T}) = |\mathcal{T}|$ . The relevant “energy paths” are:

- The **path cumulated energy** is the quantity  $C(\mathcal{T}) = \sum_{t \in \mathcal{T}} P(t)$ , the sum of all nominal transmission energy of all nodes included in the path.
- The **path maximum energy** is the quantity  $M(\mathcal{T}) = \max_{t \in \mathcal{T}} P(t)$ , the maximum nominal energy used by a node in the specific routing path.

The path cumulated energy is of interest as we want to optimize the quantity of energy expended in the-end-to-end communication. This will lead to the minimization of the total energy spent by the network.

The path maximum energy is an important quantity to optimize as we want to find the path whose maximum energy does not exceed a given threshold depending on the energy sustainability of the nodes or the protocol. For instance, it is likely that no node can sustain a nominal power of  $P_{\max}$  which is the energy needed to transmit in a range corresponding to the entire length of a street. In this case it is necessary to find a path

which uses streets with enough (more) population in order to reduce the node nominal power to an acceptable value.

Now, as we have defined our constraints on the energy in a path, we can go back to the connectivity and define new connectivity components in concordance with the energy.

**Definition 5.6.**

- Let  $G(n, \mathbf{E})$  be the set of all nodes connected to the central cross with a path cumulated energy not exceeding  $\mathbf{E}$ .
- Let  $G_k(n, \mathbf{E})$  be the subset of  $G(n, \mathbf{E})$ , where the path to the central cross should not go through more than  $k$  fixed relays.

**Definition 5.7.** Let  $G'(n, \mathbf{E})$  and  $G'_k(n, \mathbf{E})$  the respective equivalents of  $G(n, \mathbf{E})$  and  $G_k(n, \mathbf{E})$  but with the consideration of the path maximum energy instead of cumulated energy.

### 5.3.1 Path Cumulated Energy

The following theorem shows the asymptotic connectivity properties of the hyperfractal in function of the cumulated energy and in function of the path maximum energy.

**Theorem 5.8.** *In a hyperfractal with  $n$  nodes. The following holds:*

$$\lim_{n \rightarrow \infty} \mathbb{E} \left\{ \frac{|G_1(n, n^{-\gamma} P_{\max})|}{n} \right\} = 1 \quad (5.6)$$

for  $\gamma < \alpha - 1$

and

$$\lim_{n \rightarrow \infty} \mathbb{E} \left\{ \frac{|G'_1(n, n^{-\gamma} P_{\max})|}{n} \right\} = 1 \quad (5.7)$$

for  $\gamma < \alpha$

where  $\alpha$  is the pathloss coefficient.

The theorem shows that the components  $G_1(n, n^{-\gamma} P_{\max})$ , the set of all nodes connected to the central cross through maximum one relay and with a path cumulated energy not exceeding  $n^{-\gamma} P_{\max}$ , and  $G'_1(n, n^{-\gamma} P_{\max})$ , the set of all nodes connected to the central cross through maximum one relay and with a path maximum energy not exceeding  $n^{-\gamma} P_{\max}$ , scale proportionally with the number of nodes  $n$  and tend to include all of the nodes when

$n \rightarrow \infty$ . Note that the constraint on energy, either cumulated either maximum per path,  $n^{-\gamma} P_{max}$  is approximatively  $n^{-1} P_{max}$  and the exponent of  $n$  is even lower than  $-1$ .

Before going for the proof of Theorem 5.8 let us introduce the following instrumental lemma that ensures the existence of nodes in a street.

**Lemma 5.9.** *There exists  $c_1 > 0$  such that, for all integers  $H$  and  $n$ , the probability that a street of level  $H$  contains less than  $n\lambda_H/2$  nodes or more than  $2n\lambda_H$  nodes is smaller than  $\exp(-c_1 n\lambda_H)$ .*

*Proof.* Let  $N_H(n)$  be the number of nodes contained in the street of level  $H$ .

Let  $z$  be a real number. By Chebyshev's inequality [119], we have:

$$\mathbb{E}[e^{zN_H(n)}] = (1 + (e^z - 1)\lambda_H)^n$$

In order to use Chebyshev's inequality, we change the “<” to “>”:

$$\begin{aligned} P\left(N_H(n) < \frac{n\lambda_H}{2}\right) &= P\left(e^{-zN_H(n)} > e^{zn\lambda_H/2}\right) \\ &\leq \frac{\mathbb{E}[e^{-zN_H(n)}]}{e^{-zn\lambda_H/2}} \end{aligned}$$

Therefore

$$\frac{\mathbb{E}[e^{-zN_H(n)}]}{e^{-zn\lambda_H/2}} = \exp\left(n\left(\log(1 + (e^{-z} - 1)\lambda_H) + z\lambda_H/2\right)\right).$$

For  $|z|$  bounded there exists  $c_2 > 0$  such that  $|e^z - 1| \leq c_2|z|$  and there exists  $c_3$  such that  $e^z - 1 \leq z + c_3z^2$ . For  $|x|$  bounded there exists  $c_4$  such that  $\log(1 + x) \leq x - c_4x^2$ . From these steps we obtain that, for sufficiently small  $|z|$ , one has:

$$\begin{aligned} \log(1 + (e^{-z} - 1)\lambda_H) + z\frac{\lambda_H}{2} &\leq -z\frac{\lambda_H}{2} + c_2\lambda_H z^2 - c_3\lambda_H^2 z^2 \\ &\leq -c_1\lambda_H. \end{aligned}$$

which settles that

$$\frac{\mathbb{E}[e^{-zN_H(n)}]}{e^{-zn\lambda_H/2}} \leq e^{-c_1 n\lambda_H}. \quad (5.8)$$

The proof of the second part of the lemma proceeds via the same reasoning, yet this time by using the inequality:

$$P(N_H(n) > 2n\lambda_H) \leq \frac{\mathbb{E}[e^{zN_H(n)}]}{e^{2zn\lambda_H}}. \quad (5.9)$$

□

The following corollary gives an observation on the scaling of the number of nodes in a segment of street with the cumulated energy, getting us one step closer to the results we are searching for.

**Corollary 5.10.** *Let  $0 < \phi \leq 1$ , assume an interval corresponding to a fraction  $\phi$  of the street length. If the interval is on a street of level  $H$ , the probability that it contains less than  $\phi\lambda_H n/2$  nodes and it is covered with a cumulated energy greater than  $\phi(n\lambda_H)^{1-\alpha} P_{\max}$  is smaller than  $e^{-c_1\phi\lambda_H n}$ .*

*Proof.* This is a slight variation of the previous proof.

Indeed if we denote by  $N_H(n, \phi)$  the number of nodes on the segment, we have  $\mathbb{E}[e^{tN_H(n, \phi)}] = (1 + \lambda_H \phi (e^z - 1))^n$ . Similarly, the previous proof applies by just replacing  $\lambda_H$  by  $\phi\lambda_H$ .

On this street, each node has the nominal power  $P_{\max}/N_H^\alpha(n)$ , therefore the cumulated energy of the segment containing  $N_H(n, \phi)$  has the expression  $P_{\max} \frac{N_H(n, \phi)}{N_H^\alpha(n)}$ .

By further applying the previous reasoning to each of the random variables  $N_H(n)$  and  $N_H(n, \phi)$ , we obtain the result.  $\square$

Throughout the rest of this chapter, we only consider the cases where  $d_F > 3$  as we need  $d_r < d_F - 1$ , i.e.  $(2/q)^2 < 2/q'$ .

The following theorem is the **main result** of this chapter and shows that increasing the path length decreases the cumulated energy. In fact, we shall see that for  $n \rightarrow \infty$ , the limiting energy goes to zero.

**Theorem 5.11.** *In a hyperfractal with  $n$  nodes, with  $d_F$  the fractal dimension of the process  $\Phi$  and  $d_r$  the fractal dimension of process  $\Xi$ , we consider an expression of the energy  $E_n$  as  $E_n = c_E n^{(1-\alpha)(1-c_5)} P_{\max}$  where  $c_E > 0$  and  $c_5 < 1$ . The number of hops,  $D_n$ , on the shortest path of cumulated energy less than  $E_n$  between two nodes belonging to the giant component  $G_1(n, E_n)$  is :*

$$D_n = O(n^{1-c_5/(d_F-1)}). \quad (5.10)$$

Note that, although the source and the destination belong to  $G_1(n, E_n)$ , it is not necessary that all the nodes constituting the path also belong to  $G_1(n, E_n)$ , i.e., the path may include nodes that are more than one hop from the central cross.



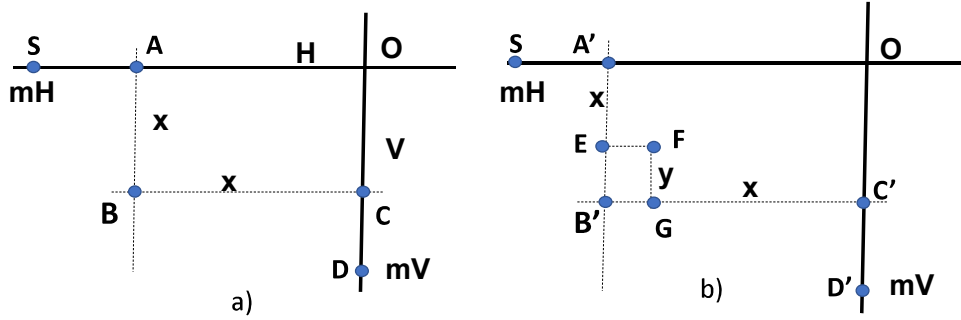


FIGURE 5.2: a) Diverted path with three fixed relays (left), b) five fixed relays (right).

*Remark 5.12.* We have the following identity:

$$\left( \frac{E_n}{P_{\max}} \right)^{1/(\alpha-1)} D_n^{d_F-1} = O(n^{d_F-2}).$$

*Proof.* The main part of our proof is to consider the simplified case when the source, denoted by  $m_H$ , and the destination,  $m_V$ , both stand on two different segments of the central cross. In this case, the energy constraint will be considered  $\frac{1}{3}E_n$ . The result can easily be extended to the case when the source and the destination stand anywhere in the giant component  $G_1(n, E_n)$  by taking  $E_n$  as energy constraint and the theorem then follows.

Let us look at Figure 5.2 a). Segment  $[SO]$  and  $[OD]$  belong to  $\mathcal{X}_0$  and the segments  $[AB]$ ,  $[BC]$  intersect  $\mathcal{X}_0$  and belong to  $\mathcal{X}_{x_1}$ ,  $\mathcal{X}_{x_2}$  with  $x_1, x_2 > 0$  and not necessarily  $x_1 \neq x_2$ .

When  $m_H$  and  $m_V$  are on located on  $\mathcal{X}_0$ , there exists a direct path which takes the direct route by staying on  $\mathcal{X}_0$ , more specifically, in Figure 5.2 a), the segments  $[SA]$ ,  $[AO]$ ,  $[OC]$ ,  $[CD]$ . Then, the path length is of order of  $\Theta(n)$  while the cumulated energy of order  $\Theta(n^{1-\alpha})P_{\max}$ .

In order to significantly reduce the order of magnitude of the path hop length, one must consider a diverted path with three fixed relays, as indicated in Figure 5.2 a). The three fixed relays we refer to are relays  $A$ ,  $B$  and  $C$ . The diverted path proceeds into two streets of  $\mathcal{X}_x$ . Let  $\mathcal{T}$  be the path. It is considered that  $x = c_5 \frac{\log n}{\log(2/q)}$  for  $c_5 < 1$ .

The path is made of two times two segments: the segment of street  $[SA]$  on  $\mathcal{X}_0$  which corresponds to the distance from the source to the first fixed relay to a street of  $\mathcal{X}_x$ , and then the segment  $[AB]$  between this relay and the fixed relay to the crossing a street of

$\mathcal{X}_x$ . The second part of the path is symmetric and corresponds to the connection between this relay and the destination through segment  $[BC]$  and  $[CD]$ .

Let us look at the more general scenario in Figure 5.2,b). Denote by  $L(x, y)$  the distance from an arbitrary position on a street of  $\mathcal{X}_y$  to the first fixed relay to a street of  $\mathcal{X}_x$ . The probability that a fixed relay exists at a crossing of two streets of respective  $\mathcal{X}_x$  and  $\mathcal{X}_y$  is  $1 - \exp(-\rho n p(x, y))$ . Since, by construction, the spacing between streets of  $\mathcal{X}_x$  is  $2^{-x}$ :

$$L(x, y) \leq \frac{2^{-x}}{1 - \exp(-\rho p(x, y))}$$

where  $\rho$  is the total expected number of points in  $\Phi^r$  in the map (reminding that the process of relays  $\Xi$  is the support of  $\Phi^r$  and  $\rho = n$  to simplify. The probability that the two streets of  $\mathcal{X}_x$  have a fixed relay at their crossing is  $1 - \exp(-\rho p(x, x))$ . With the condition  $\rho = n$ , one gets  $\rho p(x, x) = n^{1-2c_5} \log(2/q) / \log(2/q') > n^{1-c_5}$  since  $2 \log(2/q) < \log(2/q')$ . Therefore the probability that the relay does not exist decays exponentially fast.

Going back to the analyzed scenario in Figure 5.2,b) and using the reasoning of eq. (5.5) for segments of  $\mathcal{X}_0$  and  $\mathcal{X}_x$ , the cumulated energy of the path,  $E(\mathcal{T})$ , satisfies with high probability

$$E(\mathcal{T}) = O(L(x, 0)n^{1-\alpha}P_{\max}) + O((n\lambda_x)^{1-\alpha}P_{\max})$$

and the average number of nodes of the path,  $D(\mathcal{T})$ , satisfies with probability tending to 1, exponentially fast:

$$D(\mathcal{T}) = O(L(x, 0)n) + O(n\lambda_x).$$

It is quite easy to observe that the main contributors in the cumulated energy are the segments  $[AB]$  and  $[BC]$  since it is there that the spacing between consecutive nodes is more significant and therefore the nominal transmission power per node as well. Let us express this contribution by denoting  $x$  as  $x = c_5 \frac{\log n}{\log(2/q')}$ :

$$E(\mathcal{T}) = O\left(n^{(1-\alpha)(1-c_5)}\right).$$

Let  $c_E$  such that

$$E(\mathcal{T}) \leq \frac{c_E}{3} n^{(1-\alpha)(1-c_5)}.$$

The main contributor in hop count in the path is, in fact, the nodes of the path standing on  $\mathcal{X}_0$ , namely  $[SA]$  and  $[DC]$ :

$$D(\mathcal{T}) = O\left(n^{1-c_5/(d_F-1)}\right).$$

And so the proof is complete.  $\square$

In Theorem 5.11, it is always assumed that  $E_n \rightarrow 0$ , since  $c_5 < 1$ . In this case  $D_n$  spans from  $O(n^{1-1/(d_F-1)})$  to  $O(n)$  (corresponding to a path staying on the central cross). When the hyperfractal dimension  $d_F$  is large it does not make a large span. In fact, if  $E_n$  is assumed to be constant, *i.e.*  $c_5 = 1$ , then we can have a substantial reduction in number of hops, as described in the following theorem.

**Theorem 5.13.** *In a hyperfractal with  $n$  nodes, with  $d_F$  the fractal dimension of the process  $\Phi$  and  $d_r$  the fractal dimension of process  $\Xi$ , the shortest path of cumulated energy  $E_n = v_E P_{\max}$  with  $v_E > 6$ , between two nodes belonging to the giant component  $G_1(n, E_n)$ , passes through a number of hops :*

$$D_n = O\left(n^{1-\frac{2}{d_r(1+1/d_F)}}\right)$$

*Remark 5.14.* When  $d_r \rightarrow 2$  then  $D_n = O(n^{1/(d_F+1)})$ , and the hyperfractal model is behaving like a hypercube of dimension  $d_F + 1$ . Notice that, in this case,  $D_n$  tends to be  $O(1)$  when  $d_F \rightarrow \infty$ .

*Proof.* In the proof of Theorem 5.11, it is assumed that  $x < \frac{\log n}{\log(2/q)}$  in order to ensure that the number of hops on the route of  $\mathcal{X}_x$  tends to infinity. However the parameter  $x$  can be in the range  $\frac{\log n}{\log(2/q')} \leq x < \frac{\log n}{2 \log(2/q)}$ .

When  $n\lambda_x \rightarrow 0$ ,  $E(\mathcal{T}) \rightarrow 2P_{\max}$  since the streets of  $\mathcal{X}_x$  are empty of nodes with probability tending to 1. Let us denote  $x = c_6 \frac{\log n}{2 \log(2/q)}$  with  $c_6 < 1$ . We have  $D(\mathcal{T}) = O(L(x, 0)n) = O(n^{1-c_6/d_r})$ . Clearly  $c_6$  cannot be greater than 1 as, in this case, the two streets of  $\mathcal{X}_x$  will not hold a fixed relay with high probability and the packet will not turn at the intersection. Therefore the smallest order one can obtain on the diverted path with three relays is limited to  $n^{1-1/d_r}$ , which is not the claimed one.

To obtain the claimed order, one must use the more general, diverted path with five fixed relays, as shown in Figure 5.2 b). The diverted path is composed by the segments:  $[SA'], [A'E], [EF], [FG], [GC']$  and  $[C'D']$ . It is shown in [95] that the order can be decreased to  $n^{1-2/((1+1/d_F)d_r)}$ .  $\square$

### 5.3.2 Path Maximum Energy

The next results revisit the previous theorems on the path cumulated energy in the corresponding case of the imposed constraint on the path maximum energy.

**Theorem 5.15.** Let  $M_n = n^{-\alpha(1-c_5)} P_{\max}$  for  $c_5 < 1$ . The number of hops  $D_n$  on the shortest path of maximum energy less than  $M_n$  between two nodes belonging to the giant component  $G'_1(n, M_n)$  is:

$$D_n = O(n^{1-c_5/(d_F-1)})$$

*Remark 5.16.* It is important to note that although the orders of magnitude of path length  $D_n$  are the same in both Theorem 5.11 and Theorem 5.15, the results consider two different giant components: the giant component referring to the cumulated energy,  $G_1(n, E_n)$  versus the giant component referring to the maximum energy  $G'_1(n, M_n)$ .

*Remark 5.17.* The following identity hold:

$$(M_n/P_{\max})^{1/\alpha} D_n^{d_F-1} = O(n^{d_F-1-\alpha}). \quad (5.11)$$

**Theorem 5.18.** Let the maximum path energy between two points belonging to the giant component,  $G'_1(n, M_n)$  be  $M_n = P_{\max}$ . The number of hops  $D_n$  on the shortest path is  $O(n^{1-2/(d_r(1+1/d_F))})$ .

This theorem gives, in fact, the path length when no constraint on energy exists (or that the maximum energy allowed is the highest energy for a transmission between two neighbors in the hyperfractal map).

### 5.3.3 Remarks on the Network Throughput Capacity

Let us now briefly look at the scaling of the network throughput capacity when a constraint on the energy is imposed. In [120], the authors express the throughput capacity of ad-hoc wireless networks in a PPP setup as:

$$\zeta(n) = \Theta \left( \frac{n^2 \sum_{i \in G} \omega_i(n)}{\sum_{i,j \in G} r_{ij}} \right). \quad (5.12)$$

where  $\zeta(n)$  is the throughput capacity, defined as the expected number of packets delivered to their destinations per slot,  $\omega_i(n)$  is the expected transmission rate of each node  $i$  among all the nodes  $n$  and  $G$  is the giant component. In the following, denote by  $C$  the transmission rate of each node.

Using the result of Theorem 5.11 and Theorem 5.15 and substituting them in the expression 5.12, we obtain the following corollary on a lower bound of the network throughput capacity with constraints on path energy.

**Corollary 5.19.** *In a hyperfractal with  $n$  nodes, with  $d_F$  the fractal dimension of the process  $\Phi$  and  $d_r$  the fractal dimension of process  $\Xi$ ,  $c_5 < 1$  and  $C$  the transmission rate of each node, when:*

- $E_n = O(n^{(1-\alpha)(1-c_5)} P_{\max})$  is the maximum cumulated energy of the minimal path between any pair of nodes in the giant component  $G_1(n, E_n)$

or when

- $M_n = O(n^{-\alpha(1-c_5)} P_{\max})$  is the maximum path energy of the minimal path between any pair of nodes in the giant component  $G'_1(n, M_n)$ ,

a lower bound on the network throughput is:

$$\zeta(n) = \Omega\left(Cn^{\frac{c_5}{d_F-1}}\right) \quad (5.13)$$

*Remark 5.20.* We notice that with  $c_5 < 1$  and  $d_F > 3$  we have  $\zeta(n)$  of order which can be smaller than  $n^{1/2}$  which is less than the capacity in a random uniform network with no canyon effect as described by Gupta and Kumar in [29].

*Remark 5.21.* When  $c_5 = 1$ , i.e. with no energy constraint  $E_n = c_E P_{\max}$  the path length can drop down to  $D_n = O(n^{1-2/((1+1/d_F)d_r)})$  and, in this case, we have  $\zeta(n) = \Omega(n^{2/((1+1/d_F)d_r)})$  which tends to be in  $O(n)$  when  $d_F \rightarrow \infty$  and  $d_r \rightarrow 2$ . In this situation the capacity is of optimal order since  $D_n$  tends to be  $O(1)$ .

### 5.3.4 Simulations

This section presents an evaluation of the accuracy of our theoretical findings in different scenarios by comparing them to results obtained by simulating the events in a two-dimensional network. We use our own discrete time event-based simulator (developed in Matlab) which follows the model presented earlier.

The length of the map is set to 1000 and, therefore,  $P_{\max}$  is just  $1000^\alpha$ , where  $\alpha$  is the pathloss coefficient that is either 2, 3 or 4, as it will be mentioned throughout the section.

Let us look at Figure 5.3 to get a grasp of the trade-offs between cumulated end-to-end energy and hop count for a transmitter-receiver pair. The pair has been selected randomly from the simulations performed in a hyperfractal map with  $n = 800$ , pathloss coefficient  $\alpha = 4$ , fractal dimension of nodes  $d_F = 4.33$  and fractal dimension of relays  $d_r = 3$ .

The plot shows the minimum cumulated energy for the end-to-end transmission for a fixed and allowed number of hops,  $k$ , in red circle markers. Note that the energy does not decrease monotonically. This is due to the fact that forcing to take a longer path may not allow to take the best path. However when considering the minimum cumulated energy of all paths *up to a number of hops*, the black star markers in Figure 5.3, the energy decreases and exhibits clearly the behavior analyzed in Theorem 5.11. That is, the minimum cumulated energy is indeed decreasing when the number of hops is allowed to grow (and the end-to-end communication is allowed to choose longer, yet energetically cheaper, paths).

Let us further validate Theorem 5.11 through simulations performed for 100 randomly chosen transmitter-receiver pairs in hyperfractal maps with various configurations. We run simulations for different values of the number of nodes,  $n = 800$  nodes and 1000 nodes respectively, different values of pathloss,  $\alpha = 2$  and  $\alpha = 3$  (values characteristic of urban environment when the technology is mmWave) and different configurations of the hyperfractal map. The setups of the hyperfractal maps are: node fractal dimension  $d_F = 4.33$  and relay fractal dimension  $d_r = 3.3$  for the first setup and  $d_F = 3.3$  and  $d_r = 2.3$  for the second setup.

The results exhibited in Figures 5.4, 5.5, 5.6 and 5.7 are obtained by computing, for each of the transmitter-receiver pair, the minimum cumulated end-to-end energy for a path smaller than  $k$ , then averaging over the 100 results.

The left-hand sides of the Figures 5.4 and 5.5 show the variation of the minimum path cumulated energy with the increase of the number of hops in setup of  $d_F = 4.33$  and  $d_r = 3$  for  $n = 800$  in Figure 5.4 and  $n = 1000$  in Figure 5.5. The figures demonstrate that, indeed, allowing the hop count to grow decreases the energy considerably. The decay

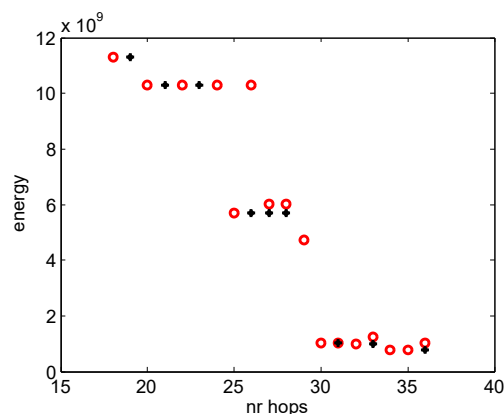


FIGURE 5.3: Minimum cumulated end-to-end energy versus hops for a transmitter-receiver pair.

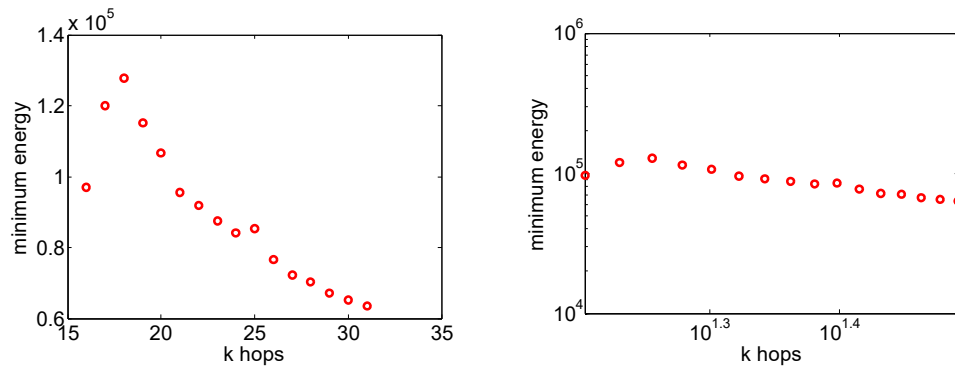


FIGURE 5.4: Minimum cumulated end-to-end energy versus hops, averaging over 100 transmitter-receiver pairs,  $d_F = 4.3$ ,  $d_r = 3.3$ ,  $n = 800$

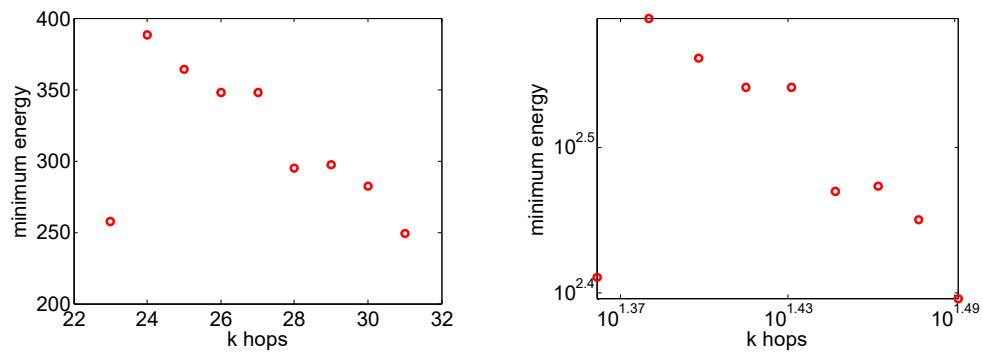


FIGURE 5.5: Minimum cumulated end-to-end energy versus hops, averaging over 100 transmitter-receiver pairs,  $d_F = 4.3$ ,  $d_r = 3.3$ ,  $n = 1000$

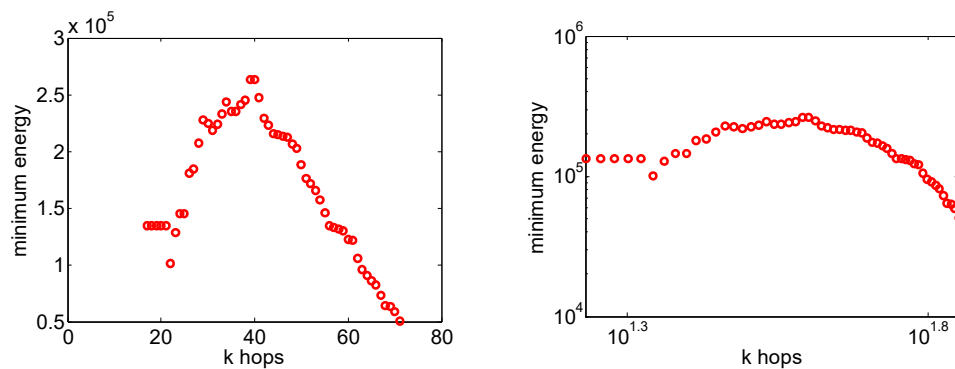


FIGURE 5.6: Minimum cumulated end-to-end energy versus hops, averaging over 100 transmitter-receiver pairs,  $d_F = 3.2$ ,  $d_r = 2.3$ ,  $n = 800$ , linear scale left, logarithmic scale right

of the maximum cumulated energy with the allowed number of hops is even more visible in logarithmic scale in the right side of the same figures.

The decays remains substantial when changing the setup to  $d_F = 3.2$ ,  $d_r = 2.3$ . Figures 5.6 and 5.7 shows the results obtained for  $n = 800$  and  $n = 1000$  respectively in the new setup. The decay is exhibited more clearly when looking in logarithmic scale. Even though there can be oscillations around the linearly decreasing characteristic, as one can notice in

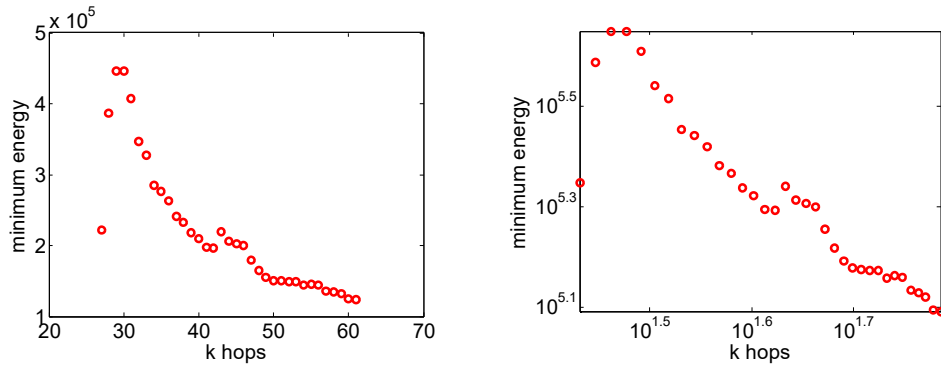


FIGURE 5.7: Minimum cumulated end-to-end energy versus hops, averaging over 100 transmitter-receiver pairs,  $\alpha = 2, d_F = 3.3, d_r = 2.3, n = 1000$ , linear scale left, logarithmic scale right

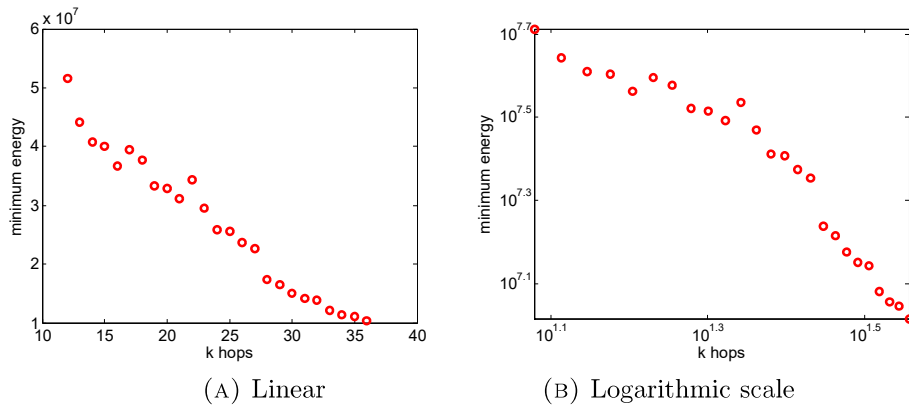


FIGURE 5.8: Minimum cumulated end-to-end energy versus hops, averaging over 100 transmitter-receiver pairs,  $\alpha = 3, d_F = 4.33, d_r = 3, n = 800$

Figure 5.7, left hand side, the global behavior stays the same, decreasing, as one can better notice in logarithmic scale in Figure 5.7, right hand side.

When changing the pathloss coefficient to  $\alpha = 3$ , the effect of Theorem 5.11 remains, as illustrated in Figure 5.8 for a hyperfractal setup of  $d_F = 4.33, d_r = 3, n = 800$  nodes.

Next, we validate the claims of Theorem 5.15 on the variation of path length with the imposed constraint on maximum energy per node. For that, we choose randomly 100 transmitter-receiver pairs belonging to the central cross and we compute the shortest path by applying a constraint on the maximum transmission energy of nodes belonging to the path. For the configurations chosen, the hyperfractal setups are: nodes fractal dimension  $d_F = 3.3$ , relays fractal dimension  $d_r = 2.3$ , pathloss coefficient  $\alpha = 3$  and we vary the number of nodes,  $n$  to be either  $n = 500$  or  $n = 800$ .

For both values of  $n$ , Figure 5.9a, shows that indeed, decreasing the constraint of path maximum energy leads to an increase in the path length.



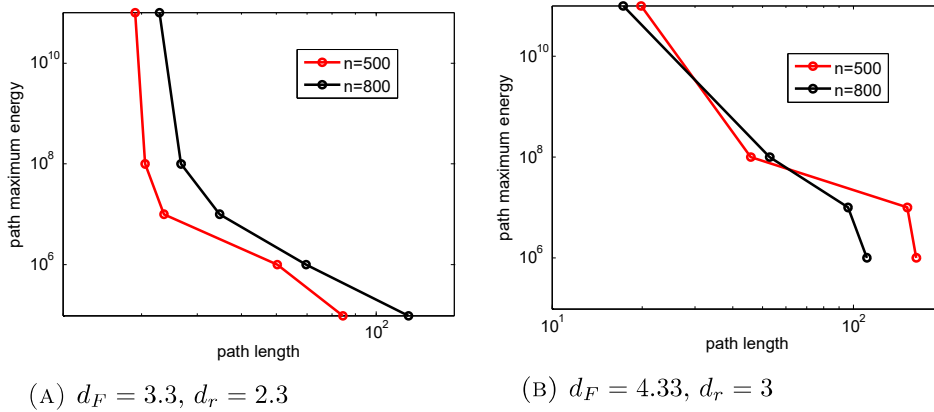


FIGURE 5.9: Path maximum energy versus hops

Changing the fractal dimensions (both streets and relays) does not change the behavior, as illustrated in Figure 5.9b. In this case, the hyperfractal setups have the following base configuration: nodes fractal dimension  $d_F = 4.33$ , relays fractal dimension  $d_r = 3$ , pathloss coefficient  $\alpha = 4$  and we vary the number of nodes,  $n$  to be either  $n = 500$  or  $n = 800$ . Again, making a tougher constraint on the path maximum energy leads to the increase of the path length, showing that achievable trade-offs in hyperfractal maps of nodes with road-side infrastructure.

## 5.4 Short Study on Load and Bottleneck

### 5.4.1 System Model

The system model for this short study contains, as throughout the whole chapter, both the mobile nodes,  $\Phi$  and the relays,  $\Xi$ . In this study we shall not consider any constraints on the radio range or energy consumptions, as these constraints usually generate a more balanced load while we are searching for the extreme case scenario.

Whenever dealing with routing in a network, one must keep in mind that the network links are limited and an interesting question arises: what is the repartition of load in a network given a routing technique? Is there a bottleneck? In the following, we try to observe the behavior of the network load under the routing techniques imposed in this chapter.

### 5.4.2 Main Results

Note that, from now on, we use the term node to refer both mobile to nodes and relays.

**Definition 5.22.** The *load*  $\sigma(x)$  of a node  $x$  is the number of paths that are routed through the respective node.

We do not provide analytically a routing technique such that the load is balanced. Instead, we compute here the load of forwarding nodes under the constraint of minimum path cost routing (either NN, or minimum delay). While the routing strategy is suboptimal in which regards the load balancing, we choose it as the reference routing technique in order to give insights on the load achieved when minimizing the cost and due to its utilization throughout the derivations done in the previous section. Furthermore, a minimum delay routing technique is of interest as it maximizes the network throughput.

In the previous section, the average path cost both for NN routing and for minimum delay routing,  $D_n$  was derived in Theorem 5.18 under the constraint of minimum cost and no constraints on energy or radio range as  $D_n = O\left(n^{1-\frac{2}{(1+1/d_F)d_r}}\right)$ .

In the hyperfractal, there are a total of  $L_n = |G| * (|G| - 1)$  routes between the nodes, where  $|G|$  is the size of the giant component. Throughout the derivations, we make the simplistic assumption that all nodes have equal traffic toward all destinations and each node  $x$  has the same capacity  $C(x) = C$  (similar to the previous section) and supports a load  $\sigma(x)$  as per Definition 5.22.

We further define the following quantities:  $\mu_n$  as the capacity per route and per node,  $C_n$  the total capacity of routes.

*Remark 5.23.* The aggregate throughput of routes that pass through a node is inferior to the capacity of the node.

$$\mu_n \sigma(x) \leq C(x) \tag{5.14}$$

Under these assumptions and observations, the following hold:

**Theorem 5.24.** *The aggregate throughput of routes multiplied by the length of routes is inferior to the sum of the capacity of all the nodes.*

$$L_n C_n \leq \sum_{x \in G} C(x)$$

*Proof.* The average load of the nodes in a hyperfractal is:

$$\mathbb{E}[\sigma(x)] = \frac{D_n L_n}{n + R(\rho)} \quad (5.15)$$

Substituting in (5.14) and multiplying on both sides with  $|G| = n + R(\rho)$ :

$$\mu_n D_n L_n \leq \sum_{x \in G} C(x)$$

As the capacity of the routes is  $C_n = \mu_n D_n$  we arrive to the result that we write as:  $\mu_n D_n L_n (1 + \epsilon) = |G| C$  with  $1 + \epsilon$  a positive number.  $\square$

A lower bound on the capacity of the network can be derived, this time, in function of the network load. The minimum capacity of a route is achieved by minimizing  $\mu_{min} = \min_{x \in G} \left( \frac{C}{\sigma(x)} \right)$ .

Replacing  $\mu_n$  by using (5.14), the minimum will be obtained as:

$$\min \left( \frac{1}{\sigma(x)} \right) = \frac{n + R(\rho)}{D_n L_n (1 + \epsilon)} \quad (5.16)$$

Denote by  $\sigma^* = \max_{x \in G}(\sigma(x))$  the maximum achieved load in the hyperfractal network. As it strongly depends on the employed routing technique,  $\sigma^*$  is a quantity that can be determined only empirically.

**Definition 5.25.** We define by  $\tau = 1 + \epsilon$  as the peak to average load ratio.

From (5.15) and (5.16)  $\tau = \frac{\sigma^*}{\mathbb{E}[\sigma]}$ . This quantity shows whether the load is balanced in the network. A high peak-to-average load ratio implies the existence a bottleneck, a node that is charged with routing considerably more routes than the other nodes in the network and that can represent a point of failure. Being a function of  $\sigma^*$ , the value of  $\tau$  is determined through simulations.

The lower bound on capacity is therefore achieved for the bottleneck  $\mu_{min} = \frac{C}{\sigma^*}$ . Consequently:

**Corollary 5.26.** *The network capacity in a hyperfractal is higher than:*

$$C_n \geq \frac{C}{\sigma^*} |G| (|G| - 1)$$

where  $\sigma^*$  is the maximum load achieved in the network.

This corollary shows that the network capacity is limited by the bottleneck of the network, therefore, a routing technique that provides a low peak to average load can be beneficial for the network capacity.

Notice that all of these observations are quite general and not conditioned on the model. The only metric conditioned by the model is the average path length,  $D_n$ .

## 5.5 Simulations

The simulations are performed by using both routing strategies. For the minimum delay routing, it is assumed that each transmitting node uses the same nominal transmit power and that the received signal is affected by path-loss denote in this section as  $l(i, j)$  and Rayleigh fading (note that in this study we do not use power control). Path-loss between node  $i$  and node  $j$  is modeled by the power-law function  $l(i, j) = (Ar)^{\alpha}$  when the two nodes  $i$  and  $j$  are aligned, where  $A, \alpha$  are some constants and  $r$  is the distance between transmitter and receiver, otherwise  $l(i, j) = 0$ . The reception undergoes Rayleigh fading  $F_{ij}$  independent over nodes and time, which is independently sampled at each time slot for each transmitter-receiver pair. Given this, the signal received by receiver  $j$  from transmitter  $i$  at time slot  $t_n$  becomes  $F_{ij}l(i, j)$ . Throughout this work, we restrict to the case of Rayleigh fading, thus by renormalization of  $A$  when necessary,  $F$  is a non negative random variable with exponential distribution of mean 1.

By assuming the background noise power negligible, and that node  $i$  is in transmit mode, the successful reception of a signal transmitted from node  $i$  to a node  $j$  at a given time slot occurs when:  $F_{ij}l(i, j) > K \sum_{k \in B - \{i\}} F_{kj}l(k, j)$ , where  $K$  is the SIR threshold related to the bit-rate when a particular modulation plus coding scheme is considered. where  $I(j)$  is given by  $\sum_{b \in B^n} \frac{F_{(b,j)}^n}{l(\|b-j\|)}$ .  $B$  is the subset of nodes transmitting at the considered time slot.

In order to avoid time-consuming simulations of Aloha protocol, the following results are used for computing the probabilities of successful reception,  $p_{ij}$  when independent Rayleigh fading is applied [120]:  $p_{ij} = p_A(1 - p_A) \prod_{k \neq i, j} w_{kj}(K/l(i, j))$ , where  $w_{kj}(\theta)$  is the Laplace transform of the pdf of the signal produced by node  $k$  over node  $j$ ,  $p_A$  is the Aloha medium access probability, and  $K$  is the Signal to Interference Ratio (SIR). In the following, the pathloss coefficient  $\alpha = 4$  and  $K = 1$ . In this case, as the results is more general, the pathloss is taken as 4, a more pessimistic value. The validations are performed for several configurations with different values of  $n, d_F$  and  $d_r$ .

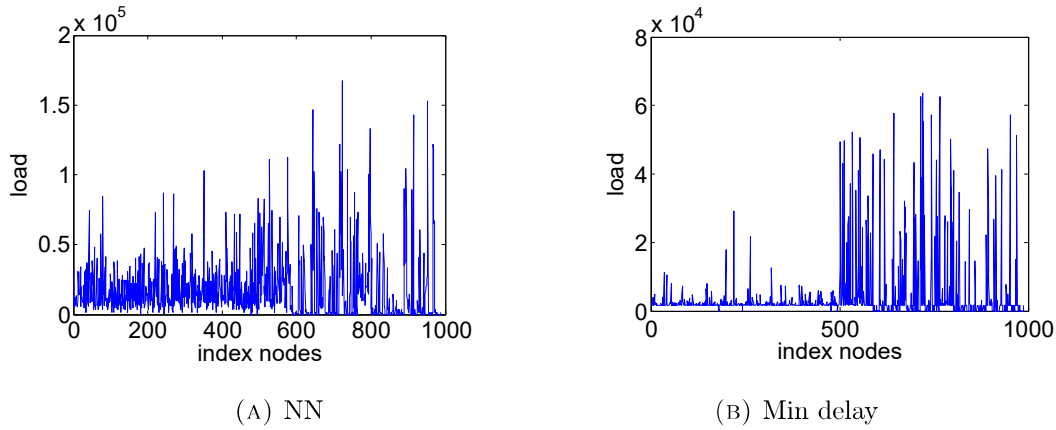


FIGURE 5.10: Load distribution in hyperfractal  $d_m = 3.3$ ,  $d_r = 2.3$ , nodes index up to index 500, relays index starting from index 500

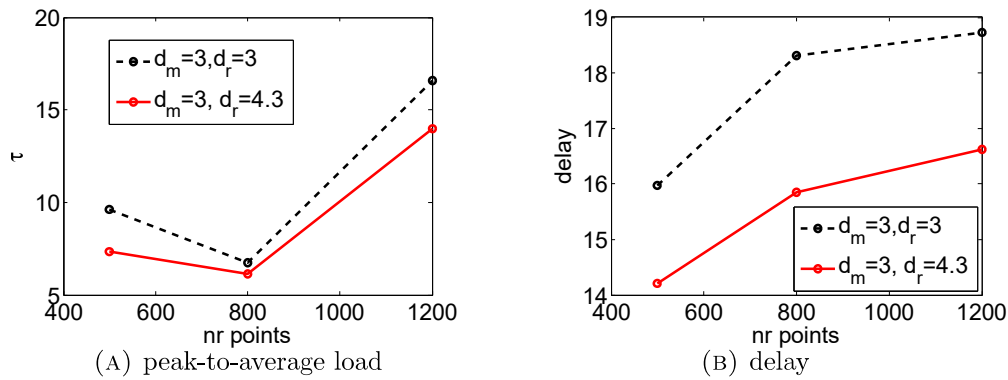


FIGURE 5.11: Peak-to-average load (a) and delay (b) for two configurations, NN routing

Figure 5.10a showcases the distribution of load for a hyperfractal configuration  $d_F = 3.2$ ,  $d_r = 2.3$  for the nearest node routing strategy. The indexes of the relays start after the index 500. Notice that the relays support loads of routes that are superior to the load supported by the mobile nodes, with a easily distinguishable maximum.

When using the minimum delay routing strategy, the load distribution changes dramatically, see Figure 5.10b. For the same hyperfractal configuration,  $d_F = 3.2$ ,  $d_r = 2.3$ , the relays are heavily loaded, while the mobile nodes support a much lighter traffic.

Let us look now to the peak-to-average load,  $\tau$ , and the delay in two configurations. Figure 5.11a shows the peak-to-average load for different values of  $n$  in two configurations, with the same fractal dimension of mobile nodes,  $d_F = 3$ , but different value for the fractal dimension of relays,  $d_r = 3$  in the first configuration, and  $d_r = 4.3$  in the second one. One can easily notice that the load is better balanced when the fractal dimension of relays is higher. Figure 5.11b confirms that the second configuration outperforms the first

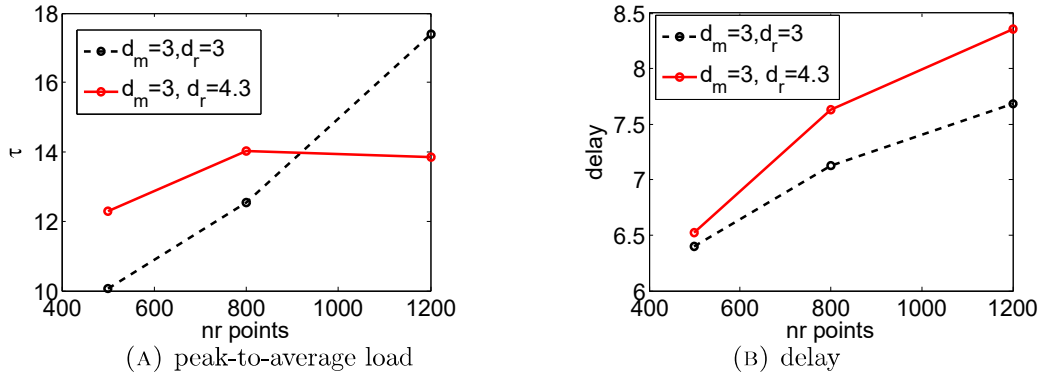


FIGURE 5.12: Peak-to-average load (a) and delay (b) for two configurations, min delay routing

configuration as the delay achieved in the second configuration is inferior to the delay achieved when  $d_r = 4.3$ .

For the minimum delay routing technique, Figure 5.12a shows the peak-to-average load for different values of  $n$  in two configurations, with the same fractal dimension of mobile nodes,  $d_F = 3$ , but different values for the fractal dimension of relays,  $d_r = 3$  and  $d_r = 4.3$ , respectively. In this case, the first configuration offers a lower delay, yet the bottleneck of the network with the increase of nodes evolves better for the second configuration. This suggests that the choice of the fractal dimension of the infrastructure has to be done accordingly, with respect to the quality of service constraints and allowed trade-offs.

## 5.6 Concluding Remarks

This chapter has presented a piece of work that answers some of the most crucial questions of ad-hoc networks: the connectivity, the energy consumption and the routing delay. More precisely, we have provided achievable trade-offs between energy consumption and routing delay, all while maintaining the connectivity of the network under the required energy constraints: path total energy or energy per transmitting node.

While developing the answers to this critical questions, we have provided insights for the design and operation of vehicular networks using millimeter wave technology under hyperfractal model. Several observations that arose as secondary results have also been presented. These secondary results debate on the bottleneck in hyperfractals networks under specific routing techniques.

## Chapter 6

# Application to Ad-Hoc networks. Delay-Tolerant Networks

### 6.1 Introduction and Motivation

As the hyperfractals are models inspired from the locations of connected devices that inherit the locations of humans on streets, it comes as natural that the main use of the hyperfractals is to serve for the modeling of the vehicular networks.

In the following, we propose the study of the broadcast of a packet of information in a vehicular delay tolerant network. We will derive bounds for the broadcast time by exploiting the properties of the hyperfractal model and we will raise awareness of specific phenomenons that appear due to network's self-similarity and the consequences of these phenomena.

A distributed network of vehicles such as vehicular ad-hoc network (VANET) can easily be turned into an infrastructure-less self-organizing traffic information system, where any vehicle can participate in collecting and reporting useful information. As the number of vehicular networks continue to grow and now create giant networks (with diverse hierarchical structures and node types), vehicular interactions are becoming more complex. This complexity is further exacerbated by the time-space relationships between vehicles. The intrinsic mobility of the vehicles on the roads leads to highly dynamic and evolutionary topologies that can no longer be adequately modeled through methods inherited from previous networks generations.

Disseminating information in a network is typically done in a broadcast-oriented way [121–123]. Broadcast in vehicular networks can be done with the help of the adjacent infrastructure, yet, in this work, we focus on the study of infrastructure-less vehicular networks to understand their performance limits. Broadcasting schemes, rather than unicasting, are particularly adequate for vehicular networks due to the mobility of the cars, which implies an ongoing evolving topology. In broadcast protocols, the advantage stands in the fact that the vehicles do not require the knowledge of a specific destination location or its relevant route. This eliminates the complexity of route discovery, address resolution and the previously mentioned topology management with mobility, which are critical aspects in dynamic networks such as vehicular networks. Broadcast protocols have been enhanced throughout the past years in order to minimize the redundancy and energy consumption, to reduce the security issues [124], increase reliability and comparisons have been made between the achievable performances with and without road-side infrastructure [123].

Vehicular networks have specific requirements and challenges, as shown in [125, 126] that can be sometimes overcome by exploiting the mobility [127]. Moreover, in [128], the authors show that the urban architecture features, more specific the intersections, can be used to ease the dissemination of information in vehicular networks.

In making use of the delay tolerant property of ad-hoc networks, an important work has been done in [37, 129], where a thorough analysis is provided for the broadcast time in a delay tolerant network. In [130], the authors exploit social relationship for proposing a routing protocol for delay-tolerant networks (DTN), while in [131], the authors analyze routing protocols performances obtained in DTN. Other metrics in delay-tolerant networks have been analyzed in [132, 133]

The work done in [134] gives an in-depth analysis of the topological properties of a vehicular network, with a focus on the mobility models while [135] presents a thorough study on the importance of location for routing protocols in ad-hoc networks.

In this Chapter, in order to extend the understanding of the hyperfractal model, and further demonstrate its capabilities, we study the time limit requirements for a piece of information to propagate in an urban vehicular network, by exploiting the model.

On one hand, our aim is to better exhibit the impact on the broadcast time of the particular environment, the traffic and network topologies. We advocate that network geometry should indeed be considered and exploited when designing broadcast protocols. On the other hand, we aim at demonstrating the ease of use of the hyperfractal model and how it can be exploited to enhance the computing wireless networks KPIs (Key Performance



Indicators). For instance, most of broadcast protocols parameters are dependent on traffic density and this is a metric which can be predicted when considering the particular network geometry.

We will prove here that the average broadcast time in a hyperfractal setup is in  $O(n^{1-\delta} \log n)$  where  $n$  is the number of mobile nodes and where  $\delta$  is a parameter depending on the fractal dimension.

## 6.2 System Model

In this Chapter, we use the process  $\Phi$  as the model for the locations of vehicles in the network. We do not make use of the process  $\Xi$  here which will lead to the generation of the delay-tolerant network, as, in the absence of the relays, the propagation of the packets through intersections, even with the help of mobility, will require the existence of buffers that can hold the packet for a longer time. We make use of several properties of the process  $\Phi$  but we also develop extra results that will be useful in deriving the main theoretical contributions.

As the density of the population on the streets rapidly decays with the increase of the level, there will be unpopulated streets. Therefore, we say that a street is *busy* if the street contains at least one mobile node.

The following lemma will play an important role in the proof of our main results:

**Lemma 6.1.** *The average number of busy streets is asymptotically equivalent to  $n^{\delta} \frac{-\Gamma(-\delta)}{\log(2/q)}$  with  $\delta = \frac{\log 2}{\log(2/q)}$  where  $\Gamma$  stands for Euler “Gamma” function.*

The mobiles move on the lines that are the support of the hyperfractal map. When a node reaches a boundary, it reenters the map from the same point, following a billiard mobility. Initially, for the sake of simplicity, the speed of the mobiles is considered to be constant and identical,  $v$ , no matter the level and the density of the nodes on the lines. In reality, the values of speed vary in certain intervals. As our analysis is focused on upper and lower bounds, the variation will not impact the order of magnitude. The case of variable speed will be discussed later, in Section 5.5 where we show that the bounds are validated for variable speed case as well. We will not analyze the case where some streets are congested and thus speed up the broadcast as some nodes are blocked in intersections.

### 6.2.1 Canyon Effect

Here again, we will use the canyon effect as the characteristic propagation phenomenon in urban environment.

We remind the reader that the *canyon* propagation model implies that the signal emitted by a mobile node propagates only on the street where it stands on. If the network was static, considering the given construction process, the probability that a mobile node is placed in an intersection goes to zero when the street width goes to zero and nodes positioned on two different streets are never able to communicate. Notice that when a street has positive width, the intersection width is negligible compared to the street length and the network will still be partitioned. The connectivity of the network is thus ensured through the mobility of the nodes, leading to a scenario of a delay tolerant network.

### 6.2.2 Broadcast Algorithm

A feasible approach to forward a packet of information from a source to a destination in the absence of any predictive knowledge on the node movement is the epidemic routing, analog to the spreading of an infectious disease. In this case, when the traffic is low, epidemic routing can achieve an optimal delivery delay at the expense of increased use of network resources. The considered broadcast protocol is a single-hop broadcast meaning that each vehicle carries the information while traveling, and this information is transmitted to the other vehicles in its one-hop vicinity (nearest neighbors of the infected node) during the next broadcasting cycle. This single-hop broadcasting protocol relies heavily on the mobility of the vehicles for spreading information.

In this study, as we primarily seek to understand the limit of the propagation speed, we do not consider other detailed aspects of the broadcast protocol, such as packet collisions. Later on, in the simulations section, all the protocol stack will be implemented. At time  $t_0 = 0$  only one node, called “source”, holds the packet. At time  $t > t_0$ , the population of nodes is split among nodes that have received the packet, called infected nodes, and nodes that have not yet received the packet, called healthy nodes by analogy with epidemic propagations.

The measured broadcast time represents the time needed for the entire network contamination starting from a single random source. The average broadcast time is obtained by averaging over all possible sources, as it will be further defined in the following section.

## 6.3 Main Results

In this section we provide the computation of broadcast time when the network of vehicles is modeled using the hyperfractal model for nodes. We show that the computations are simplified due to the scaling effect of the hyperfractal. In particular, given the self-repeating pattern of streets with hierarchical density, we can compute metrics of interest by observing a local scenario (for such a pattern) and then use the lessons learned to the whole network.

The main results are first proven under the assumption that each node is reachable through wireless propagation by its nearest neighbor, therefore that the radio range is always high enough to reach the next hop. A reasoning behind this assumption can be that the communications between vehicles has a preliminary sensing phase through which it determines the necessary transmission power for the transmission to reach the next neighbor. Another reasoning is that, even under the assumption that the transmission range is high enough in order to reach several vehicles on the street, due to the interferences, the highest SINR (Signal-to-Noise plus Interference) ratio is the one experiences by the nearest neighbor.

The results provided are as following: the evaluation of matching generic upper and lower bounds for the average broadcast time in a hyperfractal setup. Then, specific results in extremes cases are provided. It will be shown that the performance is due in part to an interesting self-similar phenomenon, denoted as *information teleportation*, that arises as a consequence of the topology and allows an acceleration of the broadcast therefore decreasing the broadcast time. We then provide the extension of the results when radio range is considered.

Throughout the following analysis, without lack of generality, we only consider streets which are busy streets as in Lemma 6.1.

### 6.3.1 Upper Bound

There are always interesting observations to be made on the hyperfractal model that lead to simplification of reasoning and computation. These observation lead to an intuitive computation of the bounds. For example, the following remark is a immediate consequence of the construction process.

*Remark:* There are  $2^H$  streets of level  $H$  intersecting each of the streets forming the central cross. Due to the canyon effect, the packet will not be able to jump from a street to another street, but has to be propagated through intersections. This will be done when

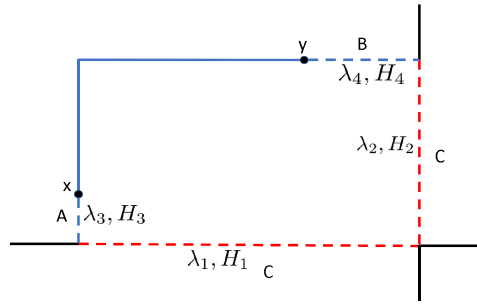


FIGURE 6.1: Direct route versus directed route

a node carrying the packet crosses the intersection. We denote by  $I(n_i, n_j)$  the average time that a packet takes to jump from one street containing  $n_i$  nodes to an intersecting street containing  $n_j$  nodes, assuming all nodes on the first street carry the packet. In fact, it is sufficient to assume that the closest nodes towards the intersection carry the packet.

In the following, for sake of generality, we deal with the case where the nodes of interest,  $x$  and  $y$ , are placed on perpendicular lines of respective depths,  $H_a$  and  $H_b$ . The location of  $x$  denotes the location of the node on line of level  $H_a$  that initiates the broadcast. The location of  $y$  denotes the location of a node on line  $H_b$  that will receive the packet. In fact, due to the mobility of the nodes, one cannot fix from the start of the broadcast the location of node  $y$ . Furthermore, as the time when the packet arrives from one route on a specific location on the line  $H_b$  can differ from the case the packet comes from a different route, we cannot choose the location of a node in a fix moment in time. Therefore, we choose  $y$  to be the representation of a location of a node  $y$  on line  $H_b$  on the segment  $[y_0 - 1/\lambda_{H_b}, y_0 + 1/\lambda_{H_b}]$ , where  $y_0$  denotes the position of a node on line  $H_b$  when the broadcast was initiated by node  $x$ .

**Definition 6.2.** We define by  $T_n(x, y)$  the time necessary for a packet transmitted in a broadcast initiated by node  $x$  to arrive at node  $y$ . We define by  $\mathbf{E}[T_n(x, y)]$  the average broadcast time between all fixed  $(x, y)$  pairs.

**Definition 6.3.** The direct route is the route that uses the streets that embed the nodes  $x$  and respectively,  $y$  and contains the intersection between these two streets.

**Definition 6.4.** A diverted route between nodes  $x$  and  $y$  is a route that employs four segments and three intersections.

As an example, in Figure 6.1, the direct route is drawn in continuous blue line and the diverted route is drawn in dotted red line and dotted blue line.

We can now make the observation that placing the nodes  $x$  and  $y$  on parallel streets of different depth would just lead to an extra term in the following developments, that

would not be relevant as it would not change the order of size, as it would exist in both scenarios, the direct street scenario and the diverted street scenario.

The following Lemmas give intuitive results that will be further used in the development of the bounds.

**Lemma 6.5.** *Assume that the street of level  $H_a$  holding node  $x$  contains  $n_a$  nodes, and the street of level  $H_b$  holding node  $y$  contains  $n_b$  nodes. Given a transmission hop time  $h$ , the bound on the time  $T_n(x, y)$  in the direct route is:*

$$T_n(x, y) \leq hn_a + hn_b + I(n_a, n_b). \quad (6.1)$$

*Proof.* To prove the formulae, let us look at the setup illustrated in Figure 6.1. In the direct route case it is assumed that the packet hops from node  $x$  towards the intersection with the street holding the node  $y$  (straight, blue line). The maximum number of hops is  $n_a$ , thus it takes at most  $hn_a$  time units. The packet turns on the intersection in time  $I(n_a, n_b)$  and then proceeds towards node  $y$  in at most  $hn_b$  time units.  $\square$

**Lemma 6.6.** *Consider the diverted route containing two additional streets of level  $H_c$  and level  $H_d$ , respectively perpendicular to the street holding  $x$ , and perpendicular to the street holding  $y$ , and containing respectively  $n_c$  nodes and  $n_d$  nodes. Assuming  $n_c$  and  $n_d$  strictly positive, in the diverted route, the bound on  $T_n(x, y)$  becomes:*

$$\begin{aligned} T_n(x, y) \leq & h(n_a L(H_c) + 1) + h(n_b L(H_d) + 1) \\ & + I(n_a, n_c) + I(n_b, n_d) + I(n_c, n_d) \\ & + hn_c + hn_d \end{aligned} \quad (6.2)$$

where  $L(H_i)$  is the distance from a node to the intersection with a street of level  $H_i$ .

*Proof.* Let us again look at the setup illustrated in Figure 6.1. It is assumed that, instead of taking the direct route as expressed in inequality (6.1), the packet is diverted into the street of level  $H_c$ , then to the street of level  $H_d$  before being delivered on the street of node  $y$  (dashed, red line). The quantity  $h(n_a L(H_c) + 1)$  and  $h(n_b L(H_d) + 1)$  is the time necessary for the packet to propagate from  $x$  to the intersection with the street of level  $H_c$  through hop-by-hop propagation, and similarly, the time necessary for the packet to propagate from the intersection of the street of level  $H_d$  to node  $y$ . The average number of nodes between  $x$  and the streets of level  $H_c$  is  $n_a L(H_c)$ , due to the uniform node distribution on the interval. Even in considering the node mobility and the time difference between each hop, the mean remains the same since the distribution of nodes remains uniform on

the interval. The additive term  $+1$  in the final result comes from the fact that the closest node moving towards the intersection may be located beyond the intersection.  $\square$

The following lemma gives an estimate of the packet turn time at an intersection.

**Lemma 6.7.** *In a hyperfractal map with  $n$  nodes, where all nodes move with constant speed  $v$ , for all  $n_i, n_j \in \mathbb{N}^*$ , the following inequality holds:*

$$I(n_i, n_j) \leq \frac{1}{v(n_i + n_j)}. \quad (6.3)$$

where  $I(n_i, n_j)$  is the packet turn time at the intersection between the streets holding  $n_i$  nodes, respectively  $n_j$  nodes.

*Proof.* Let  $\Delta$  be the distance between an intersection and a node moving toward the respective intersection. It is assumed, without loss of generality, that the packet originally progresses on an East-West street and that the intersection stands at abscissa  $z \in [0, 1]$ .

Let  $g > 0$  be the distance toward the intersection of the closest node moving toward the intersection. An upper bound on the probability that  $\Delta > g$ :  $\Delta$  is greater than  $g$  when no node is either in the interval  $[z - g, z]$  and is not moving toward the right, or is in the interval  $[z, z + g]$  and is moving toward the left. The probability of such event is upper bounded by  $(1 - g)^n$ , in fact it is exactly this expression when  $z \in [g, 1 - g]$ , omitting border effects.

The car at distance  $\Delta$  reaches the intersection in  $\frac{\Delta}{v}$  time units. At this time the car can transmit the packet to the closest car on the North-South street. Now, merging the problem over the two streets together, the probability that the time for the packet to turn to be larger than  $g/v$  is equal to the probability that no car on the East-West street and on the North-South street reaches the intersection before  $g/v$  time units, which is upper bounded by  $(1 - g)^{n_i}(1 - g)^{n_j}$ . Thus

$$vI(n_i, n_j) \leq \int_0^1 (1 - g)^{n_i + n_j} dg = \frac{1}{n_i + n_j}.$$

$\square$

The following technical result gives the probability that a street is busy and will be further used in the development of the bounds.

**Lemma 6.8.** *In a hyperfractal with  $n$  nodes and  $d_F > 2$ , the probability that a street a level  $H(n)$ , with  $n_c$  mobile nodes on the street and  $H(n) = \lceil \frac{\log(n^{1-\epsilon}p/2)}{\log(2/q)} \rceil$  is empty is smaller than  $e^{-(q/2)n^\epsilon}$ .*

*Proof.*

$$\mathbb{P}(n_c = 0) = (1 - \lambda_{H(n)})^n < e^{-n\lambda_{H(n)}} \leq e^{-(q/2)n^\epsilon}$$

In other words, the probability that a street is empty is the probability that the procedure of placing the  $n$  nodes has never selected the level  $H(n)$ . As the nodes are placed on a level following a Poisson distribution, we can use the exponential expressing and immediately get the result.  $\square$

The following theorem gives the upper bound on the broadcast time and proves that it grows as  $n^{1-\frac{1}{d_F-1}}$ , showing that the growth is sub-linear and only depends on the fractal dimension.

**Theorem 6.9.** *In a network with  $n$  mobile nodes placed in a hyperfractal setup with fractal dimension  $d_F > 2$ , transmission hop time  $h$  and constant speed of vehicles  $v$ , consider  $x$  and  $y$  be two nodes on perpendicular streets. When  $n \rightarrow \infty$  the average broadcast time satisfies:*

- (i) in the direct route scenario

$$\mathbf{E}[T_n(x, y)] \leq hpn + \frac{1}{v}; \quad (6.4)$$

- (ii) in the diverted route scenario, for all  $\epsilon > 0$

$$\begin{aligned} \mathbf{E}[T_n(x, y)] \leq & 2hpn^{1-\delta+\epsilon} \left(\frac{2}{p}\right)^\delta + \frac{4}{q}hn^{\epsilon/\delta} \\ & + \frac{3}{v} + O(ne^{-(q/2)n^\epsilon}) \end{aligned} \quad (6.5)$$

where  $\delta = \frac{1}{d_F-1}$ .

*Proof.* As we look for the upper bound, the inequality in the direct case (eq.6.4) comes straightforward as  $\mathbf{E}[n_a + n_b] < pn$ . The term  $\frac{1}{v}$  is the upper bound of  $I(n_i, n_j)$  therefore maximizing the sum. The diverted route scenario again follows Figure 6.1. Both  $n_c$  and  $n_d$  are strictly positive with high probability. Indeed the probability that  $n_c = 0$  is  $e^{-n\lambda_c}$ . Let us take  $H_c = H_d = H(n)$  with  $H(n) = \lceil \frac{\log(n^{1-\epsilon}p/2)}{\log(2/q)} \rceil$  as per Lemma 6.8, thus:

$$\frac{\log(n^{1-\epsilon}(p/2))}{\log(2/q)} - 1 \leq H(n) \leq \frac{\log(n^{1-\epsilon}(p/2))}{\log(2/q)} + 1.$$

We have both:

$$\mathbf{E}[n_c] = \mathbf{E}[n_d] \leq n^\epsilon \frac{2}{q}.$$

Meanwhile, let us take as diverted route the closest street of level  $H(n)$  from node  $x$  since this street is busy with probability higher than  $e^{-(q/2)n^\epsilon}$ . In this case:

$$L(H(n)) \leq 2^{-H(n)} \leq 2n^{-\delta(1-\epsilon)} \left(\frac{2}{p}\right)^\delta.$$

Consequently:

$$\frac{p}{2} n 2^{-H(n)} \leq p n^{1-\delta+\delta\epsilon} \left(\frac{2}{p}\right)^\delta$$

and the result is obtained by changing the value of  $\epsilon$  in  $\epsilon/\delta$ .

The term  $O(ne^{-(q/2)n^{\epsilon/\delta}})$  comes from the case when either  $n_c = 0$  or  $n_d = 0$  which arrives with probability  $e^{-(q/2)n^\epsilon}$ . In this case, we know that  $T_n(x, y) \leq hpn + \frac{1}{v}$  thus the contribution to  $\mathbf{E}[T_n(x, y)]$  is  $O(ne^{-(q/2)n^\epsilon})$ .  $\square$

**Remark** As  $\epsilon$  becomes smaller, the convergence of eq. (6.5) is slower.

**Remark** The quantity  $\delta$  is strictly less than 1 ( $\delta < 1$ ) and tends to 1 when  $d_F \rightarrow 2$ .

**Remark** In fact the term  $3/v$  is far too high while its weight in the sum should not be of high importance. Using Lemma 6.3, the term can be replaced by  $\frac{2}{vn} + \frac{1}{vn^{\epsilon/\delta}}$ . Notice that the optimal value of  $\epsilon$  is of order  $\frac{\log \log n}{\log n}$  which does not reach negligible values as long as  $n \ll \frac{1}{hv}$  and leads to the global estimate  $\mathbf{E}[T_n(x, y)] = \mathcal{O}(n^{1-\delta \log n})$ .

**Definition 6.10.** The average broadcast time  $T_{broadcast}$  is the average of all source-destination pairs  $(x, y)$  of  $\mathbf{E}[T_n(x, y)]$ .

**Corollary 6.11.** When  $n \rightarrow \infty$ , the average broadcast time as the average over all sources  $x$  satisfies:

$$T_{broadcast} = O(n^{1-\delta} \log n) \tag{6.6}$$

Here, by all sources  $x$  we mean that we compute the broadcast time started by each source and average over all sources.



### 6.3.2 Lower Bound

The intuition behind the lower bound of the average broadcast time comes from the fact that the highest weight in the broadcast time is taken by the time that the packet hops on the main cross, where the density of mobile nodes is considerably higher than on the following levels.

**Theorem 6.12.** *Consider a network with  $n$  mobile nodes in a hyperfractal setup with fractal dimension  $d_F > 2$ , transmission hop time  $h$ , constant speed of vehicles  $v$ ,  $\delta = \frac{1}{d_F-1}$  and  $\Gamma$  stands for Euler “Gamma” function. The average broadcast time satisfies:*

$$T_{broadcast} \geq \frac{p^3}{2} h n^{1-\delta} \frac{\log(2/q)}{-\Gamma(-\delta)} \quad (6.7)$$

*Proof.* The broadcast time verifies:

$$T_{broadcast} = \frac{1}{n^2} \sum_{(x,y)} \mathbf{E}[T_n(x,y)] \quad (6.8)$$

when  $(x, y)$  are all the possible pairs of two nodes in the hyperfractal.

We denote by  $\mathcal{H}$  the set of nodes on the horizontal segment belonging to the central cross and  $\mathcal{V}$  the set of nodes on the vertical segment of the central cross.

As we compute the sum only over the terms on the central cross,

$$T_{broadcast} \geq \frac{1}{n^2} \left( \sum_{\substack{x \in \mathcal{H} \\ y \in \mathcal{V}}} \mathbf{E}[T_n(x,y)] + \sum_{\substack{x \in \mathcal{V} \\ y \in \mathcal{H}}} \mathbf{E}[T_n(x,y)] \right) \quad (6.9)$$

as the number of the terms in the sum in (6.9) is lower than the total number of terms in the sum in (6.8).

Since the packet must leave the street of node  $x$ , it must at least run on a distance  $L(x)$  which is the average distance from node  $x$  to the closest busy perpendicular street. The same holds for reaching node  $y$ . In other words, the following inequality holds:

$$\mathbf{E}[T_n(x,y)] > h p n \mathbf{E}[L(x)].$$

Assume that the node  $x$  is on the East-West segment of the central cross. The average distance to the closest North-South busy street is larger than  $\frac{1}{2\mathbf{NS}_n}$ , where  $\mathbf{NS}_n$  is the random variable expressing the number of busy North-South streets in presence of  $n$

mobile nodes. Therefore,  $E[L(x)] \geq \mathbf{E}[\frac{1}{2\mathbf{NS}_n}]$ . The lowest value would be obtained if the busy North-South streets were equally spaced.

By Lemma 6.1, one has  $E[\mathbf{NS}_n] = \frac{1}{2}B_n$ . Furthermore  $E\left[\frac{1}{\mathbf{NS}_n}\right] \geq \frac{1}{E[\mathbf{NS}_n]}$  by convexity of the hyperbolic function. Thus by referring to Lemma 6.1:

$$\mathbf{E}[T_n(x, y)] > \frac{hpn}{B_n} = hpn \frac{\log(2/q)}{-\Gamma(-\delta)}.$$

Using the fact that  $\mathbf{E}[|\mathcal{H}||\mathcal{V}|] = (n-1)np^2/4$  terminates the proof.  $\square$

Notice that, for practical computations, there is not a need for an exact expression of the number of busy streets. The value of  $E[L(x)]$  can be simply determined as 1/number of levels in the map.

**Corollary 6.13.** *The average broadcast time when  $n \rightarrow \infty$  satisfies:*

$$T_{broadcast} = \Omega(n^{1-\delta}) \quad (6.10)$$

Remark: When  $n = 2$ , following expression (6.4),  $T_{broadcast} < h + \frac{1}{v}$ . Furthermore, the same holds for the cases when all nodes are on the same street or move on two perpendicular streets.

Combining Corollary 6.11 and the lower bound of Theorem 6.12, one obtains the matching result:

**Corollary 6.14.** *The average broadcast time when  $n \rightarrow \infty$  satisfies:*

$$\lim_{n \rightarrow \infty} \frac{\log T_{broadcast}}{\log n} = 1 - \delta \quad (6.11)$$

### 6.3.3 Asymptotic to Poisson Uniform

This asymptotic case is studied for scientific interested. We do not believe, however, that a network of vehicles, can, at any time, be modeled as uniform Poisson Point Process, yet, as it is the major model used by the stochastic geometry community when dealing with wireless networks, we hereby observe the following.

As previously mentioned, the asymptotic case when  $\delta = 1$  gives a Poisson uniform case. This scenario works as following: the mobile nodes are placed randomly on the plane move on predefined motion directions (either North-South or South-North, either East-West or West-Est). Every node is alone on its road, the only occasion when a car can

communicate is when another car crosses its road. A single node moving on a East-West street sees and transmits a packet towards all the North-South moving nodes crossing its street in  $\mathcal{O}(\frac{1}{v} + h)$  time. Furthermore, one of these nodes moving on a North-South street transmits the packet to all East-West moving nodes also in  $\mathcal{O}(\frac{1}{v} + h)$  time, thus the total broadcast time is:

$$T_{broadcast} = \mathcal{O}(\frac{1}{v} + h) \quad (6.12)$$

which is equivalent into letting  $\delta = 1$  in the general formula.

### 6.3.4 Extension with Limited Radio Range

When a car correctly receives the packet, it transfers it to all the cars that are within its radio range. Up until this moment, throughout this work, we have used the hypothesis of unlimited radio range. In this section we will investigate the more realistic hypothesis of limited radio range.

In the following, the radio range is dependent of the number of mobile nodes in the city map,  $R_n = \frac{1}{\sqrt{n}}$ . The reason is the following. The population of a city (in most of the cases) is proportional to the area of the city and the population of cars is proportional to the population of the city, therefore the population of cars is proportional to the area of the city,  $Area = A \cdot n$  where  $A$  is a constant. A natural assumption is that the absolute radio range,  $R$ , is constant. But since we assume in our model that the city map is always a unit square, the relative radio range in the unit square must be  $R_n = \frac{R}{\sqrt{An}}$  which we simplify in  $R_n = \frac{1}{\sqrt{n}}$ .

As the radio range is fixed and the average distance between nodes increases with the increase of the depth, some nodes will become unreachable. Therefore, the condition for a piece of information to be broadcasted on a street is that the average distance between nodes is not higher than the radio range.

The following Lemma is an adaption of Lemma 6.8 and gives the maximum depth of the level on which the average distance between nodes allows for the propagation of the packet.

**Lemma 6.15.** *In a hyperfractal with  $n$  nodes and  $d_F > 2$ , the probability that a street a level  $H(n)$  with  $H(n) = \lceil \frac{\log(n^{1/2-\epsilon} p/2)}{\log(2/q)} \rceil$  has at least one inter-node gap higher than  $R_n$  is  $n e^{-(q/2)n^\epsilon}$ .*

*Proof.* The probability that a car is not followed by another car within distance  $R_n$  is equal to  $(1 - R_n \lambda_{H(n)})^n$  which is smaller than  $e^{-n^{1/2} \lambda_{H(n)}}$ . Given  $n_c$ , the probability that

there exists such a node (the car within distance  $R_n$  of the car holding the packet) is smaller than  $n_c e^{-\sqrt{n}\lambda_H(n)}$ . With  $n_c \leq n$  the lemma is proved.  $\square$

Similarly, Lemma 6.1 becomes:

**Lemma 6.16.** *The average number of busy streets where there is no inter-node gap higher than  $R_n$  is asymptotically equivalent to  $n^{\delta/2} \frac{-\Gamma(-\delta)}{\log(2/q)}$  with  $\delta = \frac{\log 2}{\log(2/q)}$  where  $\Gamma$  stands for Euler “Gamma” function.*

The proof follows the proof of Lemma 6.1, by adding the factor  $R_n$  to  $\lambda_H$ . As it adds no extra scientific contribution to the proof of Lemma 6.1, the proof will not be detailed.

In this case, the upper bound rewrites as follows.

**Theorem 6.17.** *Consider a network with  $n$  mobile nodes in a hyperfractal setup with fractal dimension  $d_F > 2$ , transmission hop time  $h$  and constant speed of vehicles  $v$ . Let  $x$  and  $y$  be two nodes on perpendicular streets. When  $n \rightarrow \infty$ , for a transmission radio range of  $R = \frac{1}{\sqrt{n}}$ , the average broadcast time satisfies:*

- (i) in the direct route scenario

$$\mathbf{E}[T_n(x, y)] \leq hpn + \frac{1}{v};$$

- (ii) in the diverted route scenario, for all  $\epsilon > 0$

$$\mathbf{E}[T_n(x, y)] \leq 2hpn^{1/2-\delta+\epsilon} \left(\frac{2}{p}\right)^\delta + \frac{4}{q}hn^{\epsilon/\delta} + \frac{3}{v} + O(ne^{-(q/2)n^\epsilon})$$

where  $\delta = \frac{1}{d_F-1}$ .

Following the same reasoning, the lower bound becomes:

**Theorem 6.18.** *Consider a network with  $n$  mobile nodes in a hyperfractal setup with fractal dimension  $d_F > 2$ , transmission hop time  $h$ , constant speed of vehicles  $v$ ,  $\delta = \frac{1}{d_F-1}$  and where  $\Gamma$  stands for Euler “Gamma” function. For a transmission radio range of  $R = \frac{1}{\sqrt{n}}$ , the average broadcast time satisfies:*

$$T_{\text{broadcast}} \geq \frac{p^3}{2}hn^{1-\delta/2} \frac{\log(2/q)}{-\Gamma(-\delta)}$$

The proof follows the same steps as the proof of Theorem 6.12, using the result of Lemma 6.16 instead of Lemma 6.1.

Notice that, for the limited radio range bounds, we no longer have the equivalent the unifying Corollary 6.14, as the exponent of  $n$  in the upper bound is  $1/2 - \delta$  while in the lower bound the exponent is  $1 - \delta/2$ .

However, in the simulations section, we shall prove that the bounds obtained for unlimited radio range scenario hold even when simulating the complete IEEE 802.11p protocol stack and under realistic transmission conditions.

### 6.3.5 Information Teleportation

As Theorem 6.9 shows, in a hyperfractal, the broadcasted packet can follow either a direct route or a diverted route. The diverted route case leads to the existence of new contagions on the lines of level  $H_c$  and  $H_d$ . This is what we call “information teleportation” phenomenon as the new contagions are not due to a source on lines  $H_c$  or  $H_d$  spreading its packet in a hop by hop manner but is due to routing the packets through intersections. The phenomenon will be visually illustrated by experiments in Section 5.5.

The teleportation phenomenon allows an acceleration of the broadcast time. Note that the acceleration itself is a self-similar phenomenon and takes places recursively: propagation on level  $H_i$  is accelerated by teleportation coming from lines  $H_{i+1}$ ,  $H_{i+2}$ ,  $H_{i+3}$  and so on. In a hyperfractal with teleportation effect, the broadcast time evolves as  $\mathcal{O}(n^{1-\delta})$  according to Corollary 6.11.

To consider a network with the absence of teleportation is to consider the direct route case in Theorem 6.9. In such a network, the broadcast time scales linearly with the number of hops,  $\mathcal{O}(nh)$ . The two regimes are illustrated in Figure 6.2a. The teleportation phenomenon arises after the linear characteristic overtakes the one for  $\mathcal{O}(n^{1-\delta})$ . Therefore, the inflexion point where teleportation arises verifies  $nh = An^{1-\delta}$ , where  $A$  is a constant. As the propagation on each of the lines depends on the speed of the nodes, fractal dimension and so on, the inflexion point will appear at a different moment in each scenario, and will be the turning point when the propagation delay on the direct route becomes higher than the propagation delay on the diverted route.

But this gives an insight only on the delay in propagating on the direct route versus the delay on propagating on the diverted route. However, we say that the teleportation effect speeds up the broadcast in the whole network. Let us look at an intuitive example

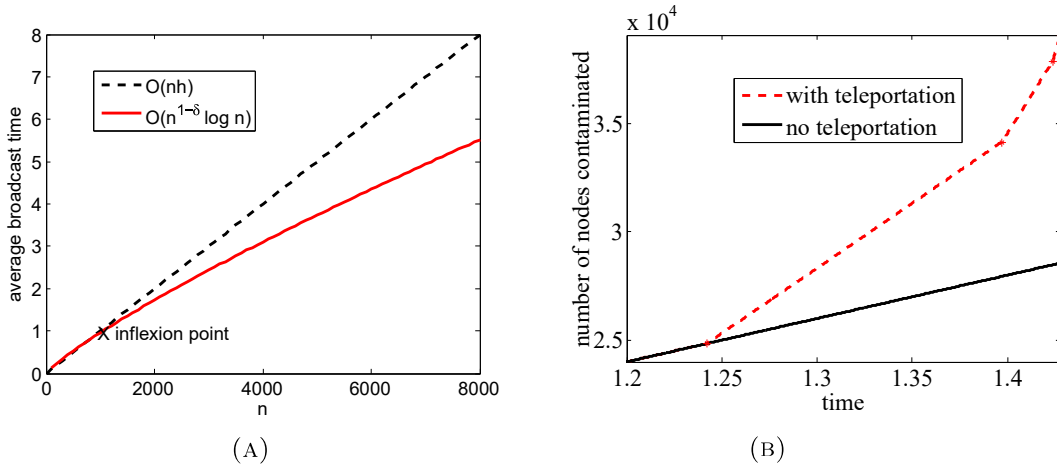


FIGURE 6.2: (A) Broadcast time evolution in hyperfractal vs linear regime: inflexion point. (B) Contagion propagation speed on the line of level 0.

of situation when the broadcast is accelerated due to information teleportation. In a hyperfractal setup, let us consider an infected source on a line of level  $H = 0$ . In each time slot  $h$ , two more nodes get infected and become themselves sources. In the absence of teleportation, therefore, the number of infected points increases linearly with the hop time. In the presence of intersections with lines of levels  $H_i > 0$ , new “outbreaks of infection” arise at time stamps of  $\frac{1}{vn(\lambda_0 + \lambda_{H_i})}$ .

Figure 6.2b shows graphically the evolution. This is an upper bound as not all the teleportation contagions generate a speed up; the nodes can be infected from neighboring contagions by simple hop by hop propagations. The teleportation phenomenon will be further debated in the Simulations Section, 5.5, where we will share our experiments and observations over the teleportation phenomenon.

## 6.4 Simulations in a System Level Simulator

### 6.4.1 QualNet Network Simulator Configuration

In order to evaluate the accuracy of our theoretical findings, we have performed simulations in QualNet Developer 6.1 [136], a commercial network simulator. QualNet is a system level simulator capable to mimic the performance of real networks. The available libraries implementing the standard specifications for different wireless and wired technologies provide the necessary tools for the simulation of complex communications

<b>Parameter</b>	<b>Setting</b>
Modulation and coding scheme	802.11 PHY specific MCS
Operating frequency	2.4GHz
Data rate	6Mbps
Transmission power	20dBm
Receiver sensitivity	-85dBm
Antenna type	Omnidirectional
MAC Protocol	802.11 MAC
Medium Access Technique	CSMA/CA
Association mode	Ad-hoc
Street length	1 Km
Environment type	urban
Application type	Constant Bit Rate (CBR)
Hop duration time (h)	60 ms

TABLE 6.1: PHY, MAC, application and environment parameters configuration in Qual-Net

networks. The simulator allows the design and configuration of protocols, network topologies, propagation environment and traffic applications and provides valuable insights regarding the behavior and performance of the simulated scenario.

For the evaluation of the theoretical quantities derived for the urban vehicular networks, the simulations follow IEEE 802.11p, the approved amendment to the IEEE 802.11 standard for wireless access in vehicular environments (WAVE), a vehicular communication system [137]. A custom configuration of the physical (PHY) and medium access control layer (MAC) layers allows the modeling of wireless networks implementing the IEEE 802.11p. Table 1 presents the main PHY, MAC and propagation parameters configured for the simulated scenarios.

#### 6.4.2 Urban Vehicular Environment Modeling and Scenario Description

An important step in the simulation is the design of the city map. As per the procedure described in Chapter 4, we can use the fractal dimension (computed from the input the average daily traffic flow measurement) to generate an equivalent simulated map of the city maps. The urban environment is replicated by means of a 3D map of a grid street plan, modeled using a three-level fractal geometry. We generate three levels in the hierarchy of streets (boulevards, streets, alleys) to set the urban street grid as illustrated in Figure 6.3.

As the buildings generate the canyon effect, the streets behave like a wave guide which is directly represented by the pathloss model set (urban model) and the propagation

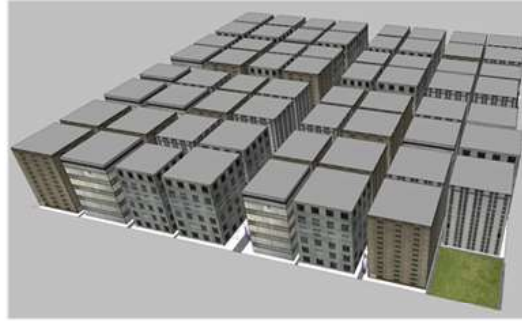


FIGURE 6.3: 3-D city map modeling in QualNet

environment (metropolitan). The width of the street decreases as the hyperfractal level increases, similarly to real cities, e.g., boulevards are wider than streets, which are, in turn, wider than alleys. For the first level the street width is approximately 60 meters, 30 meters for the second level, and 15 meters for the third level.

The simulation scenarios are created using the IEEE 802.11 library, integrating a variable number of nodes generated with a hyperfractal distribution, connected in a wireless ad-hoc network deployed in an urban environment (see Figure 6.4). In release 6.1, QualNet does not offer broadcast capabilities. In order to simulate a single-hop broadcast protocol (i.e. the information carried by one vehicle is transmitted to the other vehicles in its one-hop vicinity during the next broadcasting cycle), static hop-by-hop routing was configured in QualNet, ensuring that packets are forwarded from one node to the one in the immediate vicinity. This allows to observe the propagation of the packet along the direct route versus diverted route, as studied in Section 6.3.

We first validate the bounds claimed by Theorems 6.9 and 6.12 by observing the time necessary for a packet to propagate from one fixed source  $S$  to a fixed area of location, by selecting a destination node  $D$ . As such, there are two considered end-to-end paths between the source node  $S$  and the destination node  $D$ : the direct route (in Figure 6.4 in red) which follows the first-level streets (with a higher density of nodes), and an diverted route (in Figure 6.4 in green) which uses and third-level streets (less populated).

An important part of the end-to-end delay is the time spent in routing the packet through the intersection. As QualNet does not support delay-tolerant features, the routing through intersections is emulated by a temporary lack of available nodes in each intersection on the end-to-end paths in the evaluated scenarios. As such, additional nodes were added in intersection and were temporarily deactivated during the simulation. The crossed-out circles in Figure 6.4 emphasize the intersections where the nodes are deactivated and the additional queuing delays occur. The deactivation time (and implicitly the queuing delay) depends on the density of nodes on the streets and on their traveling speed.



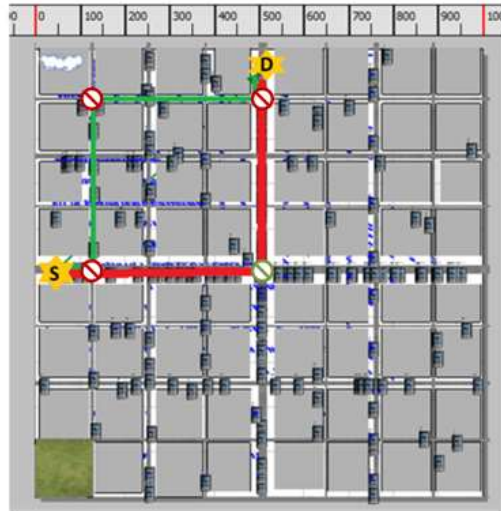


FIGURE 6.4: Direct (green) versus diverted (red) path between source and destination,  $d_F = 3$ ,  $n = 200$

### 6.4.3 Validation of Upper and Lower Bounds: Constant Speed

Several batches of simulations were run for three values of fractal dimension:  $d_F = 2.5$ ,  $d_F = 3$ , and  $d_F = 3.75$  with the number of nodes  $n$  ranging from  $n = 200$  up to  $n = 800$  nodes. The end-to-end delay on the considered paths is evaluated by using a Constant Bit Rate (CBR) application generating 100 packets of 512 bytes at every 5 seconds.

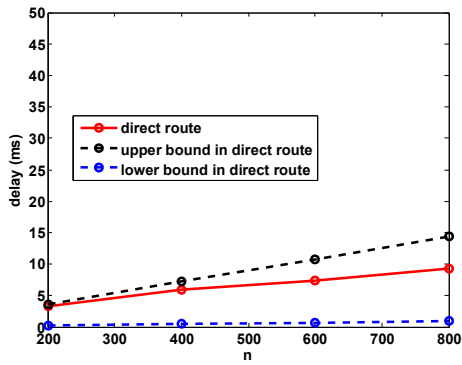
The formulations used for the upper bounds are the expression in equation (6.4) for the direct route and (6.5) for the diverted route respectively. For the lower bound the formulation used for validation through simulations is the closed expression  $T > hnL(x)$ .

Figures ?? (A), (B), (C) validate Theorems 6.9 and 6.12 on the expression of the average broadcast time for the direct path. The speed of the mobile nodes has been set to 40 kmph, as the typical legal speed limit in many cities. The upper bound is depicted in dash black, the lower bound in dash blue and the simulation results in continuous red line.

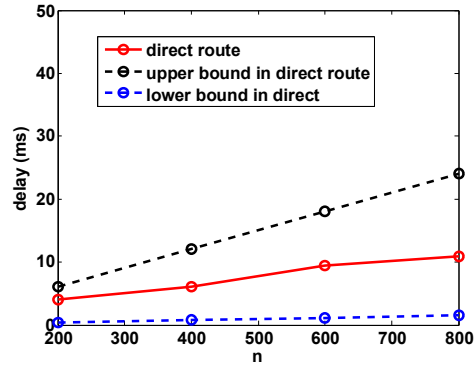
Figures ?? (D), (E), (F) validate Theorems 6.9 and 6.12 on the expression of the average broadcast time for the diverted path. Again, the speed of the mobile nodes has been set to the constant value of 40 kmph.

### 6.4.4 Validation of Bounds Under Speed Variation

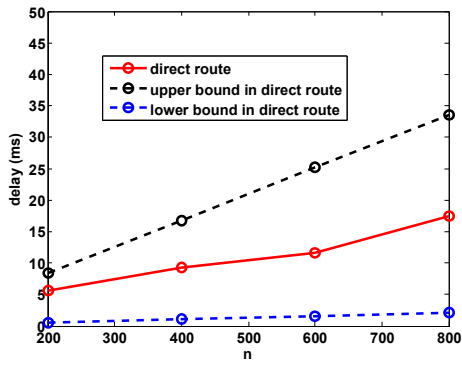
The theoretical results are developed under the assumption of constant speed throughout the whole network map, yet research has shown [62] that the speed is highly influenced by



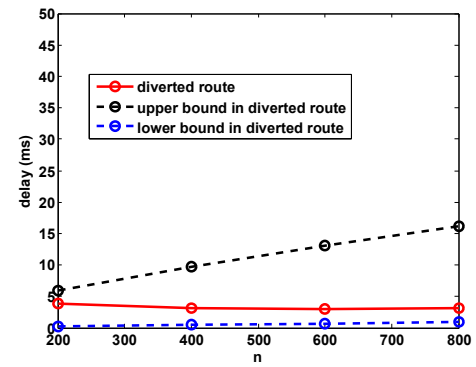
(A) direct route,  $d_F = 2.5$



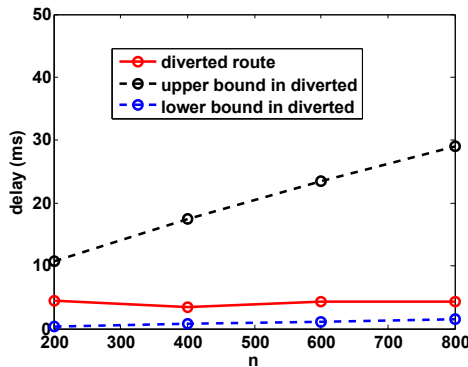
(B) direct route,  $d_F = 3$



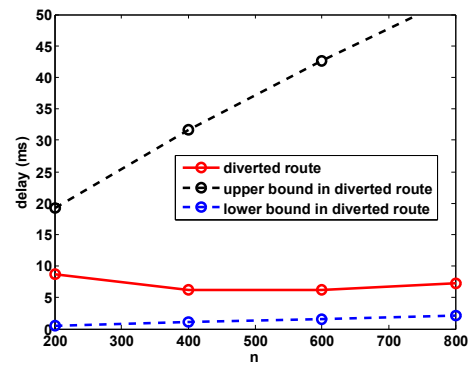
(C) direct route,  $d_F = 3.75$



(D) diverted route,  $d_F = 2.5$



(E) diverted route,  $d_F = 3$



(F) diverted route,  $d_F = 3.75$

FIGURE 6.5: Validation of bounds for direct route, constant speed, (A), (B), (C). Validation of bounds for diverted route, constant speed, (D), (E), (F)

the environment geometry. The following experiments show that the bounds introduced in Section 6.3 hold for the more realistic scenario of variable values of speed.

The first analysis looks at the case where the speed of the nodes is proportional to the level, i.e.,  $v \propto H$ . This models the scenario where the speed is lower on crowded streets, due to congestion, and increases with the decrease of density of nodes. Namely, the nodes on a level  $H_i$  have the same speed  $v_i \propto H_i$ . For each simulation scenario, the following vehicular mobility scenario is considered: the vehicles move with 20 kmph on the level 0 streets, 40 kmph on level 1 and 60 kmph on level 2, therefore the speed on the red route is 20 kmph and on the green route 60 kmph. Figure 6.6 validates the bounds, showing that our results extend to variable speed cases.

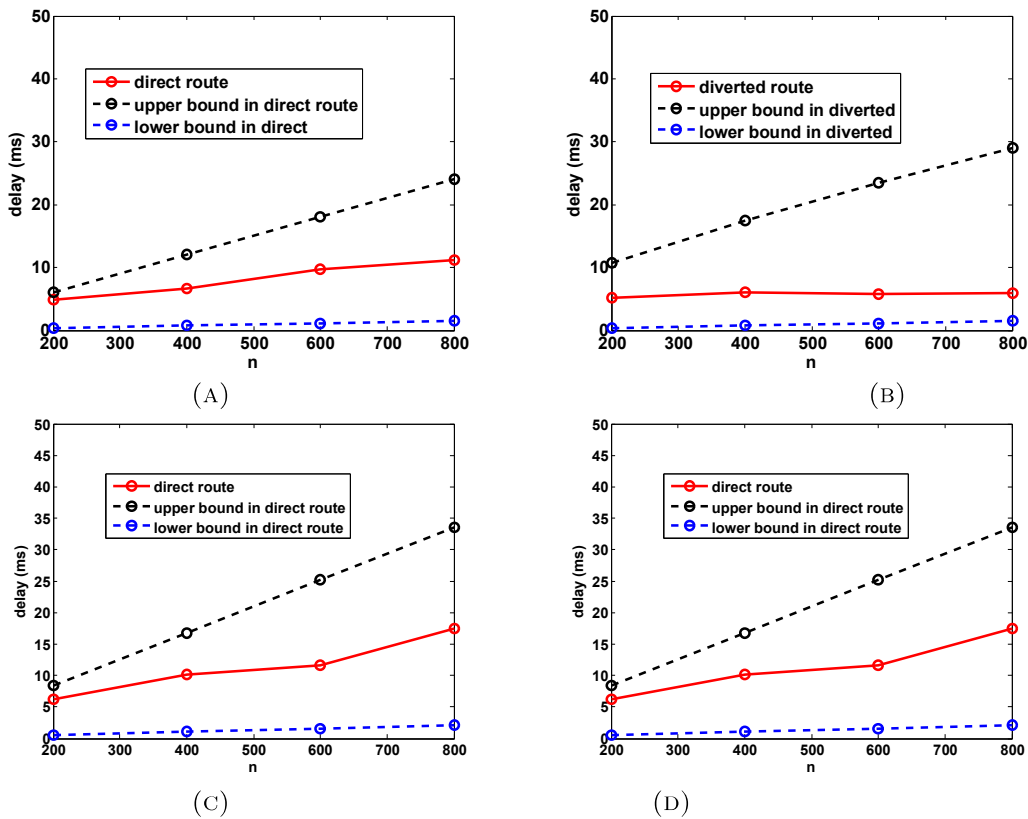


FIGURE 6.6: Validation of bounds for  $v$  increasing with level: a)  $d_F = 3$ , direct route, b)  $d_F = 3$ , diverted route, c)  $d_F = 3.75$ , direct route, d)  $d_F = 3.75$ , diverted route

The second analysis looks at the case where the speed is proportional to the inverse of the level,  $v = \frac{1}{H}$ . This models the scenario where streets with a high level of importance in the city offer greater speed, like highways, but decreases with the street importance, for example, alleys. For each simulation scenario, the following vehicular mobility scenario is considered: the vehicles move with 60 kmph on the level 0 streets, 40 kmph on level 1 and 20 kmph on level 2, therefore the speed on the red route is 60 kmph and on the

green route 20 kmph. Figure 6.7 validates our bounds for this scenarios of variable speed as well. All the plots have been done for  $\epsilon = 0.1$ .

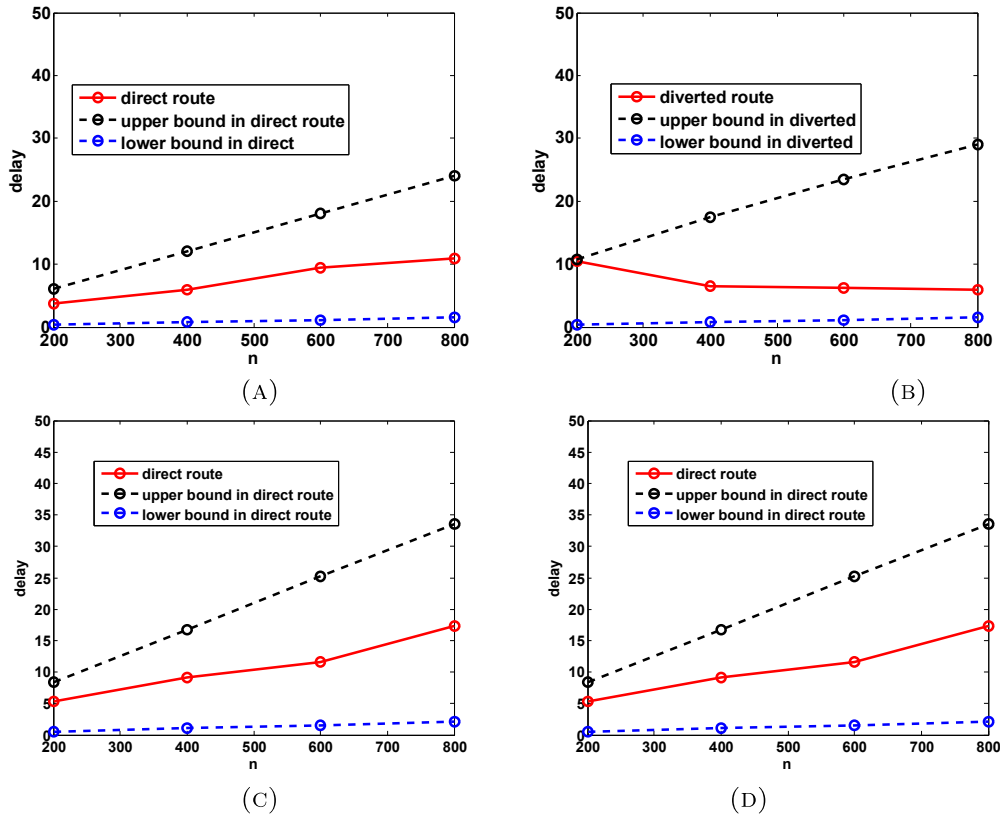


FIGURE 6.7: Validation of bounds for  $v$  decreasing with level: a)  $d_F = 3$ , direct route, b)  $d_F = 3$ , diverted route, c)  $d_F = 3.75$ , direct route, d)  $d_F = 3.75$ , diverted route

## 6.5 Simulations in a Self-Developped Discrete Time Event-Based Simulator

As QualNet does not allow simulating a full epidemic broadcast, we developed a discrete time event-driven simulator in Matlab which follows the model presented in Section 6.2 in order to observe specific phenomenons that arrive when broadcasting a packet in a hyperfractal.

The map length is the unit and a scaling is performed in order to respect the scaling of real cities as well as communication and motion parameters. In that sense, it is considered that the unit represents 10 kms of distance in a real scale. Respecting this scaling, the value of speed in the simulations is  $v = 10^{-3}$ . The hop duration is chosen as  $= 1ms$ .

Throughout the simulations, the depth of the hyperfractal are restricted to  $H = 5$ .

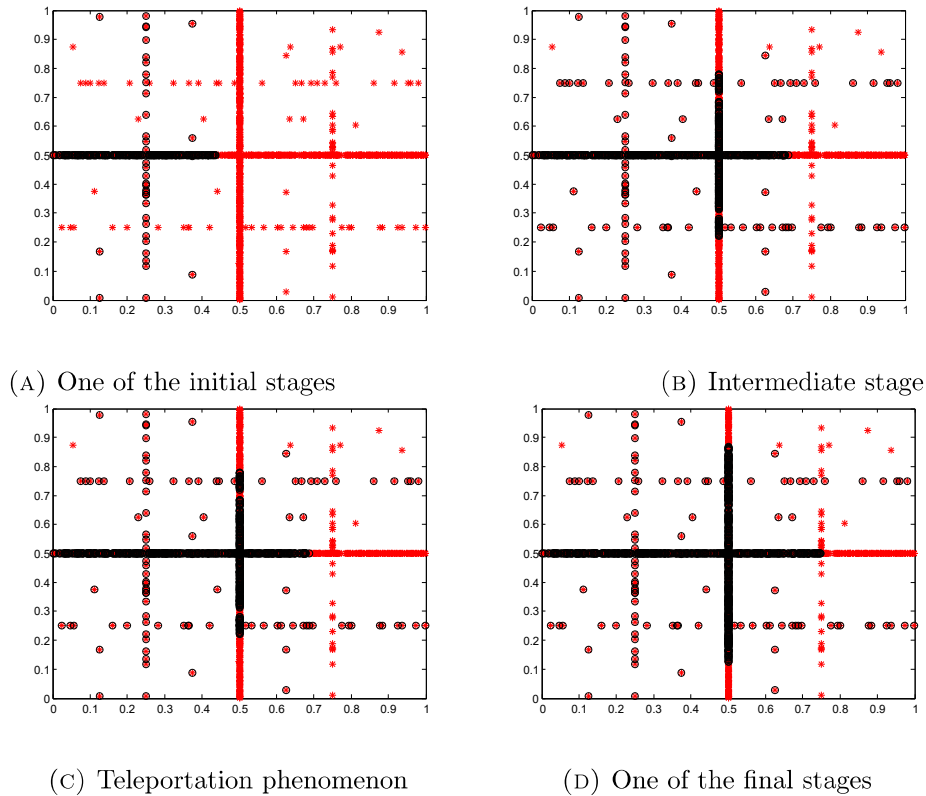


FIGURE 6.8: Snapshots of information dissemination in a Hyperfractal, healthy nodes in red ‘\*’, infected nodes in black ‘o’

### 6.5.1 Information Spread Under Hyperfractal Model and Teleportation Phenomenon

We first study information propagation in a full idealized epidemic broadcast with its specific phenomena. In a two dimensional uniform Poisson point process, the information packet spreads uniformly as a full disk that grows at a constant rate, which coincides with the information propagation speed, as shown in [37].

Interestingly, in a hyperfractal, the phenomenon is completely different, as a consequence of the canyon effect and the population distribution specific to the new model.

The simulations are performed using the following scenario: a source starts an epidemic broadcast of an information packet at time  $t = 0$  in a network of 1,200 nodes in a 1x1 unit square, mobile node speed  $v = 10^{-3}$ , packet transmission time, also called hop time is  $h = 10^{-3}$ . The population of 1,200 nodes is distributed in the map according to a hyperfractal of dimension  $d_F = 5.33$ .

Figure 6.8 shows different stages in the information propagation starting from a random chosen source until the complete contamination of the nodes.

As one can notice, the information propagation is highly influenced by geometry of the network and does not happen in a uniform way, but it strongly influenced by the distribution of the population and the constraints imposed by the environment (canyon effect, intersections).

Let us now illustrate the propagation phenomenon that arises as a consequence of the hyperfractal distribution of nodes and the broadcast algorithm. Figure 6.8c shows “the teleportation phenomenon” in a network of  $n = 1,200$  nodes with  $d_F = 5.33$ . Two contagions of infected nodes on the lines of level 0 are highlighted. These areas are not connected to the main infected area on the line on which they originate, the line of level  $H = 0$ . The nodes on these areas are infected by receiving the packet from nodes traveling on perpendicular lines. This generates several areas of contagion. On this line, the packet is spread from all of the contamination sources that have arisen and thus the broadcast is sped up. This is a phenomenon that uniquely characterizes the broadcast in hyperfractal setups.

### 6.5.2 Validation of Upper and Lower Bounds on the Average Broadcast Time in the Entire Network

In the previous section, using the simulations done in QualNet, we validated the bounds for the broadcast time in the direct route and in the indirect route. Now, the developed simulator, we can validate the bounds for the average broadcast time for a complete contamination of the network. The self-developed simulator allows for choosing larger values of  $n$ .

The experiments are run for numerous values of  $n$  starting with  $n = 300$  and then from  $n = 500$  up to 5,000 nodes with a step of 500 and  $d_F = 3$  and  $d_F = 5.33$ , thus  $p = 0.5$ , and 0.9 respectively.

The formulation used for the upper bound is the expression in equation (6.2), while for the lower bound the formulation used for validation through simulations is the closed expression  $T > hnL(x)$  with  $L(x) = \frac{1}{B_n}$  and  $B_n = \frac{n^\delta \Gamma(\delta) \left(\frac{x}{2}\right)^\delta}{\log(2/q)}$ .

Figure 6.9a validates Theorems 6.5 and 6.12 on the expression of the average broadcast time.

Notice that the lower bound follows with a good approximation the simulation results. Each of the cases shows that the broadcast time increases with the decrease of the number of points, a phenomenon which is captured successfully by the upper bound. The upper

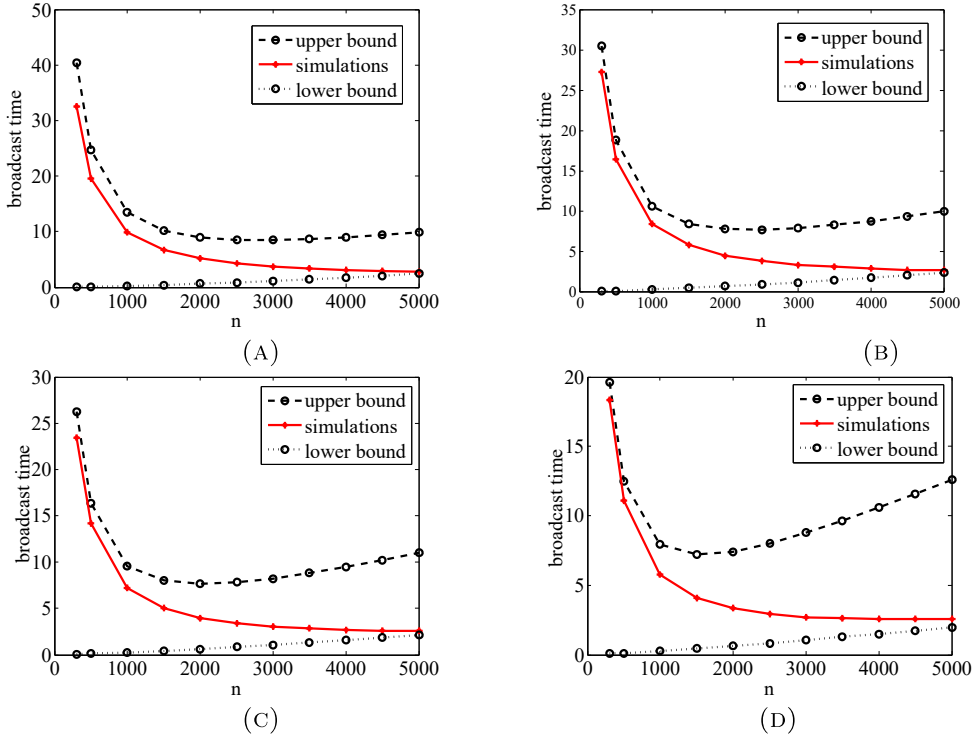


FIGURE 6.9: Broadcast time: simulation vs. theoretical results for (a)  $d_F = 3$ , (b)  $d_F = 3.33$ , (c)  $d_F = 3.75$ , (d)  $d_F = 5.33$

bound increases with a higher slope for big fractal dimension (see Figure 6.9d), converging towards the asymptotic bound of  $\mathcal{O}(n^{1-\delta} \log n)$ .

### 6.5.3 Validation of Bounds on Average Broadcast Time Under Speed Variation

Again, we shall prove that the bounds developed under the constant speed assumption hold when the speed varies with the level.

The first analysis looks at the case where the speed of the nodes is proportional to the level,  $v \propto H$ , the nodes on a level  $H_i$  have the same speed  $v_i \propto H_i$ .

The values of speed are chosen such as to represent, in real-setup,  $v = 36$  kmph for  $H = 0$ ,  $v = 40$  kmph for  $H = 1$ ,  $v = 50$  kmph for  $H = 2$ ,  $v = 60$  kmph for  $H = 3$  and  $v = 70$  kmph for  $H = 4$ . Results obtained in two setups with different fractal dimension are displayed in Figure 6.10 and validate both upper and lower bound on the broadcast time. The second analysis looks at the case where the speed is proportional to the inverse of the level,  $v = \frac{1}{H}$ . For this case, the values of speed are chosen to correspond to real-setup

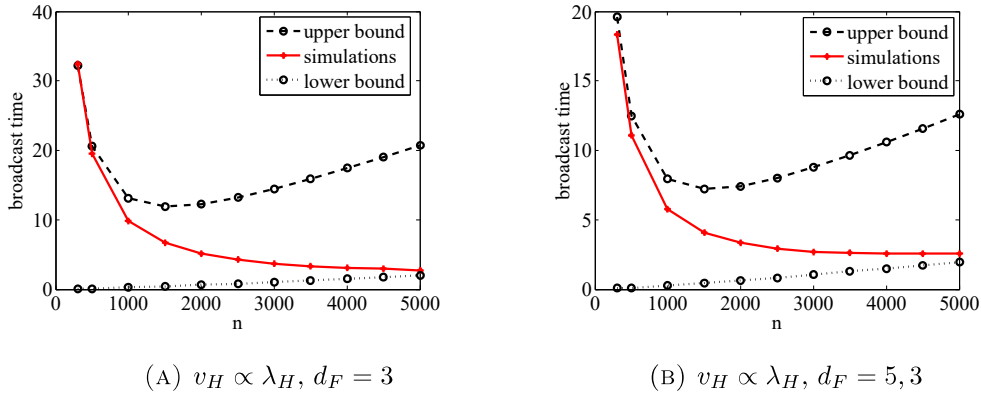


FIGURE 6.10: Speed proportional to the level

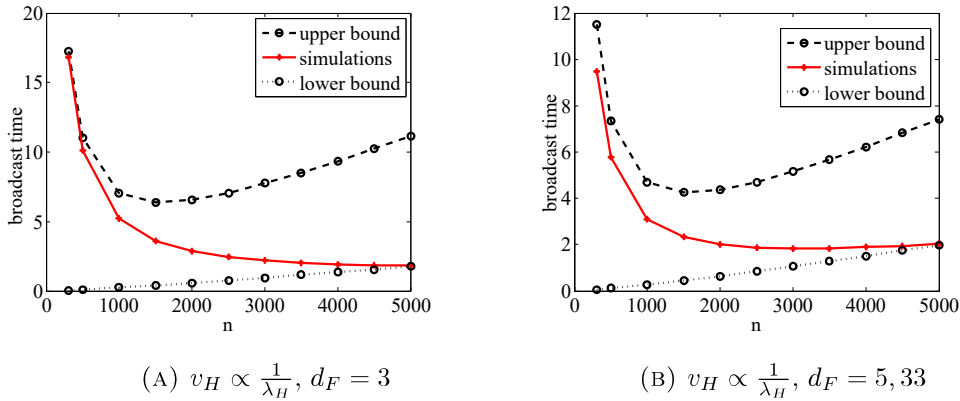


FIGURE 6.11: Speed inversely proportional to the level

values of:  $v = 36$  kmph for  $H = 4$ ,  $v = 40$  kmph for  $H = 3$ ,  $v = 50$  kmph for  $H = 2$ ,  $v = 60$  kmph for  $H = 1$  and  $v = 70$  kmph for  $H = 0$ .

Results obtained in two setups with different fractal dimensions are displayed in Figure 6.11 and validate both upper and lower bound on the broadcast time.

The figures might give the impression that the simulated average broadcast time characteristic is increasing in  $n$ . Let us remind that the simulations are restricted to  $H = 5$  levels, which eliminates a substantial number of nodes.

## 6.6 Concluding Remarks

In this chapter, we addressed another application specific to ad-hoc networks, information dissemination, under the hyperfractal model. This study provided an extended characterization of the information propagation speed of vehicular delay tolerant mobile networks



in urban scenario by exploiting the hyperfractal model nodes for the topology of the network and mobile vehicle locations. We have provided theoretical matching upper and lower bounds for such networks. These theoretical bounds are useful in order to increase our understanding of the fundamental properties and performance limits of vehicular networks in urban environments, as well as to evaluate and optimize the performance of specific routing algorithms.

Furthermore, we have shown an information propagation phenomenon specific to a hyperfractal setup: the information teleportation phenomenon, that allows for the acceleration of the broadcast.

The findings have been validated by extensive simulations performed in a self-developed simulator as well as simulations performed in a commercial network simulator. This has shown that the results remain valid for a full-stack implementation of devices and under realistic propagation phenomenons.

This study was a proof that the hyperfractal model for nodes is suited for the analysis of the delay-tolerant networks in urban environment.

## Chapter 7

# Conclusion and Future Work

### 7.1 Conclusion

This thesis proposed a novel model for the representation of the density of devices communicating in urban environment like networks of cars and IoT devices by merging stochastic geometry with self-similarity. We have shown how the model can be handled in order to compute metrics of interest in wireless networks and improve the performance. More specific, the **contributions** of this work are as follows.

A new model called “hyperfractal” has been proposed and introduced. The model exists in two options: for representing the decaying density of nodes with the increase of length of the streets and for representing the placement of road-side infrastructure by using the same observation, the decrease of mobile nodes density with the length of streets.

The model has been defined, described and basic properties such as connectivity were studied. Some typical tools such as the Campbell-Mecke formula have been developed that allow the manipulation of the model withing classic stochastic geometry framework.

For the hyperfractal model for nodes on lines, the authors have developed a procedure of computing the fractal dimension of cities and areas, as a key feature of a hyperfractal, when public traces are available. Furthermore, this procedure comprises several criteria for validation that allow an increased flexibility in the application of the model to traces. This procedure has been showcased during Nokia 5G Campus event.

The ease of use and capabilities of the hyperfractal model have been showcased by the study of two wireless communication scenarios. One of the applications advocated for the use of the model when using millimeter wave technology. In this first study, we showed

how metrics like end-to-end transmission energy and routing delay can be evaluated with by exploiting a hyperfractal setup. Some considerations on capacity and load balancing were also provided. In the second application, the focus was on a infrastructure-less communication scenario. More precisely, we evaluated the broadcast time in a network of cars. During this study, we discovered the “teleportation” phenomenon that is a characteristic of the hyperfractal setup and that allows for a speed-up of the network contamination.

## 7.2 Future Work

The hyperfractal model is very promising therefore possible directions of further work are vast. Some of the directions can be the following.

There is a necessity for a procedure of validation with traces of the hyperfractal model with relays. Up until now, the lack of publicly available data has made this difficult. The procedure should be similar to the procedure of validation of the model for mobile nodes, several criteria should be provided.

Hyperfractals can be a good fit for millimeter wave urban communications modeling, as the propagation model fits well the limitations experienced in millimeter frequency bands. In this direction, we believe a research subject could be evaluating the load and performances achievable when using millimeter wave based infrastructure. The model can also be extended to a three dimensional embedding space for the study of communications in networks of drones deploying millimeter wave technology or beam-forming if operating in LTE frequency bands.

An idea that the authors would have liked to explore is the iterated hybrid hyperfractals. We call them “hybrid” as the idea is to choose a different  $p$  for each of the quadrants or, a different option would be to choose a different  $p$  for each level, preserving the stationarity in depth but not the self-similarity. Other iterated options can be imagined, yet the focus should be on models that help us imitate even more the reality and capture the features of the desired communication scenario.

The exploration of equivalent stochastic geometric models, like Poisson points on Poisson line tessellations that would inherit the property of self-similarity and the laws of scaling has generated stimulating ideas, one of which lead to the concept of percolation in depth.

### 7.2.1 Generalization of the Model for Nodes

In their extensive work, the authors of [138] have shown that telecommunications networks follow road networks and these can be fitted successfully to Poisson line tessellations, Poisson Voronoi tessellations and Poisson Delauney tessellations. Furthermore, the authors have provided methods for computing the intensity of the underlying point process of each of these tessellations.

For future work, we envisage the generalization of the support to Poisson line tessellations, the generalization of process  $\Phi$  to a process of Poisson points on Poisson lines and the generalization of processes  $\Phi^r$  and  $\Xi$  to processes obtained in the intersections of the generalization of process  $\mathcal{X}$ . This will lead to the creation of models that should relax the constraints of the hyperfractal models, in particular, the constraints on splitting the structure in quadrants and the extension constraint generated by the limited window. The generalized models should preserve the scaling of length of the support with the level and the scaling of the density of points (either on lines, either on intersections of lines) with the level specific to the hyperfractal models.

In contrast to the hyperfractal models, the equivalent generalized models will be stationary and isotropic, which are good properties that will further simplify the manipulation of the models. This opens the path for the development of further results that will combine the benefits of the good properties of the generalized models as well as the laws of scaling of the hyperfractal models. On the other hand, the generalized models will no longer display the self-similarity by splitting in quadrants nor their intensity measure is expected to be fractal.

The procedure of computation of the fractal dimension of traffic density maps of cities presented earlier in this manuscript relies solely on these laws of scaling with the depth. A further extension of this procedure is by taking in account the statistics of intersections of the structure of level  $i$  with the support structure of level  $i - 1$ . This again, is a feature that is expected to be preserved in the generalized model.

Let us now give several ideas about these further developments.

### 7.2.2 Generalization to Poisson Points on Poisson Lines

It is natural that a first generalization to be done is by finding the equivalent model in terms of Poisson points on Poisson lines. Observe that the hyperfractal has the following growth of length. Define by  $l_0$  the length of the support  $\mathcal{X}_0$  at level 0. At level 1, the

length of  $\mathcal{X}_0$  is  $l_1 = 2l_0$ , then  $l_2 = 4l_0, \dots, l_n = 2^n l_0$ . Therefore at a level  $n$ , the mean length is  $l_n = C^n l_0$  with  $C > 1$ . The density per level has a growth as  $\lambda_n = \frac{p(1-p)^n \lambda}{C^n l_0}$ .

Given these observations, the procedure of obtaining the process of Poisson points on Poisson lines equivalent to a hyperfractal has the following steps:

- i) Build the line process in order to respect the same mean length per unit window;
- ii) Assign the Poisson points in order to keep the same density per level.

We denote by  $\Xi^*$  the support structure made of Poisson lines, at each level,  $\Xi^*$  has the density  $\lambda_n^{\Xi^*}$ . Denote by  $\Omega$  the obtained process of Poisson points on Poisson lines.

By its construction, the process is stationary, isotropic, uniform. The location of the *typical point*  $\omega^0$  is found by choosing the level of the Poisson tessellation with a geometric random variable and adding the line in the origin. With uniform probability  $p$ , a point is placed in the origin. The *Laplace transform* of interference for Poisson line process has been studied in [139] and can be extended for the obtained process. In which regards the *Campbell-Mecke* formula, we remind that this equivalent process is stationary, therefore one can make use of the Campbell-Mecke formula for stationary point processes as follows:

$$\mathbf{E} \left[ \sum_{\omega_i \in \Omega} f(\omega_i, \phi) \right] = \Lambda \mathbf{E} [f(\omega^0, \Omega \cup \{\omega^0\})]$$

The complete development of the generalization remains for future work.

### 7.2.3 Generalization to Poisson Voronoi Tessellations

The generalization to Poisson Voronoi tessellations can be done either as a generalization to iterated Poisson Voronoi tessellations, or as generalization to independent Poisson Voronoi tessellations. In both cases, the algorithm for obtaining the equivalent tessellation in a finite window is as follows:

- i) Given  $p$ , find the density  $v_h$  at each level of the Poisson point process of the equivalent Voronoi tessellation;
- ii) Build the tessellations at each depth in order to respect the mean length of lines in the window;
- iii) Assign Poisson points to the lines while keeping the same density of population within level.

Let us further give some hints for the generalization to independent Poisson Voronoi tessellations. We denote by  $\Xi^{**}$  the support structure made of Voronoi cells, at each level,  $\Xi^{**}$  is generated by an underlying Poisson point process with density  $v_h = 2^h$ . Denote by  $\Omega^{**}$  the obtained process of Poisson points on Poisson lines. The point process on the support has the intensity  $\lambda_h^{\Omega^{**}} = p(1-p)^h$  and on each of the lines the density is  $p(1-p)^h/2^h$ .

Again here, the obtained process, by its construction, is stationary, isotropic, uniform.

### 7.2.4 In-Depth Percolation for a Finite Window

While trying to imagine the extension of the hyperfractal model to the equivalent models, the following questions came to our mind: if we limit the window of analysis, for the growth of  $\lambda$  (number of Poisson points) and  $\rho$ , how does the giant component scale? What about if we allow for a logarithmic growth of the window?

When laying in a limited window, for  $n \rightarrow \infty$ , there will exist a finite number of lines in a layer and we will always be able to find a level sufficiently deep such that there is a line that connects to the lines of the first level. Secondly, when  $n \rightarrow \infty$ , there is an increasing probability that there is a line that holds a point and has a relay at the intersection with the lines of the first level.

This concept of connectivity in this finite window of analysis but with a depth going to infinity, we call it as “percolation in depth”. The questions look rather interesting, in particular for the stochastic geometry community.

# Appendix A

## Proofs

Proof of Lemma 6.1

**Lemma A.1.** *The average number of busy streets is asymptotically equivalent to  $n^\delta \frac{\Gamma(-\delta)}{\log(2/q)}$  with  $\delta = \frac{\log 2}{\log(2/q)}$  and where  $\Gamma(\cdot)$  is the Euler “Gamma” function.*

*Proof of Lemma 6.1.* Let us denote by  $B_n$  be the average number of busy streets. The probability that a street of level  $H$  is busy is  $1 - (1 - \lambda_H)^n$ . Therefore

$$B_n = 2 \sum_{H \geq 0} 2^H (1 - (1 - \lambda_H)^n).$$

We introduce the Poisson generating function  $B(z) = \sum_n B_n \frac{z^n}{n!} e^{-z}$ . It is named after Poisson as it is equivalent into considering that the number of nodes  $n$  is random and follows a Poisson law of parameter  $z$ . The reason behind introducing this function is that it facilitates the manipulation and the asymptotics of its coefficient is given by the general depoissonization theorems [140]. One has:

$$B(z) = 2 \sum_H 2^H (1 - e^{-\lambda_H z}).$$

The Mellin transform  $B^*(s) = \int_0^\infty B(z) z^{s-1} dz = 2 \frac{(p/2)^{-s}}{1 - 2(q/2)^{-s}} \Gamma(s)$  is defined for  $-1 < \Re(s) < 0$  and has simple poles at  $s = -\delta + \frac{2ik\pi}{\log(q/2)}$  with  $k \in \mathbb{Z}$ . Applying the results of

[140] the estimate  $B_n = O(n^\delta)$  is obtained. More precisely for all  $M > 0$

$$\begin{aligned} B_n &= \frac{n^\delta}{\log(2/q)} \sum_{k \in \mathbb{Z}} n^{2ik\pi/\log(2/q)} \Gamma(-\delta + 2ik\pi/\log(2/q)) \\ &\quad + (n^{-M}) \\ &= \frac{n^\delta}{\log(2/q)} (\Gamma(-\delta) + O(\Gamma(-\delta + 2ik\pi/\log(2/q)))) \end{aligned}$$

The main asymptotic term is  $B_n = n^\delta \frac{\Gamma(-\delta)}{\log(2/q)}$  the other contributions are negligible due to the exponential decrease of function Gamma on the imaginary axis.  $\square$



# Bibliography

- [1] Michael Batty and Paul Longley. *Fractal Cities: A Geometry of Form and Function*. Academic Press Professional, Inc., San Diego, CA, USA, 1994. ISBN 0-12-455570-5.
- [2] Michael Barnsley. *Fractals Everywhere*. Academic Press Professional, Inc., San Diego, CA, USA, 1988. ISBN 0-12-079062-9.
- [3] M. Karabacak and all. Mobility performance of macrocell-assisted small cells in manhattan model. In *VTC*, May 2014. doi: 10.1109/VTCSpring.2014.7022987.
- [4] B. B. Mandelbrot. *The Fractal Geometry of Nature*. W. H. Freeman, 1983.
- [5] Wikipedia contributors. Industry 4.0 — Wikipedia, the free encyclopedia, 2018. URL [https://en.wikipedia.org/w/index.php?title=Industry\\_4.0&oldid=854860300](https://en.wikipedia.org/w/index.php?title=Industry_4.0&oldid=854860300). [Online; accessed 16-August-2018].
- [6] Wikipedia contributors. Vehicular communication systems — Wikipedia, the free encyclopedia, 2018. URL [https://en.wikipedia.org/w/index.php?title=Vehicular\\_communication\\_systems&oldid=851981434](https://en.wikipedia.org/w/index.php?title=Vehicular_communication_systems&oldid=851981434). [Online; accessed 16-August-2018].
- [7] Nokia about IoT, howpublished = [https://www.nokia.com/en\\_int/about-us/what-we-do/internet-of-things](https://www.nokia.com/en_int/about-us/what-we-do/internet-of-things).
- [8] Christopher Watson. Trends in world urbanisation. *Proceedings of the First International Conference on Urban Pest*, 1993.
- [9] Wikipedia contributors. Urbanization — Wikipedia, the free encyclopedia, 2018. URL <https://en.wikipedia.org/w/index.php?title=Urbanization&oldid=857901183>. [Online; accessed 11-September-2018].
- [10] Nokia. Use case: Safer and efficient highway ready for future mobility, 2018. URL <https://networks.nokia.com/use-case/highways/C-V2X-communications>. [Online; accessed 16-August-2018].

- 
- [11] Andreas Festag. Standards for vehicular communication—from IEEE 802.11p to 5G. *e & i Elektrotechnik und Informationstechnik*, 132(7):409–416, Nov 2015. ISSN 1613-7620.
- [12] What is vehicle to infrastructure? <http://http://whatis.techtarget.com/definition/vehicle-to-infrastructure-V2I-or-V2X>.
- [13] Wikipedia contributors. Stochastic geometry models of wireless networks — Wikipedia, the free encyclopedia, 2018. URL [https://en.wikipedia.org/w/index.php?title=Stochastic\\_geometry\\_models\\_of\\_wireless\\_networks&oldid=842560914](https://en.wikipedia.org/w/index.php?title=Stochastic_geometry_models_of_wireless_networks&oldid=842560914). [Online; accessed 12-June-2018].
- [14] E. Gilbert. Random plane networks. *Journal of the Society for Industrial and Applied Mathematics*, 9(4):533–543, 1961.
- [15] L. Kleinrock and J. Silvester. Optimum transmission radii for packet radio networks or why six is a magic number. In *Conference Record, National Telecommunications Conference*, pages 4.3.1–4.3.5, Birmingham, Alabama, December 1978.
- [16] L. Kleinrock and J. Silvester. Spatial reuse in multihop packet radio networks. *Proceedings of the IEEE*, 75(1):156–167, 1987.
- [17] François Baccelli and Bartłomiej Błaszczyszyn. *Stochastic Geometry and Wireless Networks, Volume I - Theory*. Foundations and Trends in Networking Vol. 3: No 3-4, pp 249-449. NoW Publishers, .
- [18] F. Baccelli, B. Błaszczyszyn, and P. Muhlethaler. On the performance of time-space opportunistic routing in multihop mobile ad hoc networks. In *2008 6th Int. Symp. on Modeling and Optimization in Mob., Ad Hoc, and Wireless Networks (WiOpt)*, 2008.
- [19] Wikipedia contributors. Signal-to-interference-plus-noise ratio — Wikipedia, the free encyclopedia, 2016. URL [https://en.wikipedia.org/w/index.php?title=Signal-to-interference-plus-noise\\_ratio&oldid=757256852](https://en.wikipedia.org/w/index.php?title=Signal-to-interference-plus-noise_ratio&oldid=757256852). [Online; accessed 18-September-2018].
- [20] Wikipedia contributors. Shot noise — Wikipedia, the free encyclopedia, 2018. URL [https://en.wikipedia.org/w/index.php?title=Shot\\_noise&oldid=858002041](https://en.wikipedia.org/w/index.php?title=Shot_noise&oldid=858002041). [Online; accessed 18-September-2018].
- [21] Wikipedia contributors. Campbell’s theorem (probability) — Wikipedia, the free encyclopedia, 2018. URL <https://en.wikipedia.org/w/index.php?title=>

- [Campbell%27s\\_theorem\\_\(probability\)&oldid=851514722](#). [Online; accessed 4-September-2018].
- [22] M. Zorzi and S. Pupolin. Outage probability in multiple access packet radio networks in the presence of fading. *IEEE Transactions on Vehicular Technology*, 43(3):604–610, 1994.
- [23] François Baccelli and Bartłomiej Błaszczyszyn. On a Coverage Process Ranging from the Boolean Model to the Poisson Voronoi Tessellation With Applications to Wireless Communications. Technical Report RR-4019, INRIA, October 2000. URL <https://hal.inria.fr/inria-00072622>. Projet MCR.
- [24] Bartłomiej Błaszczyszyn, Martin Haenggi, Paul Keeler, and Sayandev Mukherjee. *Stochastic Geometry Analysis of Cellular Networks*. Cambridge University Press, 2018.
- [25] François Baccelli and Bartłomiej Błaszczyszyn. *Stochastic Geometry and Wireless Networks, Volume I - Theory*. Foundations and Trends in Networking Vol.3. .
- [26] Bartłomiej Błaszczyszyn. Lecture Notes on Random Geometric Models — Random Graphs, Point Processes and Stochastic Geometry. Lecture, December 2017. URL <https://hal.inria.fr/cel-01654766>.
- [27] David Aldous and Russell Lyons. Processes on unimodular random networks. *Electronic Journal of Probability*, 12:1454–1508, 2007.
- [28] Catherine Gloaguen and Elie Cali. Cost estimation of a fixed network deployment over an urban territory. *Annals of Telecommunications*, Nov 2017.
- [29] P. Gupta and P. R. Kumar. The capacity of wireless networks. *IEEE Transactions Information Theory*, pages 388–404, 2006. ISSN 0018-9448. doi: 10.1109/18.825799.
- [30] B. Błaszczyszyn and P. Muhlethaler. Random linear multihop relaying in a general field of interferers using spatial aloha. *IEEE Transactions on Wireless Communications*, July 2015. ISSN 1536-1276. doi: 10.1109/TWC.2015.2409845.
- [31] Z. Tong, H. Lu, M. Haenggi, and C. Poellabauer. A stochastic geometry approach to the modeling of dsrc for vehicular safety communication. *IEEE Transactions on Intelligent Transportation Systems*, May 2016. ISSN 1524-9050.
- [32] M. Haenggi, J. G. Andrews, F. Baccelli, O. Dousse, and M. Franceschetti. Stochastic geometry and random graphs for the analysis and design of wireless networks. *IEEE Journal on Selected Areas in Communications*, 27(7):1029–1046, 2009.

- 
- [33] A. Guo and M. Haenggi. Spatial stochastic models and metrics for the structure of base stations in cellular networks. *IEEE Transactions on Wireless Communications*, 12(11):5800–5812, 2013.
- [34] M. Haenggi. Mean interference in hard-core wireless networks. *IEEE Communications Letters*, 15(8):792–794, 2011.
- [35] H. S. Dhillon, R. K. Ganti, F. Baccelli, and J. G. Andrews. Modeling and analysis of k-tier downlink heterogeneous cellular networks. *IEEE Journal on Selected Areas in Communications*, 30(3):550–560, April 2012. ISSN 0733-8716. doi: 10.1109/JSAC.2012.120405.
- [36] H. El Sawy, E. Hossain, and M. Haenggi. Stochastic geometry for modeling, analysis, and design of multi-tier and cognitive cellular wireless networks: A survey. *IEEE Communications Surveys Tutorials*, 15(3):996–1019, 2013.
- [37] Philippe Jacquet, Bernard Mans, and Georgios Rodolakis. Information propagation speed in mobile and delay tolerant networks. *IEEE Transactions on Information Theory*, 56(10):5001–5015, October 2010. ISSN 0018-9448.
- [38] T. Spyropoulos, K. Psounis, and C. S. Raghavendra. Efficient routing in intermittently connected mobile networks: The single-copy case. *IEEE/ACM Transactions on Networking*, 16, 2008.
- [39] H. P. Keeler and B. Błaszczyszyn. SINR in wireless networks and the two-parameter poisson-dirichlet process. *IEEE Wireless Communications Letters*, 3(5):525–528, 2014.
- [40] M. Di Renzo. Stochastic geometry modeling and analysis of multi-tier millimeter wave cellular networks. *IEEE Transactions on Wireless Communications*, 14(9):5038–5057, 2015.
- [41] N. Deng, W. Zhou, and M. Haenggi. The Ginibre Point Process as a model for wireless networks with repulsion. *IEEE Transactions on Wireless Communications*, 14(1):107–121, 2015.
- [42] B. Błaszczyszyn, P. Muhlethaler, and N. Achir. Vehicular ad-hoc networks using slotted aloha: Point-to-point, emergency and broadcast communications. In *2012 IFIP Wireless Days*, pages 1–6, 2012.
- [43] Barłomiej Błaszczyszyn, Paul Mühlethaler, and Yasser Toor. Stochastic analysis of aloha in vehicular ad hoc networks. *Annals of telecommunications - annales des télécommunications*, 68(1):95–106, Feb 2013. ISSN 1958-9395.

- 
- [44] B. Blaszczyszyn, P. Mühlethaler, and Y. Toor. Maximizing throughput of linear vehicular ad-hoc networks (vanets) — a stochastic approach. In *2009 European Wireless Conference*, pages 32–36, 2009.
- [45] Chang-Sik Choi and François Baccelli. Poisson cox point processes for vehicular networks. *CoRR*, abs/1801.04556, 2018.
- [46] E. Steinmetz, M. Wildemeersch, T. Q. S. Quek, and H. Wymeersch. A stochastic geometry model for vehicular communication near intersections. In *2015 IEEE Globecom Workshops (GC Wkshps)*, pages 1–6, 2015.
- [47] Q. Cui, N. Wang, and M. Haenggi. Spatial point process modeling of vehicles in large and small cities. In *GLOBECOM 2017 - 2017 IEEE Global Communications Conference*, pages 1–7, 2017.
- [48] X. Tian, J. Yu, L. Ma, G. Li, and X. Cheng. Distributed deterministic broadcasting algorithms under the sinr model. In *IEEE Infocom 2016*, 2016.
- [49] J. Guo, Y. Zhang, X. Chen, S. Yousefi, C. Guo, and Y. Wang. Spatial stochastic vehicle traffic modeling for vanets. *IEEE Transactions on Intelligent Transportation Systems*, 2017.
- [50] Andrea Tassi, Malcolm Egan, Robert Piechocki, and Andrew Nix. Modeling and Design of Millimeter-Wave Networks for Highway Vehicular Communication. *IEEE Transactions on Vehicular Technology*, 66(12):10676 – 10691, August 2017.
- [51] X. Ge, Y. Qiu, J. Chen, M. Huang, H. Xu, J. Xu, W. Zhang, Y. Yang, C. Wang, and J. Thompson. Wireless fractal cellular networks. *IEEE Wireless Communications*, 23(5):110–119, October 2016. ISSN 1536-1284.
- [52] Yixue Hao, Min Chen, Long Hu, Jeungeun Song, Mojca Volk, and Iztok Humar. Wireless fractal ultra-dense cellular networks. *Sensors*, 17(4), 2017.
- [53] Véronique Capdevielle, Afef Feki, and Aymen Fakhreddine. Self-optimization of handover parameters in LTE networks. In *11th International Symposium and Workshops on Modeling and Optimization in Mobile, Ad Hoc and Wireless Networks (WiOpt)*, May 2013.
- [54] H. Arslan, L. Krasny, D. Koilpillai, and S. Chennakeshu. Doppler spread estimation for wireless mobile radio systems. In *IEEE WCNC*, 2000.
- [55] Hong Zhang and A. Abdi. Mobile speed estimation using diversity combining in fading channels. In *IEEE GLOBECOM*, Nov 2004.

- [56] Majed Haddad, Dalia-Georgiana Herculea, Eitan Altman, Nidham Ben Rached, Veronique Capdevielle, Chung Shue Chen, and Frederic Ratovelomanana. Mobility state estimation in LTE, booktitle = in IEEE WCNC, year = 2016, location = Doha, Qatar, keywords = heterogeneous cellular networks, mobile networks, time-based spectral spreading method, user mobility estimation,.
- [57] 3GPP TS 36.304 v.10.5.0 (2012-03). User equipment (UE) procedures in idle mode. In *Tech. Rep. v.10.5.0*, Mar. 2012.
- [58] 3GPP TS 36.331 v.10.5.0 (2012-03). Radio Resource Control (RRC) Protocol specification. In *Tech. Rep. v.10.5.0*, Mar. 2012.
- [59] S. Barbera, P.H. Michaelsen, M. Saily, and K. Pedersen. Improved mobility performance in LTE co-channel hetnets through speed differentiated enhancements. In *IEEE Globecom Workshops (GC Wkshps), 2012*, pages 426–430, Dec 2012.
- [60] J. Turkka, T. Henttonen, and T. Ristaniemi. Self-optimization of lte mobility state estimation thresholds. In *IEEE Wireless Communications and Networking Conference Workshops (WCNCW)*, April 2014.
- [61] A. Merwaday, I. Guvenc, W. Saad, A. Mehbodniya, and F. Adachi. Sojourn time based velocity estimation in small cell poisson networks. *IEEE Communications Letters*, 20(2):340–343, Feb. 2016.
- [62] Dalia Herculea, Chung Shue Chen, Majed Haddad, and Véronique Capdevielle. Straight: Stochastic geometry and user history based mobility estimation. In *ACM HotPOST*, 2016. ISBN 978-1-4503-4344-2.
- [63] S. Uppoor, O. Trullols-Cruces, M. Fiore, and J.M. Barcelo-Ordinas. Generation and analysis of a large-scale urban vehicular mobility dataset. *IEEE Transactions on Mobile Computing*, 13(5):1061–1075, May 2014.
- [64] M.M. Zonoozi and P. Dassanayake. User mobility modeling and characterization of mobility patterns. *IEEE Journal on Selected Areas in Communications*, 15(7):1239–1252, Sep 1997.
- [65] Atsuyuki Okabe, Barry Boots, and Kokichi Sugihara. *Spatial Tessellations: Concepts and Applications of Voronoi Diagrams*. John Wiley & Sons, Inc., New York, NY, USA, 1992. ISBN 0-471-93430-5.
- [66] S Nie, D Wu, M Zhao, X Gu, L Zhang, and L Lu. An enhanced mobility state estimation based handover optimization algorithm in LTE-A self-organizing network.

- The 6th International Conference on Ambient Systems, Networks and Technologies (ANT)*, 2015.
- [67] Geoff Boeing. Visual analysis of nonlinear dynamical systems: Chaos, fractals, self-similarity and the limits of prediction. *Systems*, 4(4), 2016. ISSN 2079-8954. doi: 10.3390/systems4040037.
- [68] L. Arnold. Stoyan, d.; stoyan, h., fractals, random shapes and point fields. methods of geometrical statistics. *ZAMM - Journal of Applied Mathematics and Mechanics / Zeitschrift für Angewandte Mathematik und Mechanik*, 75(8):614–614.
- [69] Wikipedia contributors. Topological space — Wikipedia, the free encyclopedia, 2018. URL [https://en.wikipedia.org/w/index.php?title=Topological\\_space&oldid=859928993](https://en.wikipedia.org/w/index.php?title=Topological_space&oldid=859928993). [Online; accessed 24-September-2018].
- [70] Wikipedia contributors. Lebesgue covering dimension — Wikipedia, the free encyclopedia, 2018. URL [https://en.wikipedia.org/w/index.php?title=Lebesgue\\_covering\\_dimension&oldid=835143885](https://en.wikipedia.org/w/index.php?title=Lebesgue_covering_dimension&oldid=835143885). [Online; accessed 21-August-2018].
- [71] Wikipedia contributors. Sierpinski triangle — Wikipedia, the free encyclopedia, 2018. URL [https://en.wikipedia.org/w/index.php?title=Sierpinski\\_triangle&oldid=860738061](https://en.wikipedia.org/w/index.php?title=Sierpinski_triangle&oldid=860738061). [Online; accessed 24-September-2018].
- [72] Wikipedia contributors. Fractal cosmology — Wikipedia, the free encyclopedia, 2018. URL [https://en.wikipedia.org/w/index.php?title=Fractal\\_cosmology&oldid=857588733](https://en.wikipedia.org/w/index.php?title=Fractal_cosmology&oldid=857588733). [Online; accessed 24-September-2018].
- [73] Y. Mo, J. Liu, and S. Lv. Gis-based analysis of fractal features of the urban road network. In *2015 6th IEEE International Conference on Software Engineering and Service Science (ICSESS)*, pages 845–848, Sept 2015.
- [74] G. S. Thakur, P. Hui, and A. Helmy. On the existence of self-similarity in large-scale vehicular networks. In *2013 9th International Wireless Communications and Mobile Computing Conference (IWCMC)*, July 2013.
- [75] Mousumi Paul and Gautam Sanyal. Traffic analysis of vehicular ad-hoc networks of v2i communication. *Procedia Computer Science*. Eleventh International Conference on Communication Networks, ICCN 2015, August 21-23, 2015,.
- [76] Abhinav Jauhri, Carlee Joe-Wong, and John Paul Shen. On the real-time vehicle placement problem, 2017.

- [77] Seungsin Lee, R. Rao, and R. Narasimha. Characterization of self-similarity properties of discrete-time linear scale-invariant systems. In *2001 IEEE International Conference on Acoustics, Speech, and Signal Processing. Proceedings*, May 2001.
- [78] Kihong Park and Walter Willinger. *Self-Similar Network Traffic: An Overview*, chapter 1, pages 1–38. Wiley-Blackwell, 2002. ISBN 9780471206446.
- [79] Xiaofeng Bai and Abdallah Shami. Modeling self-similar traffic for network simulation. *CoRR*, abs/1308.3842, 2013.
- [80] W. E. Leland, M. S. Taqqu, W. Willinger, and D. V. Wilson. On the self-similar nature of ethernet traffic (extended version). *IEEE/ACM Transactions on Networking*, 2(1):1–15, Feb 1994. ISSN 1063-6692.
- [81] G. Millán and G. Lefranc. A fast multifractal model for self-similar traffic flows in high-speed computer networks. *Proceeding of Computer Science*, 17:420 – 425, 2013. ISSN 1877-0509. First International Conference on Information Technology and Quantitative Management.
- [82] D. Radev and I. Lokshina. Modeling and simulation of self-similar wireless ip network traffic. In *2009 Wireless Telecommunications Symposium*, pages 1–6, April 2009.
- [83] G. Srivatsun, S. Rani, and G. Krishnan. A self-similar fractal cantor antenna for mics band wireless applications. *Wireless Engineering and Technology*, 2(2), 2011.
- [84] C. P. Dettmann, O. Georgiou, and J. P. Coon. More is less: Connectivity in fractal regions. In *2015 International Symposium on Wireless Communication Systems (ISWCS)*, pages 636–640, Aug 2015.
- [85] X. Ge, X. Tian, Y. Qiu, G. Mao, and T. Han. Small cell networks with fractal coverage characteristics. *IEEE Transactions on Communications*, pages 1–1, 2018.
- [86] C. Yuan, Z. Zhao, R. Li, M. Li, and H. Zhang. The emergence of scaling law, fractal patterns and small-world in wireless networks. *IEEE Access*, 5:3121–3130, 2017. ISSN 2169-3536.
- [87] Philippe Jacquet. Optimized outage capacity in random wireless networks in uniform and fractal maps. In *IEEE International Symposium on Information Theory, ISIT 2015, Hong Kong, China, June 14-19, 2015*.
- [88] P. Jacquet. Capacity of simple multiple-input-single-output wireless networks over uniform or fractal maps. In *MASCOTS*, Aug 2013. doi: 10.1109/MASCOTS.2013.66.



- [89] K. T. Herring, J. W. Holloway, D. H. Staelin, and D. W. Bliss. Path-loss characteristics of urban wireless channels. *IEEE Transactions on Antennas and Propagation*, 58(1):171–177, Jan 2010.
- [90] Wikipedia. Street canyon — wikipedia, the free encyclopedia, 2017. [Online; accessed 6-December-2017].
- [91] A. Thornburg, T. Bai, and R. W. Heath. Performance analysis of outdoor mmwave ad hoc networks. *IEEE Transactions on Signal Processing*, 2016.
- [92] E. Ben-Dor, T. S. Rappaport, Y. Qiao, and S. J. Lauffenburger. Millimeter-wave 60 ghz outdoor and vehicle AOA propagation measurements using a broadband channel sounder. In *2011 IEEE Global Telecommunications Conference - GLOBECOM 2011*.
- [93] H. Zhao, R. Mayzus, S. Sun, M. Samimi, J. K. Schulz, Y. Azar, K. Wang, G. N. Wong, F. Gutierrez, and T. S. Rappaport. 28 GHz millimeter wave cellular communication measurements for reflection and penetration loss in and around buildings in New York city. In *2013 IEEE International Conference on Communications (ICC)*.
- [94] Wikipedia contributors. Minkowski–Bouligand dimension — Wikipedia, the free encyclopedia, 2018. URL [https://en.wikipedia.org/w/index.php?title=Minkowski%E2%80%93Bouligand\\_dimension&oldid=862709915](https://en.wikipedia.org/w/index.php?title=Minkowski%E2%80%93Bouligand_dimension&oldid=862709915). [Online; accessed 9-October-2018].
- [95] P. Jacquet and D. Popescu. Self-similarity in urban wireless networks: Hyperfractals. In *Workshop on Spatial Stochastic Models for Wireless Networks, SpaSWiN*, May 2017.
- [96] François Baccelli and Bartłomiej Błaszczyszyn. *Stochastic Geometry and Wireless Networks, Volume I - Theory*. NoW Publishers, .
- [97] Philippe Flajolet, Xavier Gourdon, and Philippe Dumas. Mellin transforms and asymptotics: Harmonic sums. *Theoretical Computer Science*, 1995. ISSN 0304-3975.
- [98] Michael Fuchs, Hsien-Kuei Hwang, and Vytas Zacharovas. An analytic approach to the asymptotic variance of trie statistics and related structures. *Theoretical Computer Science*, 2014. ISSN 0304-3975.
- [99] Adrian Baddeley and Rolf Turner. Modelling spatial point patterns in R, booktitle = Case Studies in Spatial Point Pattern Modelling. Lecture Notes in Statistics 185, 23–74, year = 2006, publisher = Springer.

- [100] Minnesota department of transportation data. <https://www.dot.state.mn.us/tmc/trafficinfo/traffic.html>, . Accessed: 2017-11-22.
- [101] Comptages et enquêtes du trafic: Tableaux statistiques. evolution du trafic sur quelques axes routiers. <https://www.nyon.ch/fr/vivre/mobilite-transport/comptages-et-enquetes-du-traffic-tableaux-statistiques-1198-9065>, .
- [102] Traffic volume flow maps Seattle. <http://whhttp://www.wsdot.com/traffic/seattle/flowmaps/>, .
- [103] Department of planning, transport and infrastructure, South Australia. [https://dpti.sa.gov.au/traffic\\_volumes](https://dpti.sa.gov.au/traffic_volumes), .
- [104] J. Choi, V. Va, N. Gonzalez-Prelcic, R. Daniels, C. R. Bhat, and R. W. Heath. Millimeter-wave vehicular communication to support massive automotive sensing. *IEEE Communications Magazine*, December 2016.
- [105] A. Ghosh, T. A. Thomas, M. C. Cudak, R. Ratasuk, P. Moorut, F. W. Vook, T. S. Rappaport, G. R. MacCartney, S. Sun, and S. Nie. Millimeter-wave enhanced local area systems: A high-data-rate approach for future wireless networks. *IEEE Journal on Selected Areas in Communications*, 2014.
- [106] S. Singh, M. N. Kulkarni, A. Ghosh, and J. G. Andrews. Tractable model for rate in self-backhauled millimeter wave cellular networks. *IEEE Journal on Selected Areas in Communications*, 2015.
- [107] Ioannis Broustis and Michalis Faloutsos. Routing in vehicular networks: Feasibility, modeling, and security. *International Journal of Vehicular Technology*, 2008.
- [108] A. Checko, H. L. Christiansen, Y. Yan, L. Scolari, G. Kardaras, M. S. Berger, and L. Dittmann. Cloud ran for mobile networks—a technology overview. *IEEE Communications Surveys Tutorials*, 17(1):405–426, 2015. ISSN 1553-877X.
- [109] Joohwan Kim, Xiaojun Lin, and Ness B. Shroff. Optimal anycast technique for delay-sensitive energy-constrained asynchronous sensor networks. *IEEE/ACM Transactions on Networking*.
- [110] Joohwan Kim, Xiaojun Lin, Ness B. Shroff, and Prasun Sinha. Minimizing delay and maximizing lifetime for wireless sensor networks with anycast. *IEEE/ACM Transactions on Networking*, 18(2):515–528, 2010.
- [111] Nabhendra Bisnik and Alhussein A. Abouzeid. Delay and capacity in energy efficient sensor networks. In *Proceedings of the 4th ACM Workshop on Performance*

- Evaluation of Wireless Ad Hoc, Sensor, and Ubiquitous Networks*, pages 17–24, 2007. ISBN 978-1-59593-808-4.
- [112] Z. M. Wang, S. Basagni, E. Melachrinoudis, and C. Petrioli. Exploiting sink mobility for maximizing sensor networks lifetime. In *Proceedings of the 38th Annual Hawaii International Conference on System Sciences*, 2005.
- [113] Carla-Fabiana Chiasserini, Imrich Chlamtac, Paolo Monti, and Antonio Nucci. Energy efficient design of wireless ad hoc networks. In *Proceedings of the Second International IFIP-TC6 Networking Conference on Networking Technologies, Services, and Protocols*, NETWORKING '02. Springer-Verlag.
- [114] J. E. Wieselthier, G. D. Nguyen, and A. Ephremides. On the construction of energy-efficient broadcast and multicast trees in wireless networks. In *Proceedings IEEE INFOCOM 2000. Conference on Computer Communications. Nineteenth Annual Joint Conference of the IEEE Computer and Communications Societies (Cat. No.00CH37064)*.
- [115] P. J. Wan, G. Călinescu, X. Y. Li, and O. Frieder. Minimum-energy broadcasting in static ad hoc wireless networks. *Wireless Networks*, 8(6):607–617, November 2002. ISSN 1022-0038.
- [116] M. J. Neely and E. Modiano. Capacity and delay tradeoffs for ad hoc mobile networks. *IEEE Transactions on Information Theory*, 2005.
- [117] X. Mao, S. Tang, X. Xu, X. Y. Li, and H. Ma. Energy-efficient opportunistic routing in wireless sensor networks. *IEEE Transactions on Parallel and Distributed Systems*, 2011.
- [118] Xiuzhen Cheng, Ding-Zhu Du, Lusheng Wang, and Baogang Xu. Relay sensor placement in wireless sensor networks. *Wireless Networks*, 2008.
- [119] Wikipedia contributors. Chebyshev's inequality — Wikipedia, the free encyclopedia, 2018. URL [https://en.wikipedia.org/w/index.php?title=Chebyshev%27s\\_inequality&oldid=855671467](https://en.wikipedia.org/w/index.php?title=Chebyshev%27s_inequality&oldid=855671467). [Online; accessed 24-August-2018].
- [120] S. Malik, P. Jacquet, and C. Adjih. On the throughput capacity of wireless multi-hop networks with ALOHA, node coloring and CSMA. In *2011 IFIP Wireless Days*.
- [121] S. Li and C. Huang. A multihop broadcast mechanism for emergency messages dissemination in vanets. In *2018 IEEE 42nd Annual Computer Software and Applications Conference*, pages 932–937, July 2018.

- [122] W. Liu, K. Nakauchi, and Y. Shoji. A neighbor-based probabilistic broadcast protocol for data dissemination in mobile iot networks. *IEEE Access*, 6:12260–12268, 2018.
- [123] M. Noor-A-Rahim, G. G. M. N. Ali, H. Nguyen, and Y. L. Guan. Performance analysis of ieee 802.11p safety message broadcast with and without relaying at road intersection. *IEEE Access*, 6:23786–23799, 2018.
- [124] Alejandro Galaviz-Mosqueda, Miguel Morales-Sandoval, Salvador Villarreal-Reyes, Hiram Galeana-Zapién, Raúl Rivera-Rodríguez, and Miguel Ángel Alonso-Arévalo. Multi-hop broadcast message dissemination in vehicular ad hoc networks: A security perspective review. *International Journal of Distributed Sensor Networks*, 13(11), 2017.
- [125] G. Karagiannis, O. Altintas, E. Ekici, G. Heijenk, B. Jarupan, K. Lin, and T. Weil. *IEEE Communications Surveys Tutorials*, 2011.
- [126] M. Gerla, E. K. Lee, G. Pau, and U. Lee. Internet of vehicles: From intelligent grid to autonomous cars and vehicular clouds. In *2014 IEEE World Forum on Internet of Things (WF-IoT)*, March .
- [127] E. Ekici, Yaoyao Gu, and D. Bozdag. Mobility-based communication in wireless sensor networks. *Comm. Mag.*, 44(7):56–62, September 2006. ISSN 0163-6804.
- [128] G. Korkmaz, E. Ekici, and F. Ozguner. An efficient fully ad-hoc multi-hop broadcast protocol for inter-vehicular communication systems. In *2006 IEEE International Conference on Communications*, volume 1, pages 423–428, June 2006.
- [129] E. Baccelli, P. Jacquet, B. Mans, and G. Rodolakis. Highway vehicular delay tolerant networks: Information propagation speed properties. *IEEE Transactions on Information Theory*, March 2012.
- [130] X. Qin, G. Xie, and J. Gao. A dynamic topological potential and social relationship based routing protocol for mobile social delay tolerant networks. In *2017 International Conference on Computer, Information and Telecommunication Systems (CITS)*, July 2017.
- [131] D. X. Dzurovcak and S. Yang. Performance analysis of routing protocols in delay tolerant networks. In *2017 IEEE 14th International Conference on Mobile Ad Hoc and Sensor Systems MASS*, Oct 2017.

- [132] D. Cheliotis, I. Kontoyiannis, M. Loulakis, and S. Toumpis. Exact speed and transmission cost in a simple one-dimensional wireless delay-tolerant network. In *2017 IEEE International Symposium on Information Theory (ISIT)*, pages 476–480, June 2017.
- [133] R. Cavallari, R. Verdone, and S. Toumpis. Cost/speed analysis of mobile wireless dtns under random waypoint mobility. In *2016 14th International Symposium on Modeling and Optimization in Mobile, Ad Hoc, and Wireless Networks (WiOpt)*, pages 1–8, May 2016.
- [134] Marco Fiore and Jérôme Härri. The networking shape of vehicular mobility. In *Proceedings of the 9th ACM International Symposium on Mobile Ad Hoc Networking and Computing*. ACM, 2008.
- [135] M. Mauve, J. Widmer, and H. Hartenstein. A survey on position-based routing in mobile ad hoc networks. *IEEE Network*, 15(6):30–39, Nov 2001. ISSN 0890-8044.
- [136] Scalable Networks. QualNet Network Software. <https://web.scalable-networks.com/qualnet-network-simulator-software>, 2018. [Online; accessed 3-July-2018].
- [137] Wikipedia contributors. IEEE 802.11p — Wikipedia, the free encyclopedia, 2018. URL [https://en.wikipedia.org/w/index.php?title=IEEE\\_802.11p&oldid=848044994](https://en.wikipedia.org/w/index.php?title=IEEE_802.11p&oldid=848044994). [Online; accessed 3-July-2018].
- [138] C. Gloaguen, F. Fleischer, H. Schmidt, and V. Schmidt. Fitting of stochastic telecommunication network models via distance measures and monte-carlo tests. *Telecommunication Systems*, 2006.
- [139] F. Morlot. A population model based on a poisson line tessellation. In *2012 10th International Symposium on Modeling and Optimization in Mobile, Ad Hoc and Wireless Networks (WiOpt)*, pages 337–342, May 2012.
- [140] Philippe Jacquet and Wojciech Szpankowski. Analytical depoisonization and its applications. *Theoretical Computer Science*, 201(1-2):1–62, 1998.